EFDA–JET–PR(07)45

D. Moreau, D. Mazon, M. Ariola, G. De Tommasi, L. Laborde, F. Piccolo, F. Sartori, T. Tala, L. Zabeo, A. Boboc, E. Bouvier, M. Brix, J. Brzozowski, C. D. Challis, V. Cocilovo, V. Cordoliani, F. Crisanti, E. De La Luna, R. Felton, N. Hawkes, R. King, X. Litaudon, T. Loarer, J. Mailloux, M. Mayoral, I. Nunes, E. Surrey, O. Zimmerman and JET EFDA contributors

A Multiple Time Scale Dynamic-Model Approach for Magnetic and Kinetic Profile Control in Advanced Tokamak Scenarios on JET

A Multiple Time Scale Dynamic-Model Approach for Magnetic and Kinetic Profile Control in Advanced Tokamak Scenarios on JET

D. Moreau[1], D. Mazon[1], M. Ariola[2], G. De Tommasi[2], L. Laborde[3], F. Piccolo[3], F. Sartori[3], T. Tala[4], L. Zabeo[3], A. Boboc[3], E. Bouvier[5], M. Brix[3], J. Brzozowski[6], C. D. Challis[3], V. Cocilovo[7], V. Cordoliani[5], F. Crisanti[7], E. De La Luna[8], R. Felton[3], N. Hawkes[3], R. King[3], X. Litaudon[1], T. Loarer[1], J. Mailloux[3], M. Mayoral[3], I. Nunes[9], E. Surrey[3], O. Zimmerman[10] and JET EFDA contributors*

JET-EFDA, Culham Science Centre, OX14 3DB, Abingdon, UK

[1]Euratom-CEA Association, DSM/DRFC, CEA-Cadarache, 13108 St Paul lez Durance, France
[2] Euratom-ENEA-CREATE Association, Univ. Napoli Federico II, I-80125 Napoli, Italy
[3] Euratom-UKAEA Fusion Association, Culham Science Centre, Abingdon, Oxon OX14 3DB, UK
[4] Euratom-Tekes Association, VTT, PO Box 1000, FIN-02044 VTT, Finland
[5] Ecole Polytechnique, Route de Saclay, 91128, Palaiseau, France
[6]Euratom-VR Association, Department of Physics, KTH, SE 10691, Stockholm, Sweden
[7] Euratom-ENEA Association, C.R. Frascati C.P. 65, 00044 Frascati, Italy
[8]Euratom-CIEMAT Association, ES Avenida Complutense 22 E-28040, Madrid, Spain
[9]Euratom-IST Association, Centro de Fus„o Nuclear, IST, 1049-001, Lisboa, Portugal
[10]Euratom-FZJ Association, IPP, Forschungszentrum, D-52425, J¸lich GmbH, Germany
** See annex of M.L. Watkins et al, "Overview of JET Results ",*
(Proc. 21 st IAEA Fusion Energy Conference, Chengdu, China (2006)).

Preprint of Paper to be submitted for publication in
Nuclear Fusion

ABSTRACT

Real-time simultaneous control of several radially distributed magnetic and kinetic plasma parameters is being investigated on JET, in view of developing integrated control of advanced tokamak scenarios. This paper describes the new model-based profile controller which has been implemented during the 2006-2007 experimental campaigns. The controller aims to use the combination of Heating and Current Drive (H&CD) systems - and optionally the Poloidal Field (PF) system - in an optimal way to regulate the evolution of plasma parameter profiles such as the safety factor, $q(x)$, and gyro-normalized temperature gradient, $\rho_{Te}^*(x)$. In the first part of the paper, a technique for the experimental identification of a minimal dynamic plasma model is described, taking into account the physical structure and couplings of the transport equations, but making no quantitative assumptions on the transport coefficients or on their dependences. To cope with the high dimensionality of the state space and the large ratio between the time scales involved, the model identification procedure and the controller design both make use of the theory of singularly perturbed systems by means of a multiple-time-scale approximation. The second part of the paper provides the theoretical basis for the controller design. The profile controller is articulated around two composite feedback loops operating on the magnetic and kinetic time scales, respectively, and supplemented by a feedforward compensation of density variations. For any chosen set of target profiles, the closest coherent state achievable with the available actuators is uniquely defined. It is reached, with no steady state offset, through a near-optimal proportional-integral control algorithm. Conventional optimal control is recovered in the limiting case where the ratio of the plasma confinement time to the resistive diffusion time tends to zero. Closed-loop simulations of the controller response have been performed in preparation for experiments, and typical results are shown. Finally, in the last section of the paper, the first experimental results using this dynamic-model approach to control the plasma current and the safety factor profile on JET, either with the three H&CD systems or also with the PF system as an additional actuator, are presented and discussed.

1. INTRODUCTION

Extensive research programs have been devoted, worldwide, to the development of advanced tokamak operation scenarios in which an optimization of some plasma parameter profiles results in a large improvement in plasma performance at reduced plasma current [1-5]. The design of an economically attractive *steady state* fusion reactor relies on such scenarios because a high-gain fusion burn could then be achieved while a major fraction of the plasma current is self-generated by the neoclassical bootstrap effect. Integrated real-time control of such bootstrap-dominated plasma regimes [6] is a new challenge, but it is essential for steady state operation and it will be one of the ITER objectives to demonstrate that advanced operation scenarios can yield significant fusion gains ($Q_{fus} \approx 5$) in steady state, under controlled operation [7-8]. In the meantime, experimental investigations have started on various tokamaks to find practical means of regulating advanced tokamak discharges [9-15].

The simultaneous real-time control of radially distributed magnetic and kinetic plasma parameters, such as the current and electron temperature gradient profiles, was achieved for the first time during the 2002-2004 experimental campaigns on JET [16-18]. At this stage, and for the sake of simplicity, the controller was based on the static plasma response only, and on an algorithm that minimises a weighted sum of least square integral errors between the requested profiles and the measured ones [19]. The integration of magnetic and kinetic profiles - known to be strongly coupled - into a single controller is particularly relevant to advanced tokamak scenarios in future fusion devices such as ITER where the Heating and Current Drive (H&CD) actuators will be quite constrained. With a limited number of actuators and a large set of parameters and profiles to control, the strong linkage between the multiple profiles which define the non-linear plasma state can be seen as an advantage. Of course, the response of all the relevant profiles to variations of the actuators around a given equilibrium state needs to be identified by some means. But then, the real-time data relative to these profiles (plasma density, velocity, pressure, safety factor, etc ...) can be integrated into a single controller which regulates the global plasma state through a minimization algorithm [19] rather than each profile accurately and separately. Such an integrated approach to plasma control seems essential and it should be validated already in present experiments if one is to ultimately achieve high-beta/high-bootstrap-current burning plasmas for steady state reactor operation.

Another requirement of the profile control investigations we have proposed on JET is the use of the available actuators in their routine operating mode, i.e. avoiding special features that may not extrapolate to burning plasmas. In ITER, some actuators may be less versatile than in present-day tokamaks, due to simple physics and/or technology considerations (antenna design, wave propagation, etc..). In JET, controlling accurately the radial deposition of Lower Hybrid (LH) waves through the launched n// spectrum [12-13] could be introduced within the proposed control algorithm [19]. But this does not offer much flexibility in the location of maximum power deposition in high-beta fusion plasmas and, in addition, this may have to be done at the expense of degrading the conditions of optimum wave coupling and directivity, and of maximum power transmission through the LH launcher. It was therefore not implemented at this stage of the controller design.

More generally, on present-day tokamaks as well as for ITER, none of the available H&CD actuators - either Neutral Beam Injection (NBI), Radio Frequency (RF) waves for Ion Cyclotron Resonant Heating (ICRH), LH waves, or Electron Cyclotron (EC) waves, - seems flexible and powerful enough, on its own, to tailor the current density profile as required for optimum performance. Also, current drive cannot be decoupled from heating (and sometimes fuelling and torque), especially in the presence of large bootstrap current and alpha-particle heating fractions since both heating and fuelling drive the bootstrap current and the fusion power. Therefore, dedicating a specific actuator to a specific task does not seem appropriate.

The approach newly developed on JET aims to use the combination of H&CD/PF (poloidal field) systems and the experimentally deduced plasma couplings in the most efficient dynamic way to achieve a set of simultaneous tasks. In this respect, it stands in contrast with experiments in

which a given actuator (e.g. LH, EC or NBI power) controls a particular scalar parameter characterising a plasma profile (e.g. minimum safety factor, internal inductance, β_N, etc ...) [11-14]. The 2004 experiments [16-17] using a controller based on the static plasma response were successful in achieving the various targets that were aimed at, thus demonstrating the validity of the proposed coupled profiles approach. However, the control was found to be too sensitive to rapid plasma events such as the spontaneous emergence of internal transport barriers (ITB) or MHD instabilities. In order to address this issue, a technique for the experimental identification of a dynamic plasma model has been developed, taking into account the physical structure and couplings of the transport equations, but making no quantitative assumptions on the transport coefficients or on their dependences [10].

The next section describes the analysis which leads to the choice of the relevant state variables, and the physical constraints to be imposed on the corresponding state-space model. The high dimensionality of the state space and the large ratio between the various time scales involved (resistive and thermal diffusions with strong interactions between fast and slow dynamic modes) call for an appropriate model identification procedure. The technique uses the theory of singularly perturbed systems (i. e. a multiple-time-scale approximation) thanks to a small parameter, ε, representing the ratio of the fast and slow timescales. It generates a slow and a fast model of reduced orders which are shown to describe the system satisfactorily.

The third section of the paper provides the theoretical basis for the profile controller design. The control is near-optimal in the sense that it asymptotically merges into conventional optimal control, with $O(\varepsilon^2)$ accuracy, in the limiting case where ε tends to zero. The paper then describes closed-loop simulations in which the radial profiles of the plasma safety factor and of the gyro-normalized electron temperature gradient [20] are controlled simultaneously.

The fourth part of the paper finally presents some experimental results concerning the control of the safety factor profile on JET. They were conducted using the new controller in a limited (and unoptimized) set of possible configurations, i.e. with different H&CD actuators, radial control location and minimization criteria, and with/without the PF system as an actuator.

2. IDENTIFICATION OF A STATE-SPACE PLASMA RESPONSE MODEL

2.1. STRUCTURE OF THE DYNAMIC PLASMA MODEL AND NATURAL STATE VARIABLES

In order to use optimal control theory and regulate the plasma evolution in advanced tokamak scenarios, a physics-based, semi-empirical technique has been developed to *experimentally identify* a dynamic plasma model [21]. The structure of the model stems from a set of simplified transport equations,

$$\mu_0 \frac{\partial \mathbf{j}}{\partial t} = -\nabla \times \nabla \times \mathbf{E} \qquad \frac{\partial N}{\partial t} = -\nabla . \Gamma_n + S_n \qquad \frac{3}{2}\frac{\partial (NT\ \ )}{\partial t} = -\nabla . \Gamma_T + S_T \qquad (1)$$

which relate the time variation of the current density, J, plasma density, N, and temperature, T, to the electric field, E, particle and heat fluxes, G_n and G_T and particle and heat sources, S_n and S_T. The toroidal magnetic field is assumed constant in time. When these equations are averaged over magnetic flux surfaces they yield a one-dimensional (1-D) model in which all physical variables depend only on a radial variable, *x*, and on time. Such models form the basis of many time-dependent computer codes, e. g. [22-24], in which the various transport coefficients generally consist of neoclassical terms derived from first principles (collisional transport) and of additional terms that describe turbulent transport in an empirical way and generally provide a fair simulation of some experimental observations. For some interpretative applications, this is a good compromise between theory-based simulations and empirical modelling of phenomena which are not fully understood. For real-time control purposes, it seems however preferable to make no ad-hoc assumptions on the parametric dependences of the transport coefficients. Instead, an empirical model can be sought, that needs only be valid in some broad vicinity of an equilibrium state, and in which coupling between the various plasma parameters is retained with no loss of generality. A rigorous derivation of the 1-D, flux-averaged, transport equations in the most general geometry yields cumbersome expressions including metric tensor coefficients, with too many unknown parameters to identify experimentally. A different compromise is therefore needed here, and the geometrical rigour in the derivation will be traded off against the simplicity of the model.

In the proposed approach, the system (Eq. 1) is linearized around an *equilibrium reference state* which needs not be known explicitly, and a state space model (a form commonly used in control engineering) of minimal complexity is sought, whose structure is consistent with the general structure of linearized 1-D transport equations, apart from cumbersome geometrical corrections which are omitted (see appendix A1.1).

The following assumptions have also been made in Eq. (1) in order to keep the order of the system within reasonable limits for its experimental identification to be tractable :

i) we consider a one-fluid plasma model with varying particle density N(*x*, t), temperature T(*x*, t) and current density, J(*x*, t) (the same methodology could be followed to seek a model with different temperatures for electrons and ions, $T_e \neq T_i$, and eventually with plasma flows and momentum transport),

ii) the particle and heat fluxes, G_n and G_T, depend only on the density, N(*x*, t), temperature, T(*x*, t), and on the current density, J(*x*, t), through differential operators,

iii) the electrical conductivity depends on T(*x*, t), and possibly on N(*x*, t) and J(*x*, t) through neoclassical or anomalous effects, but variations of the effective charge, Z_{eff}, are neglected (they could be taken into account as a disturbance),

iv) gas fuelling is small compared with the combined effect of beam fuelling and recycling, which are coupled to the heating power, so that the particle source, $S_n(x, t)$, depends only on the H&CD input powers (essentially through the NBI particle deposition), and on N(*x*, t), T(*x*, t) and J(*x*, t),

v) the heat deposition profile $S_T(x, t)$ depends on the various H&CD input powers, and on $N(x, t)$, $T(x, t)$ and $J(x, t)$ (the effect of the poloidal magnetic field on wave propagation and absorption can be important),

vi) the non-inductive current density also depends on the various H&CD input powers, and on $N(x, t)$, $T(x, t)$ and $J(x, t)$.

In the framework of our simplified model, the state variables appear naturally to be the variations of the *internal* poloidal magnetic flux, $\Psi = \psi - \psi_{ref}$, and of the temperature, $T = T - T_{ref}$, with respect to their reference values (their values in the reference state). A lumped-parameter version of the state space model is then derived, which reads :

$$\partial\Psi / \partial t = A_{11}\,\Psi(t) + A_{12}\,T(t) + B_{11}\,P(t) + B_{12}\,n(t) + B_{\Psi V}.V_{ext}(t) \qquad (2a)$$

$$\varepsilon\,\partial T / \partial t = A_{21}\,\Psi(t) + A_{22}\,T(t) + B_{21}\,P(t) + B_{22}\,n(t) \qquad (2b)$$

with inputs $P(t) = [P_{LH}(t), P_{NBI}(t), P_{ICRH}(t)] = P(t) - P_{ref}$, the heating and current drive input powers (lower hybrid, neutral beam and radio-frequency), $V_{ext} = V_{ext}(t) - V_{ref}$, the loop voltage at the plasma surface, and n(t), the plasma density. In Eq. (2), the distributed variables $\Psi(x, t)$, $T(x, t)$ and $n(x, t) = N(x, t) - N_{ref}$ have been projected onto a finite set of trial functions (cubic splines, $a_i(x)$, see Fig. 1a) using a Galerkin scheme (see appendix A1.2) so that the original differential system of equations reduces to an ordinary linear differential system where $B_{\Psi V}$ is known and A_{ij}, B_{ij} (i=1, 2 and j=1, 2) are matrices of appropriate dimensions which are to be identified either from simulated data or from experimental data.

We have purposely restricted the number of H&CD actuators to three, for the sake of simplicity. In fact the JET NBI system is composed of two boxes of eight injectors each with different power deposition profiles (normal or tangential, central or off-axis), and a distinction between several groups of injectors could be made to increase the number of independent actuators (e.g. to control also the plasma rotation profile). The same holds for the four ICRH antennas which could be powered at different frequencies, and for the LH launcher modules which could launch waves with different phase velocity and provide more flexibility on the power and current deposition profiles. However, increasing the number of actuators should be made at the expense of the power headroom available on each actuator, and frequent saturation of several actuators would result unless the systems were oversized. It was therefore not considered at this stage. It was then essential to constrain the configuration of the systems so that they always deliver a given power in the same way. For example, a priority order was imposed on the NBI injectors so that, for a given power, a unique combination of the NBI injectors was used.

The small (constant) parameter, ε, represents the typical ratio between the energy confinement time and the characteristic resistive diffusion time ($\varepsilon << 1$). It is introduced here to scale matrices

A_{ij} and B_{ij} so that their coefficients have similar magnitudes, and it allows singular perturbation methods to be applied in order to simplify both model identification and controller design.

The real-time control of the plasma density profile could be integrated within the proposed scheme with some additional actuator (e.g. pellet injection) but it has not been considered yet in the present controller implementation. Variations of the plasma density, n(*x*, t), are partly due to neutral beam fuelling, an effect which could be imbeded either into the B_{21} or the B_{22} matrix. Yet, density variations which are not correlated with the H&CD powers subsist. They will be considered as disturbances and possibly compensated (see section 3.2). Density variations may also have a systematic disturbing influence on some measurements and on the real-time magnetic reconstruction of the plasma equilibrium. If they can be identified, the latter effects must be described through the B_{22} matrix. Therefore, in Eqs. (2) and in the following, the vector n(t) contains coefficients which characterize the plasma density profile (e.g. line-integrated measurements along some chords, etc...), and is treated as an additional input to the system but not as a control actuator. Introducing a generalized input vector, u(t), which contains P(t), V_{ext}(t) and n(t), the system can be rewritten in a slightly more compact form :

$$\partial\Psi / \partial t = A_{11}\,\Psi(t) + A_{12}\,T(t) + B_1\,u(t) \tag{3a}$$

$$\varepsilon\,\partial T / \partial t = A_{21}\,\Psi(t) + A_{22}\,T(t) + B_2\,u(t) \tag{3b}$$

2.2. The Two Time Scales and the Singular Perturbation Approximation

Because of the high dimensionality of the physical state space, the numerical identification of a comprehensive model (Eq. 1-3) can be anticipated to be very difficult. Ideally, one would even try to retain the differential nature of the original system by using appropriate techniques, rather than projecting the system onto a set of basis functions. There are indeed situations in which a genuine distributed-parameter model is definitely required to design a satisfactory controller (e.g. a low-order discrete model would be unappropriate if high order modes were unstable). However, unless the need for such a model becomes really apparent, and bearing in mind that the model identification will have to be made from noisy experimental data until an accurate tokamak plasma simulator is available, a system discretization seems unavoidable. Nonetheless, a sufficient number of basis functions is required if the original distributed-parameter system is to be fairly well approximated. The number of parameters to be identified in Eq.(3a-3b) then rapidly increases with the size of matrices A_{ij}, B_k, and the possible solutions (when they exist) become multiple, unphysical and unstable to small changes in the data : the identification problem becomes ill-conditioned.

Part of the difficulty stems from the fact that various time scales are involved in the dynamics of the system, as seen from the order of magnitude of the parameter, ε, introduced above ($\varepsilon \approx 0.05$ in JET and it will be even smaller in a burning plasma). It seems judicious, then, to take advantage of this small parameter and to investigate identification and control techniques which are based upon the

theory of singularly perturbed systems and multiple-time-scale expansions [25]. This amounts to expanding each dependent variable in powers of ε, defining an additional independent variable, $\tau = t/\varepsilon$, to describe the fast dynamics while t describes the slow dynamics, and to splitting variables into a sum of a fast and a slow component which depend on τ and t, respectively. A well-posed set of ordinary differential equations is then obtained by grouping terms of equal order in ε and imposing that, in the asymptotic limit where ε tends to zero, the initial conditions for the slow dynamics (t = 0) must match the quasi-steady-state solution on the fast dynamics ($\tau \rightarrow \infty$).

It is clear from the structure of the original system that, apart from the anomalous flux redistribution caused by some rapid MHD events such as sawtooth crashes, etc… (which will be treated by the controller as external disturbances), Ψ has only a slow evolution. Its fast component can be set identically to zero in the two-time-scale model. Besides, this would be true for any other magnetic variable (current density, safety factor profile, etc...). We shall therefore seek two models of reduced orders, a slow model (or quasi-steady-state model),

$$\partial \Psi / \partial t = A_s \Psi + B_s u_s \qquad \text{together with} \qquad T_s = C_s \Psi + D_s u_s \tag{4}$$

and a fast model,

$$\partial T_f / \partial t = A_f T_f + B_f u_f \tag{5}$$

Here T_s and T_f are the slow and fast components, respectively, of the temperature ($T=T_s+T_f$), and u_s and u_f are the slow and fast components, respectively, of the input vector ($u=u_s+u_f$). It is straightforward to show that the new matrices to be identified are linked to the original model matrices (Eq. 3a-3b) through the relations :

$$A_s = A_{11} - A_{12} \,.\, A_{22}^{-1} \,.\, A_{21} \tag{6a}$$

$$B_s = B_1 - A_{12} \,.\, A^{-1} \,.\, B_2 \tag{6b}$$

$$C_s = - A_{22}^{-1} \,.\, A_{21} \tag{6c}$$

$$D_s = - A_{22}^{-1} \,.\, B_2 \tag{6d}$$

$$A_f = \varepsilon^{-1} A_{22} \tag{6e}$$

$$B_f = \varepsilon^{-1} B_2 \tag{6f}$$

2.3. Non-dimensional Controlled Variables

Although the poloidal magnetic flux and plasma temperature appear as relevant state variables, it

can prove practical to control some other plasma parameters which are more directly linked with MHD stability criteria or plasma confinement physics (e.g. current density, internal inductance and plasma pressure, beta parameter, critical gradients, ITB triggering, etc ..). If, in addition, the controlled variables were non-dimensional, then the range of their optimum target values would be known and would not depend so much on the engineering parameters of a particular discharge (toroidal magnetic field, plasma density, current, shape, etc...).

A minimal possible set of magnetic and kinetic parameter profiles which fulfill such requirements is composed of the safety factor, $q(x)$, and the gyro-normalized temperature gradient, $\rho_{Te}^*(x)$. They have been chosen in earlier control experiments [16-19] and will therefore be introduced here into the state-space model. In fact, to take account of the inverse dependence of the safety factor on the current density or the poloidal flux, the rotational transform, $\iota(x)) = 1/q(x)$, is used to describe the magnetic state of the plasma rather than $q(x)$ itself. As for $\Psi(x)$ and $T(x)$, A Galerkin approximation is used and in the following, the notations Ψ, T, μ and ρ will refer to the coefficients of $\Psi(x)$, $T(x)$, $\iota(x)$ and $\rho_{Te}^*(x)$ expansions, respectively. The same cubic splines are used for $\iota(x))$ $\Psi(x)$ and $T(x)$ (Fig. 1a), but $\rho_{Te}^*(x)$ involves the gradient of a noisy signal and requires a stronger smoothing. A piecewise linear fit with the basis functions, $b_i(x)$, displayed on Fig. 1b was shown to be a better choice for $\rho_{Te}^*(x)$ [17].

Noticing that $\iota(x)) = d\Psi(x)/d\Phi(x)$ and $\rho_{Te}^*(x) \propto [\sqrt{T_e}(x)B_T(x)].[\nabla T_e(x)/T_e(x)]$ (Ref. [20]), where $B_T(x)$ and $\Phi(x)$ are the toroidal magnetic field on the equatorial plane and the toroidal magnetic flux, respectively, one can nearly map the variations of $\iota(x)$ and $\rho_{Te}^*(x)$ around a given equilibrium onto the variations of the state variables $\Psi(x)$ and $T(x)$ around this equilibrium, at least approximately and in the linear domain. This requires that the time variations of $B_T(x)$ and $\Phi(x)$ are not essential and do not depend intrinsically on the power inputs, an assumption that can be checked quantitatively from the experimental data (see section 2.5.2). As a result, $\iota(x)$ and $\rho_{Te}^*(x)$ can possibly be treated as alternative *state variables*, and not as *output variables* that depend on the states of the system *as well as* on the value of the system inputs. Linearizing the expressions above for $\iota(x)$ and $\rho_{Te}^*(x)$ around the equilibrium state, differentiating the basis functions and neglecting the toroidal field variations and the residues in the various expansions, direct matrix relations between the Galerkin coefficients μ and Ψ, on one hand, and between T and ρ on the other hand can be formally derived. Within the two-time-scale approximation, this yields the following type of relations :

$$\mu = C_{\mu,\psi}.\Psi \quad \text{and} \quad \rho_s = C_{\rho,\psi}\Psi + D_{\rho,\psi}u_s \ (\text{or } \rho_s = C_{\rho,\mu}\mu + D_{\rho,\mu}u_s) \tag{7}$$

and

$$\rho_f = C_{\rho,T}.T_f \tag{8}$$

which complete the original system (Eq. 4-5). As an alternative to the reduced order models governing Ψ and T, one can therefore seek approximate state space models governing μ and ρ in the form:

$$\partial\mu / \partial t = A_s \mu + B_s u_s \qquad \text{together with} \qquad \rho_s = C_s \mu + D_s u_s \tag{9}$$

and

$$\partial\rho_f / \partial t = A_f \rho_f + B_f u_f \tag{10}$$

If a set of matrices A_s, B_s, C_s, D_s, and A_f, B_f can be identified so that the model reproduces fairly the data, it follows that the non-dimensional variables [μ, ρ] can be controlled by appying singular perturbation methods directly to state-feedback control rather than to a less robust output-feedback control for which the closed-loop stability of the high-frequency dynamics would not be guaranteed [25].

2.4. PRELIMINARY INVESTIGATIONS ON MODEL IDENTIFICATION USING LOCAL PROFILE DATA AND THE H&CD ACTUATORS

2.4.1. Computer-Simulated Data

A series of interactive routines have been developed to try and numerically identify the various elements of two-time-scale state-space plasma models (Eq. 4-5, 7-8 or 9-10), either from computer simulated data or from real experimental data. First attempts were made using simulated data, i.e. data obtained through semi-empirical time-dependent simulations of the plasma evolution with large transport codes. It would indeed be quite satisfactory if one could design a profile controller using numerical simulations, prior to running any real experiment. However, using the JETTO code [24] to simulate previous control experiments, with a controller based only on the static plasma response, it was found that the *static* response and the resulting controller gain matrices were significantly different from experimentally deduced ones [26]. A fortiori, we believe that the present understanding of plasma transport phenomena is not sufficient yet to make reliable predictions of the *dynamic* response of the plasma. This is particularly true concerning the evolution of some plasma parameter profiles in the advanced operation scenarios. Hence, for the time being, simulations can prove useful for training purposes, but dedicated open-loop experiments are necessary to collect the required data before running sophisticated model identification codes.

Various sets of codes have been written to cope with different types of data and to investigate different data processing and identification strategies. They all rely heavily on system identification algorithms described in [27] and on the corresponding MATLAB® Identification Toolbox functions. They run on the JET cluster of UNIX workstations.

The linearization which is at the origin of the state-space model assumes that all data (inputs, outputs and state variables) are defined with respect to a reference equilibrium state which corresponds to a given set of plasma parameters and input powers. However, JET pulses are generally too short to reach a well-defined equilibrium state, particularly in the advanced scenarios, and therefore such a state cannot be determined accurately. Nevertheless, thanks to some simple data processing, approximate state space models can be found without explicit knowledge of the reference state (see appendix A2).

To illustrate the general methodology underlying data processing and the proposed identification procedures, we shall discuss here some results obtained with JETTO-simulated data. In the example shown, the first 5 seconds of the simulations are based on an experimental pulse (JET pulse # 62527), i.e. the inputs are chosen accordingly and some poorly known parameters are tuned to reproduce the experiment at best. The simulations are then extended with either slow or fast modulations of one (or all) of the H&CD input powers. In these simulations, the plasma current was maintained constant through an independent feedback control using the surface loop voltage as an actuator. The latter was therefore not considered as a potential actuator for profile control (see section 3). The identification of the slow (resistive) time scale response requires modulation periods of about 1 second or more, while the fast (confinement) time scale can better be resolved with modulation periods of the order of 100 ms or less. We thus performed two sets of simulations and the sampling time for storing the simulation results was chosen as 0.01 s for the fast modulation (FM) pulses and 0.09s for the slow modulation (SM) ones. Each set consists of a reference pulse without any input modulation, 3 pulses where each H&CD actuator (LH, NBI, ICRH) is modulated (an example is shown on Fig. 2), and a pulse where all the input powers are modulated simultaneously and randomly.

A stepwise approach was followed in order to identify only some particular elements of the model at a time. Whenever possible, matrices obtained at one step were either fixed or used to initialize the following step of the identification procedure. For instance, the identification of the fast model matrices A_f and B_f can be carried out by considering only the simulations where each one, and then all of the input powers have been modulated randomly, with different high frequency spectra ($f \approx 10$Hz), around an average power corresponding to the reference state. The slow component (e.g. $f < 2.5$Hz) of both the inputs and outputs are filtered out so that the fast response can be isolated from the slow relaxation process due to resistive diffusion. A typical waveform for the fast modulations of the NBI power is shown on Fig. 2 (red dotted trace).

To start with a low order model, let us consider for instance the electron temperature (Eq. 5) at only two normalized radii ($x = 0.3$ and $x = 0.4$). The corresponding A_f can be identified from the FM pulse where the three H&CD powers were varied. A first estimate of the B_f matrix is also obtained in the process. It is then refined, column by column, by using pulses where only one input was varied at a time, keeping A_f fixed and neglecting density variations. In a last step the density variations are included and the rest of the B_f matrix is filled. In this example, the first eigenvalue of A_f was found to be around $-14\ s^{-1}$, corresponding to a characteristic time of 0.07s. The second one was too close to the sampling frequency to be of particular relevance. A comparison between the original data obtained from the JETTO simulation and the data reconstructed from the identified state space model is shown on Fig. 3 (a common time offset has been removed). The fit between a set of original data, say *Y(i)* where *i* is a sample index, and the corresponding reconstructed data, *y(i)*, is characterized by a parameter,

$$f = 1 - \frac{\sum_{i=1}^{N}[Y(i) - y(i)]^2}{\sum_{i=1}^{N}[Y(i) - < Y >]^2} \quad (11)$$

where N is the number of samples and the bracket denotes an average over the samples. Fit parameters of the order of 70-90% (84% and 76% in this example) were found.

Another stage of the identification process provides an approximation for the A_s matrix (slow model) by considering the free dynamics of the system on the resistive time scale. This is obtained from the reference pulse where all the actuators are constant. The example shown here (Fig.4) concerns two elements of the Ψ vector corresponding to the same radii as before, $x = 0.3$ and $x = 0.4$. Excellent fit parameters of 98% and 95% are found. The smallest eigenvalue of the A_s matrix corresponds to a resistive time constant $\tau_R = 6.9$ s. In a further step, B_s is then identified using various SM pulses (see for instance the blue trace on Fig. 2) while keeping A_s fixed. Finally, in the ultimate step, the identification of C_s and D_s from SM pulses provides the last elements of a slow state space model governing the coupled evolution of the slow variables, Ψ, and the quasi-steady-state component of the kinetic variables, T_s. Note from Eq. (6d-6f) that, for consistency, D_s should ideally be equal to $[-(A_f)^{-1}. B_f]$ so that only C_s should be determined at this stage. This constraint can indeed be imposed during the identification. However, the determination of B_f generally contains large uncertainties and one has to bear in mind that the main request we must set on the models to be sought is that they fit the data as closely as possible, even at the expense of breaking some structural link between the reduced order models and the original full order model. Better fits were obtained without this constraint and typical results are shown on Fig.5 with fit parameters around 60-80%.

2.4.2. JET Experimental Data

In order to compare the degrees of accuracy that can be obtained using simulated and experimental data, and to make the necessary adaptations, the general strategy described above was also applied to some preliminary data taken on JET during the 2006 restart campaign. The plasma configuration was not optimized yet for advanced operation and was therefore different from the one used later during the dedicated identification and control experiments. But this was useful to check that the fast power modulations could be technically delivered by the H&CD systems, that the experimental data could be processed adequately, and to find ways of improving the identification algorithms so that they provide the required models for a reliable controller design. Again, these pulses were performed at constant plasma current so that only the three H&CD systems were considered as profile control actuators.The constant H&CD waveforms for the reference pulse, and the randomly modulated waveforms for two other pulses are shown on Fig. 6. In some pulses, the minimum time between power changes were chosen as 20ms for the LH and ICRH powers and 40 ms for NBI, and the systems responded satisfactorily to these modulated waveforms. As before we started with the

identification of the matrix A_s by considering only the reference pulse. On Fig. 7, the free dynamics of the Ψ Galerkin coefficients obtained from the model for the cubic splines with knots at x = 0.4, 0.5 and 0.6 are compared with the corresponding experimental data. The noise in the experimental data is due to the noise in the interfero-polarimetry and magnetic measurements used for the flux surface reconstruction. The fit parameters are in the range 60-70% and the eigenvalues of the identified A_s matrix correspond to time constants of 5.2s, 1.7s and 0.4s.

In a second step, B_s was identified using a pulse with slow modulations of the inputs, while fixing A_s as found above. A comparison between the model response and the experimental data is shown on Fig. 8. Fit parameters were found in the range 20-40%, yet the response of the model was satisfactory.

The fast model identification relies on experiments in which input powers must be modulated at high frequency (> 10Hz), and that forces A_f and B_f to be identified simultaneously. However, noting again from Eq. (6d-6f) that $D_s = -A_f^{-1}.B_f$, and imposing this constraint on the identification of A_f and B_f, one is able to limit the number of matrix elements to identify. By way of illustration, some results are displayed on Fig. 9 for three coefficients of the T_e profile corresponding to a cubic spline expansion with the same knots as previously for Ψ.

Identifying models of order 3 (sometimes up to order 4) has proved successful even when using noisy experimental data. It is however difficult to find models of higher order because the physical characteristic times (eigenvalues) which can possibly be identified are squeezed between the longest one, which is determined by the plasma size and temperature (resistive diffusion), and the time resolution of the data. So, when the state space data is taken locally, as was done above with Galerkin coefficients corresponding to the data at given normalized radii, the identified models cannot describe the profile dynamics over a very wide part of the plasma cross section. The order of the model to be identified increases when adding data from a larger number of radii. Controlling the values of $\Psi(x)$, $T_e(x)$, $q(x)$ or $\rho_{Te}^*(x)$ only at a few radii may be sufficient for some applications. But for global profile control purposes, it seems more judicious to look for models which can fairly describe the entire profiles while remaining of relatively low order. Such an approach will be described in the next section.

2.5. EXPERIMENTAL MODEL IDENTIFICATION USING GLOBAL PROFILE DATA WITH FOUR ACTUATORS

2.5.1. Open-loop Modulation Experiments in the Boundary Flux Control Mode

The first real-time profile control experiments performed during the 2006-2007 scientific campaign on JET were dedicated to a test of the proposed dynamic-model approach for the control of the safety factor profile. The chosen plasma scenario for these experiments was a high triangularity scenario (δ=0.45) with a toroidal field of 3T, a plasma current of 1.5MA, and an average plasma density of about $3.5.10^{19}$ m^{-3} [28].

An original feature of these experiments is that they were performed in a new mode of operation of the JET Extreme Shape Controller (XSC) [29], in which the PF system controls the plasma shape together with the *plasma boundary flux* [30], rather than together with the *plasma current*, as in the conventional XSC operation. The total plasma current is therefore allowed to float within some safety limits (± 0.5 MA). This will enable full control of the primary flux consumption for fully non-inductive steady state operation. For profile control purposes, it allows to include the edge safety factor (q_{95} or q_{edge}) into the q-profile control, so that the total plasma current is controlled by the full combination of the H&CD and ohmic (PF) systems in partially non-inductive operation, or only by the combination of the H&CD systems in fully non-inductive operation. The surface loop voltage (i.e. the boundary flux or more precisely some parts of the PF system) can therefore be treated as an additional profile control actuator. It is indeed the most powerful one to control the current density in the outer layers of the plasma ($x > 0.7$-0.8) or the q-profile during plasma current ramp-up.

To collect enough relevant data and identify a global plasma model, a number of specific open-loop experiments were performed in the early phase of the campaign. The available actuators were modulated randomly around a given set of input values corresponding to the so-called *reference state*. In order to modulate the surface loop voltage (V_{ext} in Eq. 2a) a modulation of the slope of the boundary flux was requested. The response of the XSC is shown in blue and the corresponding oscillations of the plasma current are shown on Fig.10b. The dynamic performance of the flux control strongly depends on the bandwidth of the power amplifier on the JET central solenoid (P1 coil) and the response time could not be reduced further. The loop voltage always exhibits a low frequency oscillation of a significant amplitude before settling, with a time lag of about 2 seconds, to its target value defined by the requested flux slope. This is not important for model identification as we can use the delivered value of V_{ext} as the input variable rather than the requested one, but it will be shown later to have severe consequences on the closed-loop behaviour of the controller (see section 4).

Typical modulations of the H&CD actuators are shown in Fig. 11 where only the NBI power is modulated, and Fig.12 where all the H&CD powers are modulated in the same pulse. Since the q-profile evolves on the (slow) resistive time scale, these modulations were done at relatively low frequencies, typically lower than 5Hz.

2.5.2. Transformation of the state variables from $\Psi(x)$ to $\iota(x) = 1/q(x)$

In order to use singular perturbation methods and optimal control techniques [25] to control the safety factor profile, or its inverse, $\iota(x)$, it is necessary to identify a state space model of the form given by Eq. (9-10). As explained in section 2.3, the intuitive justification for the existence of such a model (in the linear domain) lies in the fact that the variations of the toroidal magnetic field and flux should be small with respect to the variations of the poloidal flux, a conjecture that can be verified on the modulated data. Furthermore, if one can find the quantitative (linearized) mapping between the internal poloidal flux vector, Ψ, and the vector μ which describes the $\iota(x)$ profile, the constraints which are imposed on the Ψ-model (Eq.4) could be directly transposed onto the μ-

model (Eq.9). For instance, the column matrix, $B_{\Psi V}$, appearing on Eq.(2a) is in principle known from the derivation leading from Eq. (1) to Eq.(2a-2b) [appendix†A1]. Therefore, if an approximate Ψ-ι mapping exists, the particular column corresponding to the input V_{ext} in the matrix B_s of Eq. (9) is also known, at least approximately.

The real-time magnetic reconstruction used in these experiments is based on finding the best least-square fit of a large number of magnetic and interfero-polarimetry measurements, using polynomial parameterizations of the poloidal and toroidal flux functions [31]. This provides a rational fraction approximation for $\iota(x))=d\Psi(x)/d\Phi(x)$. We have therefore analysed the variations of the toroidal flux polynomial coefficients as a function of time during the modulation experiments and found that they do not vary substantially. Typical variations of $q(x)$, $\Psi(x)$ and $\Phi(x)$ can be seen on Fig.13a-13c for three different modulation pulses (Pulse No: 67871, 67872 and 68016) at two different times (t = 6s and t = 11s). It appears that the variations of the safety factor profile are indeed due, to a very large extent, to the variations of the internal poloidal flux. The toroidal flux function can therefore be assumed nearly constant when $q(x)$ varies, as long as the plasma configuration (shape) and the vacuum toroidal magnetic field do not change. Table 1 gives the average values of $\Phi'(x)=d\Phi/dx$ over many pulses and over time. These average values were used to calculate $\iota(x)$ in terms of $\Psi'(x)=d\Psi/dx$ and thus define an approximate Ψ-ι mapping around our reference state. The V_{ext} column of the B_s matrix then follows from the knowledge of $B_{\Psi V}$.

2.5.3. Singular Vectors of the Static Gain Matrix and Model Order Reduction

With a limited number of actuators, the family of achievable plasma states has only a few degrees of freedom. However it was shown in previous work [16-19] that a controller based on a least square minimization can achieve an adequate compromise in order to approach the requested plasma state at best. In any case, a complete set of magnetic and kinetic profiles which corresponds to a given stationary plasma state is never exactly known in every detail in advance, for it depends on a number of parameters which are not controlled or even not measured accurately (e.g. impurity profiles, etc ...). Therefore the *coherence* between the various target profiles that are *requested* by the operator cannot be assessed in advance and a least square control seems to be a good way to drive and maintain the plasma on the *closest coherent stationary state*. This does not preclude, of course, choosing a set of target profiles which are likely to be achievable, or nearly achievable, with the available actuators.

In previous experiments, the controller was based on a static model, i.e. on a singular value decomposition (SVD) of the static gain matrix, K, which was obtained experimentally by comparing several discharges with various, but constant, power levels. Modal (decoupled) control was achieved by retaining only a few principal components in the SVD (the only meaningful components), so that the controller gains obtained from the pseudo-inversion of K could have reasonable values [19].

This idea can be extended to the present dynamic-model approach in the following way. In order to come up with a state space model which governs the whole profiles (e.g. 10 spline coefficients)

while retaining only the most meaningful characteristics of the system, one can project the original data on an appropriate subspace of reduced dimension (say 3-4), identify the dynamics of the system within this subspace, and neglect the dynamics of the system within the supplementary (orthogonal) subspace. Several choices can be made to define the reduced state space and its basis vectors. The static gain matrix is an important element of the system and is indeed essential even for a controller based on a dynamic model. Another set of meaningful elements are the eigenvectors which correspond to the smallest eigenvalues (longest characteristic times) of the system. For the slow model, it seems preferable to put the emphasis on the static gain matrix, as was done in the previous static-model approach, and choose the first output singular vectors of K as a basis, so that the span of the reduced space contains the meaningful components of the static gain matrix. For the fast model, the static gain matrix is nil and an obvious choice would be to choose the first eigenvectors of the A_f matrix. In both cases an initial guess, for K and for A_f, is needed in order to select a state space basis in which to perform the reduced-order model identification. The process could be iterated if necessary.

In the example presented here, a slow model of order 3 was obtained for the dynamics of $\iota(x)$. A preliminary static gain matrix, $K^{(0)}$, was obtained from discharges having the same initial phase (plasma breakdown and current ramp-up) but in which an incremental step was applied on each of the actuators (H&CD powers and loop voltage) at the same time in the early heating phase and after a short plasma current flat top. The size of the output vectors was $n_\mu = 10$ and the size of the input vectors was $n_u = 4$ so that $K^{(0)}$ was a 10×4 matrix.

The principal components of $K^{(0)}$ were then obtained from its singular value decomposition,

$$K^{(0)} = W^{(0)} \cdot \Sigma^{(0)} \cdot V^{(0)+} = \left[W_1^{(0)} \quad W_2^{(0)} \quad \ldots \quad W_{n_\mu}^{(0)} \right] \cdot \Sigma^{(0)} \cdot \left[V_1^{(0)} \quad V_2^{(0)} \quad \ldots \quad V_{n_u}^{(0)} \right]^+ \qquad (12)$$

(throughout the paper, a + superscript indicates a transposed vector or matrix), and the state vectors, x(t), were restricted to be linear combinations of the first three singular vectors ($W_1^{(0)}$, $W_2^{(0)}$, $W_3^{(0)}$), chosen as a basis for the 3-dimensional state space. They correspond to the three largest singular values in $\Sigma^{(0}$. The entire μ-space of dimension n_μ can be represented onto a new orthogonal basis made of the complete set of singular vectors, $W_k^{(0)}$, with k = 1, 2, ..., n_μ. In this basis, the output vectors are represented by new column vectors, $x^{(0)}$, and the transformation between μ and $x^{(0)}$ reads $\mu = W^{(0)}. x^{(0)}$ and $x^{(0)} = W^{(0)+}. \mu$. The last components of $x^{(0)}$, corresponding to $k > 3$, are assumed to be irrelevant and are neglected. The basis functions of the 3-dimensional subspace on which the $\iota(x)$ profiles are thus projected can be constructed from the chosen cubic spline expansion (Fig.1a) using the elements of $W_1^{(0)}$, $W_2^{(0)}$, $W_3^{(0)}$ as the spline coefficients. They are displayed on Fig.14. A model of order $n_x = 3$ is then sought in which the state of the system is simply given by

$$x(t) = \left[W_1^{(0)} \quad W_2^{(0)} \quad W_3^{(0)} \right]^+ \cdot \mu(t) \qquad (13a)$$

and its dynamics is governed by an equation in the form

$$\dot{x}(t) = A_s \cdot x(t) + B_s \cdot u(t) \qquad (13b)$$

2.5.4. Reduced-Order Model Identification and Validation

Once the modulated $\iota(x)$ data (10 values at x = 0.1, 0.2...1, obtained from the real-time magnetic reconstruction [31]) has been projected onto the subspace of dimension 3 defined above (Eq. 13a), the slow model identification can proceed as before (section 2.4). The matrices A_s and B_s are identified to produce the best least square fit to the [u(t), x(t)] data, and the model output equation which provides the predicted $\mu(t)$ data for a set of inputs u(t), is assumed to be

$$\mu(t) = \left[W_1^{(0)} \quad W_2^{(0)} \quad W_3^{(0)} \right] \cdot x(t) \qquad (14)$$

with x(t) solution of Eq. (13b). The prediction is finally checked against the original $\mu(t)$ data.

Any higher-order modes of $\iota(x)$ with components $x_k^{(0)} \neq 0$ in the supplementary space (k = 4, 5, ..., 10) are assumed to have a fast stable dynamics, and are neglected owing to the fact that they have a negligible contribution in the SVD of the static gain matrix, $K^{(0)}$.

Comparing the experimental $\iota(x)$ data with predictions using the measured inputs and the identified model shows a good agreement. Typical results are shown here for three pulses which were used in the identification process : when only one actuator such as the NBI power or V_{ext} is modulated (Fig. 15 and 16, respectively) or when several actuators are modulated simultaneously (Fig. 17). Fit parameters in the range 40-70% were obtained for most cases. A better validation can be made by using pulses which were not used to identify the model. This was done for a number of pulses in another experimental session where softer variations of the inputs were obtained as a result of preliminary feedback tests, more typical of the real closed-loop experiments to come. An example is shown on Fig. 18 with fit parameters between 50% and 85%. Altogether, the slow model thus identified was therefore found to be sufficiently accurate for closed-loop q-profile control experiments to be attempted.

3. PROFILE CONTROLLER DESIGN AND CLOSED-LOOP SIMULATIONS

Given a two-time-scale model governing the evolution of a particular set of slow and fast variables [such as Ψ-T in Eq. (4-5) or $\mu-\rho$ in Eq. (7-10) or Eq. (13b-14)], we shall now describe the quasi-optimal profile controller (PC) which was implemented on JET to try and control, or regulate, the evolution of the selected variables. The PC design relies on the theory of singular perturbations applied to *optimal state control* [25], a technique which properly decouples the two time scales when the parameter ε (Eq. 2-3) is sufficiently small. With the present design, the PC should respond more rapidly to fast (kinetic) perturbations than it did with the former one [16-19], while converging towards a requested *target plasma state* on the resistive time scale.

The two-time-scale profile controller is organized around two main loops :

(i) a slow, *proportional-plus-integral* (PI), regulator control loop which, on the basis of the reduced-order slow model, drives the system towards the *coherent equilibrium state* which approaches at best the *prescribed target state* (see section 2.5.3), and regulates its evolution. On the same time scale, the variation of the slow components of the kinetic variables (e.g. ρ_s in eq. 9) is governed by the evolution of the magnetic variables and by the slow evolution of the actuators subject to the slow control law ;

(ii) a fast *proportional* control loop which ensures the stability of the kinetic variables on the plasma confinement time scale, bringing them back, at any time, on an evolving thermal quasi-equilibrium which is consistent with the evolving magnetic configuration. This loop regulates the transient behaviour of the kinetic variables when they are subject to rapid disturbances along the slow trajectory.

The generic behaviour of the system can be schematically described using the diagram displayed on Fig.19. Two typical trajectories are shown on this figure. In open-loop operation, with constant input powers, the system slowly relaxes towards equilibrium (blue trajectory). The particular equilibrium which corresponds to the reference input powers is called the *reference state*. When a different *target state* has been chosen (assumed on the figure to sit on the locus of coherent equilibrium states) and the two feedback loops are closed, the system responds according to a composite control law and the corresponding trajectory in state space (red trace) can be decomposed roughly in two parts. First, the fast components of the kinetic variables (e.g. ρ_f in eq. 10) are driven rapidly to zero, and are maintained near zero by the fast proportional feedback loop all along the control phase. On the occurrence of undesired fast transients, this brings the system back into a quasi-steady state that is consistent, at any time, with the slowly evolving magnetic state. Then, the system is driven slowly towards the target equilibrium state (or towards the closest coherent equilibrium state if the requested target is not a coherent equilibrium).

As already mentioned in section 2.5.1, the present profile controller has been designed to run in two operational modes: *(i)* the total plasma current can either be separately controlled together with the plasma shape through the PF system (normal use of the JET Extreme Shape Controller [29]), *(ii)* or more loosely by the PC (q-profile control) while the PF system controls the plasma shape *and* the boundary magnetic flux. In the former case (*i*), the PC provides *power requests* on the H&CD systems and the outer part of the q-profile is not included in the controlled variables. In the latter case (*ii*), the PC also provides a *boundary flux request*, so that part of the PF system (namely the central solenoid P1 coil) is used as an additional PC actuator. The maximum number of actuators is then four, and the controlled μ-vector should then contain the outmost value, $1/q_{edge}$, of the q-profile, a parameter which is representative of the total plasma current. In the present magnetic equilibrium reconstruction [31], the separatrix is approximated by a regular boundary with finite

safety factor at the edge, q_{edge}. If the magnetic separatrix were to be identified in the reconstruction process, the value of the safety factor on a magnetic surface encircling, say, 95% of the internal poloidal flux (q_{95}) could be used.

3.1. NEAR-OPTIMAL COMPOSITE CONTROL

Let us discard, for the moment, the plasma response to those components of the input vector that are not used as control actuators, such as the plasma density, n(t). Their variations will be considered later as disturbances (see section 3.2). The input vector u(t), of dimension n_u, then refers only here to the actuators, and we consider only the corresponding blocks of the two-time-scale state space models. They provide an accurate description of the system dynamics when the disturbance variables do not depart significantly from their reference values.

From now on, for the sake of clarity, we shall assume that the controlled profiles are $\iota(x)$ and $\rho^*_{Te}(x)$ so that the controlled variables are the vector set $[\mu, \rho]$ of dimensions (n_μ, n_ρ). We shall use the notation [x, z] for the magnetic and kinetic state vectors, of dimensions (n_x, n_z), leaving the possibility that the order of the identified models is lower than the number of variables in the vectors μ and ρ. Thus, the reduced two-time scale models will be assumed to stem from a full order model with the generic form :

$$\begin{bmatrix} \dot{x} \\ \varepsilon \dot{z} \end{bmatrix} = A \cdot \begin{bmatrix} x(t) \\ z(t) \end{bmatrix} + B \cdot u(t) \tag{15a}$$

$$\begin{bmatrix} \mu(t) \\ \rho(t) \end{bmatrix} = C \cdot \begin{bmatrix} x(t) \\ z(t) \end{bmatrix} \tag{15b}$$

where C can be a rectangular matrix (or the identity matrix if [x, z] = [μ, ρ]). We also define reduced variables:

$$X(t) = x(t) - x_\infty, \qquad Z(t) = z(t) - z_\infty, \qquad U(t) = u(t) - u_\infty \,, \tag{16a}$$

$$\tilde{\mu} = \mu - \mu_\infty \quad \text{and} \quad \tilde{\rho} = \rho - \rho_\infty \tag{16b}$$

where the subscript refers to a set of coherent final equilibrium values (note that, in the linearized model, x(t), z(t), u(t), μ(t) and ρ(t) are themselves variations of some raw variables, X(t), Z(t), U(t), M(t), R(t), with respect to their *reference values*, X_{ref}, Z_{ref}, U_{ref}, M_{ref}, R_{ref}, and so are x_∞, z_∞, u_∞, μ_∞ and ρ_∞. Given a requested target (or setpoint) for the output variables, $[\mu_{target}, \rho_{target}]$, the vectors $[\mu_\infty, \rho_\infty]$ represent the *closest coherent state achievable* by the controller according to the model (see section 2.5.3), and u_∞ represents the corresponding input vector. These vectors can be calculated

from a particular pseudo-inverse, K_{inv}, of the model static gain matrix, $K = - C.A^{-1}.B$, already mentioned in section 2.5.3, in such a way as to minimize a particular quadratic error involving the controlled variables (see section 3.1.1) :

$$u_\infty = K_{inv} \cdot \begin{bmatrix} \mu_{target} \\ \rho_{target} \end{bmatrix} \tag{17a}$$

$$\begin{bmatrix} \mu_\infty \\ \rho_\infty \end{bmatrix} = K \cdot u_\infty = K \cdot K_{inv} \cdot \begin{bmatrix} \mu_{target} \\ \rho_{target} \end{bmatrix} \tag{17b}$$

Given a singularly perturbed dynamical system under the generic form of Eq. (15a-15b), with a magnetic state vector, $x=x_s$, and a kinetic state vector, $z=z_s+z_f$, and under a set of reasonable controllability conditions [25], the theory of linear-quadratic optimal control can be adapted to find a slow control law,

$$U_s(t) = - G_s . X(t) \tag{18a}$$

and a fast one,

$$U_f(t) = - G_f . Z_f(t) \tag{18b}$$

so that the *composite feedback control*, $U(t) = U_s(t) + U_f(t)$, is stabilizing and provides the best $O(\varepsilon^2)$ solution to the minimization of the cost functional :

$$J[U(t)] = \int_0^\infty dt \left\{ \begin{bmatrix} X^+(t) & Z^+(t) \end{bmatrix} \cdot Q \cdot \begin{bmatrix} X(t) \\ Z(t) \end{bmatrix} + U^+(t) \cdot R \cdot U(t) \right\} \tag{19}$$

where Q and R are positive-semidefinite and positive-definite matrices, respectively. When these matrices are properly tuned, the controller offers a good compromise between performance and cost in terms of actuator power.

As it stands in Eq. 18a, the slow feedback control law provides only proportional control and therefore does not ensure that one achieves $x \rightarrow x_\infty$ without a significant steady state offset. A proportional-plus-integral control is required for this to be guaranteed. For this purpose, we introduce an extra state vector defined as [32]

$$\zeta = K_\zeta \cdot \int_0^t \begin{bmatrix} \tilde{\mu}(t) \\ \tilde{\rho}(t) \end{bmatrix} d\tau \tag{20}$$

where K_ζ is an arbitrary matrix of dimensions $(n_u \times n_x)$, which is $O(1)$ in the ε ordering (for instance, one can choose $K_\zeta = K_{inv}$). We thus add to the original system, the additional dynamical equation,

$$\dot{\zeta} = K_\zeta \cdot C \cdot \begin{bmatrix} X(t) \\ Z(t) \end{bmatrix} . \tag{21}$$

Applying conventional optimal control to the minimization of a new functional,

$$J[U(t)] = \int_0^\infty dt \left\{ \begin{bmatrix} X^+(t) & Z^+(t) \end{bmatrix} \cdot Q \cdot \begin{bmatrix} X(t) \\ Z(t) \end{bmatrix} + \alpha_\zeta^2 \, \zeta^+(t) \cdot \zeta(t) + U^+(t) \cdot R \cdot U(t) \right\} \qquad (22)$$

with α_ζ real would then provide the desired PI control law,

$$U(t) = -G \cdot \begin{bmatrix} X(t) \\ Z(t) \\ \zeta(t) \end{bmatrix} = -G_1 \cdot \begin{bmatrix} X(t) \\ Z(t) \end{bmatrix} - G_2 \cdot \int_0^t K_\zeta \cdot C \cdot \begin{bmatrix} X(t) \\ Z(t) \end{bmatrix} dt \quad . \qquad (23)$$

The dynamical system [X, Z, ζ] has also the required structure for applying the singular perturbation analysis and can therefore be reduced using the two-time-scale approximation. K_ζ being *O*(1) in the ε ordering, Eq. (21) has a slow dynamics and ζ is obviously a slow variable. But, before giving a detailed description of the two-time-scale controller design, some specific properties regarding the achievable plasma states as well as the controllability and observability of the system must be discussed. This will be done in the following sections (3.1.1 to 3.1.3). Then, in sections 3.1.4 and 3.1.5, we shall look for the composite control law, $U(t) = U_s(t) + U_f(t)$, which provides the best $O(\varepsilon^2)$ solution to the minimization of the functional J[U(t)] (Eq.22).

3.1.1. Choice of K_z and Closest Coherent Achievable State

As already noted before, because of the infinite dimensionality of the system and the limited number of actuators, the controller cannot achieve *every* possible $[\iota(x), \rho^*_{Te}(x)]$ final state. Once a model is known, there exist a family of identified equilibrium states that are generated by all possible input vectors, u_∞. They are artistically represented by a thick trace on Fig. 19. The discrete model identification procedures described in section 2 implied that they belong to the span of the basis functions, $a_i(x)$ and $b_i(x)$ (Fig. 1), an assumption which is largely consistent with experimental accuracy. The distributed target profiles $[\iota_{target}(x), \rho^*_{Te,target}(x)]$ will also be defined by their Galerkin coefficients, $[\mu_{target}, \rho_{target}]$, on this set of basis functions (see appendix A1.2). But the reduced variables, $[\tilde{\mu}, \tilde{\rho}]$ were defined in terms of some achieved stationary state, $[\mu_\infty, \rho_\infty]$, which needs to be specified once an arbitrary target state has been chosen. In Eq. (18) we have defined a coherent achievable state by applying the operator $(K.K_{inv})$ to the target state, where K_{inv} is a pseudo-inverse of the static gain matrix, K. This pseudo-inverse is not unique though, and it must be defined in terms of a minimization criterion. We therefore define the *closest coherent achievable state* $[\mu_\infty, \rho_\infty]$, within the family of equilibrium states given by the model, as the one that corresponds to the input vector, u_∞, for which the quadratic functional,

$$I_\infty = \frac{1}{x_2 - x_1} \int_{x_1}^{x_2} \left[\iota_\infty(x) - \iota_{target}(x) \right]^2 dx + \frac{\lambda_{ITB}}{x_4 - x_3} \int_{x_3}^{x_4} \left[\rho^*_{Te,\infty}(x) - \rho^*_{Te,target}(x) \right]^2 dx \qquad (24)$$

is minimum. The parameter λ_{ITB} is a weighting parameter which is zero for magnetic control only, and whose order of magnitude should be around 10^3-10^4 when the temperature gradient is to be controlled as well [$\rho^*_{Te}(x)$ is about 1.4×10^{-2} at the formation of an ITB in JET].

The static gain matrix, K, of the identified model relates the input vector, u_∞, to the vector coefficients, $[\mu_\infty, \rho_\infty]$, of the achieved profiles, $[\iota_\infty(x), \rho^*_{Te,\infty}(x)]$. Inserting the relation between u_∞ and $[\iota_\infty(x), \rho^*_{Te,\infty}(x)]$ into the functional (24), one finds

$$I_\infty [K, u_\infty] = \left\{ K \cdot u_\infty - \begin{bmatrix} \mu_{target} \\ \rho_{target} \end{bmatrix} \right\}^+ \cdot \Delta^+ \cdot \Delta \cdot \left\{ K \cdot u_\infty - \begin{bmatrix} \mu_{target} \\ \rho_{target} \end{bmatrix} \right\} \tag{25}$$

where the product $(\Delta^+ . \Delta)$ is the Cholesky decomposition of a block-diagonal matrix

$$\Pi = \begin{bmatrix} \Pi_\mu & 0 \\ 0 & \lambda_{ITB}\,\Pi_\rho \end{bmatrix} = \Delta^+ \cdot \Delta = \begin{bmatrix} \Delta_\mu & 0 \\ 0 & \Delta_\rho \end{bmatrix}^+ \cdot \begin{bmatrix} \Delta_\mu & 0 \\ 0 & \Delta_\rho \end{bmatrix} \tag{26}$$

and Π_μ and Π_ρ are matrices whose elements are scalar products of the basis functions :

$$\left[\Pi_\mu\right]_{i,j} = \int_{x_1}^{x_2} a_i(x)\, a_j(x)\, dx \qquad \text{and} \quad \left[\Pi_\rho\right]_{i,j} = \int_{x_3}^{x_4} b_i(x)\, b_j(x)\, dx \quad . \tag{27}$$

After performing a *singular value expansion* of $(\Delta . K)$,

$$\Delta \cdot K = \hat{K} = \hat{W} \cdot \Sigma \cdot \hat{V}^+ \tag{28}$$

it is easy to show [19] that the input vector that minimizes $I_\infty [K, u_\infty]$ is :

$$u_\infty = \hat{V}_{tr} \cdot \Sigma_{tr}^{-1} \cdot \hat{W}_{tr}^{+} \cdot \Delta \cdot \begin{bmatrix} \mu_{target} \\ \rho_{target} \end{bmatrix} = \hat{V}_{tr} \cdot \Sigma_{tr}^{-1} \cdot W_{tr}^{+} \cdot \Pi \cdot \begin{bmatrix} \mu_{target} \\ \rho_{target} \end{bmatrix} \tag{29}$$

where $\hat{W}, \Sigma$ and $\hat{V}$ have been properly truncated (subscript "tr") to retain only the singular vectors which correspond to finite singular values, and where $W_{tr} = \Delta^{-1} \cdot \hat{W}_{tr}$. It is to be noted that, by definition, the norm of the singular vectors $\hat{W}$ and $\hat{V}$ is one, and the decomposition (28) depends on the units in which the input and output variables are measured. For the norm to be meaningful, these units ought to be chosen (before performing the SVD) in relation to the typical variations of the output variables or, for the input powers and loop voltage, in relation to the available headroom with respect to their reference values.

Now, because of unavoidable redundancies in the respective actions of the available actuators, K is a rectangular matrix whose condition number (the ratio of the largest to the smallest singular value) is generally much larger than one [19]. Hence, target states that differ very slightly could result, through the pseudo-inversion of K, in large variations in u_∞. Or, in other words, trying to approach a requested target state too closely may result in large power requests on different actuators which nearly annihilate each other, while a different set of smaller input powers would provide a

slightly different, yet quite satisfactory, stationary solution $[\mu_\infty, \rho_\infty]$. Therefore, as in Ref. [19], we shall retain, in the truncated singular value expansion of $\hat{K}$, only the n_{SV} most significant terms $[n_{SV} \leq \min(n_u, n_x)]$, neglecting those corresponding to outstandingly small (irrelevant) singular values. In doing so, we use an approximation of the identified static gain matrix,

$$K_T = \Delta^{-1} \cdot \hat{K}_T = \Delta^{-1} \cdot \hat{W}_T \cdot \Sigma_T \cdot \hat{V}_T^{+} = W_T \cdot \Sigma_T \cdot \hat{V}_T^{+} \tag{30}$$

which lies within the uncertainties of the model identification and which can be considered as an alternative for the static gain matrix of the system. The input vector

$$u_\infty = \hat{V}_T \cdot \Sigma_T^{-1} \cdot \hat{W}_T^{+} \cdot \Delta \cdot \begin{bmatrix} \mu_{target} \\ \rho_{target} \end{bmatrix} = \hat{V}_T \cdot \Sigma_T^{-1} \cdot W_T^{+} \cdot \Pi \cdot \begin{bmatrix} \mu_{target} \\ \rho_{target} \end{bmatrix} \tag{31}$$

is a solution to the minimization of $I_\infty [K_T, u_\infty]$ and n_{SV} can be chosen so that Eq. (31) yields steady state actuator values which are†“reasonable” ($\left\|\Sigma_T^{-1}\right\| \leq \left\|\Sigma_{tr}^{-1}\right\|$).
An appropriate choice for K_{inv}, is therefore

$$K_{inv} = \hat{V}_T \cdot \Sigma_T^{-1} \cdot W_T^{+} \cdot \Pi \tag{32}$$

and the *closest coherent achievable state* is defined as

$$\begin{bmatrix} x_\infty \\ z_\infty \end{bmatrix} = -A^{-1} \cdot B \cdot u_\infty = -A^{-1} \cdot B \cdot K_{inv} \cdot \begin{bmatrix} \mu_{target} \\ \rho_{target} \end{bmatrix} \tag{33a}$$

and

$$\begin{bmatrix} \mu_\infty \\ \rho_\infty \end{bmatrix} = K_T \,.\, u_\infty \bullet H \; K_T \,.\, u_\infty = K_T \cdot K_{inv} \cdot \begin{bmatrix} \mu_{target} \\ \rho_{target} \end{bmatrix} \tag{33b}$$

Under an optimal control law such as Eq. (23), with $K_\zeta = [K_{\zeta\mu} \; K_{\zeta\rho}]$, some particular combinations, $K_{\zeta\mu} \cdot \tilde{\mu} + K_{\zeta\rho} \cdot \tilde{\rho}$, of the reduced variables would vanish without any offset when the system has reached a stationary state, thanks to the PI control. This implies that, in steady state, the controller achieves

$$K_\zeta \cdot \begin{bmatrix} \mu \\ \rho \end{bmatrix} \;\rightarrow\; K_\zeta \cdot \begin{bmatrix} \mu_\infty \\ \rho_\infty \end{bmatrix} \tag{34}$$

i.e.

$$K_\zeta \cdot K_T \cdot u \;\rightarrow\; K_\zeta \cdot K_T \cdot u_\infty \qquad . \tag{35}$$

Now, with the choice

$$K_\zeta = W_T^{+} \cdot \Pi, \tag{36}$$

one has $K_\zeta \cdot K_T = \Sigma_T \cdot \hat{V}_T^{+}$, and this also implies that $K_T.u \rightarrow K_T.u_\infty$, i.e. $[\mu, \rho] \rightarrow [\mu_\infty, \rho_\infty]$. Note however that the rank of K_T is n_{SV} so that the final value of u(t) is not necessarily equal to u_∞ when n_{SV} is smaller than n_u. It can differ from u_∞ by any combination of the input vectors which belong to the null space of K_T. Yet the norm of K_{inv} (Eq. 32) can be significantly reduced when n_{SV} is chosen judiciously ($\left\|\Sigma_T^{-1}\right\| \leq \left\|\Sigma_{tr}^{-1}\right\|$). The controller gains then take on reasonable values and the final value of u(t) does not depart so much from u_∞. It is also a solution to the minimization of I_∞ $[K_T, u]$, and yields the same minimum value.

Another consequence of Eq. (36) is that $(K_\zeta.K_T.K_{inv}) = K_\zeta$, so that Eq. (33) also entails

$$K_\zeta \cdot \begin{bmatrix} \mu_{target} \\ \rho_{target} \end{bmatrix} = K_\zeta \cdot \begin{bmatrix} \mu_\infty \\ \rho_\infty \end{bmatrix}, \tag{37}$$

and, if one were to use conventional optimal control, the PI control law (Eq. 23) could be written in terms of the requested target state :

$$U(t) = -G \cdot \begin{bmatrix} X(t) \\ Z(t) \\ \zeta(t) \end{bmatrix} = -G_p \cdot \left\{ \begin{bmatrix} x(t) \\ z(t) \end{bmatrix} + A^{-1} \cdot B \cdot K_{inv} \cdot \begin{bmatrix} \mu_{target} \\ \rho_{target} \end{bmatrix} \right\} - G_i \cdot \int_0^t K_\zeta \cdot \begin{bmatrix} \mu(t) - \mu_{target} \\ \rho(t) - \rho_{target} \end{bmatrix} dt \tag{38}$$

3.1.2. System Controllability and Stabilizability

The generic model structure derived in appendix A1.2 naturally yields a state space whose dimension is as large as the number of trial basis functions. However, when using experimental data, the model identification techniques described in section 2 can hardly provide models whose order exceeds 3 or 4. To be consistent with our generic model structure, models of higher order could be artificially constructed by completing the selected subspace basis with a set of orthonormal vectors in the supplementary subspace (see section 2.5.4), and imposing arbitrary large negative eigenvalues and zero static gain to the new state components whose dynamics have not been identified.

On the contrary, let us now assume that some identification method has generated a slow and a fast model which fit the system dynamics satisfactorily, with a large number of state variables. If the highest order modes are stable, they often exhibit fast but negligible responses to the inputs and nearly zero static gains. When some eigenmodes have zero static gains, they cannot be influenced by the inputs and the system is not *completely controllable,* in the academic sense. With small static gains, some high-order modes may only be *weakly controllable*. They generally play little role in the slow dynamics of the system, though, and their control is not essential. In these cases, a reduced-order controllable system may be deduced from the original one by discarding the highest order modes (see appendix A3), perhaps at the expense of a slight shift in the definition of the slow and the fast time scales. Besides, with a larger number of modes, it is also likely that the eigenvalue spectra of the slow and fast models overlap [i.e. that some "slow" eigenvalues are $O(\varepsilon^{-1})$ larger than the smallest one], or that the characteristic times of some of the fast model eigenmodes fall

below the controller sampling time so that their dynamics can be discarded. Altogether, if the available models have high orders, it may sometimes be possible and preferable to construct new reduced-order systems that are completely controllable and/or more consistent with the two-time-scale ordering. A general method to construct such reduced-order models is described in appendix A3.

Now, even for a low-order system for which all the identified modes have finite static gains, the question of the system controllability arises. The *controllability* and the *stabilizability* of the real singularly perturbed system cannot be assessed directly when the identification of the full order model is not possible. But, for ε sufficiently small, they can be deduced from the controllability and stabilizability of the separate reduced-order models obtained within the two-time-scale approximation [25]. The slow system associated with Eq. (15a-15b) will be written under the general form :

$$\dot{x} = A_s\, x + B_s\, u_s \tag{39a}$$

$$\begin{bmatrix} \mu \\ \rho_s \end{bmatrix} = \begin{bmatrix} C_{\mu,s} \\ C_{\rho,s} \end{bmatrix} \cdot x + \begin{bmatrix} D_{\mu,s} \\ D_{\rho,s} \end{bmatrix} \cdot u_s = C_s \cdot x + D_s \cdot u_s \tag{39b}$$

so that

$$K = -\,C_s \cdot A_s^{-1} \cdot B_s + D_s\,, \tag{39c}$$

and, with $z = z_s + z_f$ and $\rho = \rho_s + \rho_f$, the fast system will be written as

$$\dot{z}_f = A_f\, z_f + B_f\, u_f \tag{40a}$$

$$\rho_f = C_f \cdot z_f\,. \tag{40b}$$

The i^{th} eigenvalue, $\lambda_{s,i}$, of the slow system is controllable when

$$\text{Rank}\left[(\lambda_{s,i} \cdot Id_{n_x} - A_s) \quad B_s\right] = n_x \tag{41a}$$

where Id_{n_x} stands for the identity matrix of order n_x, and the j^{th} eigenvalue, $\lambda_{f,j}$, of the fast system is controllable when

$$\text{Rank}\left[(\lambda_{f,j} \cdot Id_{n_z} - A_f) \quad B_f\right] = n_z\,. \tag{41b}$$

If, after completing this test on the identified models, they are completely controllable [i.e. all their eigenvalues are controllable], then we can infer that the original system is likely to be controllable. Now, if they are not completely controllable even after order reduction, but all uncontrollable

eigenvalues are stabilizable (i.e. either stable or stabilizable through feedback), optimal control can still be used to find the control, U(t), that depends on the *observable* states and minimizes an objective functional of the input and output variables. We shall always assume here that the system is *stabilizable* so that an appropriate controller can be designed. Besides, during the various experiments dedicated to model identification (section 2), no particular instability was observed around the chosen reference state, and all the identified eigenvalues were stable.

3.1.3. Output Variables, System Observability and Controlled States

In control engineering, the *output variables* of a state space model generally depend on the states of the system *as well as* on the values of the input variables. Here, thanks to the physical basis underlying the original, singularly perturbed, system (see sections 2.3 and 2.5.2), we have been able to assume that the output variables of interest are only linked to the state variables, as in Eq. (15b). With such output equations in the original full-order system, despite the fact that an input-dependent term does appear in the slow system (Eq. 39b), the two-time-scale controller can be based on *optimal state control* rather than *output-feedback control* for which the closed-loop stability of the real system would not always be guaranteed, even when ε is small [25].

Let us now assume that, for some particular applications, one controls only a few selected components, $[\mu_c, \rho_c]$, of the full μ and ρ vectors, with no particular interest in the global control of the profiles. For such a purpose, the K and Δ matrices, as well as the target vectors can indeed be truncated adequately in the functional, I_∞, of Eq. (25) which is then an approximate representation of Eq. (24). With output vectors $[\mu_c\,,\ \rho_c = \rho_{s,c}+\rho_{f,c}]$ of dimensions $\left[n_{\mu_c}, n_{\rho_c}\right]$, governed by output equations

$$\begin{bmatrix} \mu_c(t) \\ \rho_{s,c}(t) \end{bmatrix} = C_{s,c} \cdot x(t) + D_{s,c} \cdot u_s(t) \quad \text{and} \quad \rho_{f,c}(t) = C_{f,c} \cdot z_f(t), \tag{42}$$

the observability of the states x and z_f requires that

$$\text{Rank} \begin{bmatrix} (\lambda_{s,i} \cdot Id_{n_x} - A_s) \\ C_{s,c} \end{bmatrix} = n_x \qquad \text{for } i = 1, 2, ..., n_x \tag{43a}$$

and

$$\text{Rank} \begin{bmatrix} (\lambda_{f,j} \cdot Id_{n_z} - A_f) \\ C_{f,c} \end{bmatrix} = n_z \qquad \text{for } j = 1, 2, ..., n_z. \tag{43b}$$

All states may not be *observable* if the number of measured outputs is too small. As in section 3.1.2, if the available models have high orders and all the eigenmodes are not observable, one can possibly construct reduced-order models by retaining the slowest eigenvalues only, so that they are all observable from the selected output variables (or from a minimum set of measured output variables which includes the selected ones). The general procedure described in appendix A3 can again be used for this purpose, and the new reduced-order models should then be validated against the data.

We shall then assume that one can always measure at least a number of output variables equal to the order of the models, and those for which Eq. (42) can be inverted. This obviously ensures the observability of the reduced-order systems, and therefore of the real, full-order, system if ε is small enough [25].

3.1.4. The Slow Proportional-Integral Feedback Loop

Leaving the possibility that $x \neq \mu$, and using the additional variable, ζ, defined in Eq. (20), let us now write the slow model in terms of the reduced variables. It involves only the slow variables (X, ζ, $\tilde{\mu}$, $\tilde{\rho}_s$, U_s) since the fast variables (z_f, μ_f, ρ_f, U_f) vanish in the quasi-static approximation :

$$\dot{X} = A_s\, X + B_s\, U_s \tag{44a}$$

$$\dot{\zeta} = K_\zeta \cdot \begin{bmatrix} \tilde{\mu} \\ \tilde{\rho}_s \end{bmatrix} = \left(K_{\zeta\mu} + K_{\zeta\rho} \cdot C_s\right) \cdot X + \left(K_{\zeta\rho} \cdot D_s\right) \cdot U_s \tag{44b}$$

$$\begin{bmatrix} \tilde{\mu} \\ \tilde{\rho}_s \end{bmatrix} = \begin{bmatrix} C_{\mu,s} \\ C_{\rho,s} \end{bmatrix} \cdot X + \begin{bmatrix} D_{\mu,s} \\ D_{\rho,s} \end{bmatrix} \cdot U_s = C_s \cdot X + D_s \cdot U_s \tag{44c}$$

where $K_\zeta = [K_{\zeta\mu}\ K_{\zeta\rho}]$. The particular case, $x = \mu$, is obtained in a trivial way by choosing $C_{\mu,s} = Id_{n_\mu}$ and $D_{\mu,s} = 0$.

We consider the control law, $U_{opt}(t)$, which, by applying conventional optimal control to the real system (assumed stabilizable), would minimize the quadratic functional given in Eq. (22). In order to keep the number of tuning parameters reasonably small, the following choices were fixed :

i) $$Q = C^+ \cdot \Delta^+ \cdot \Delta \cdot C \tag{45}$$

where C has been defined in Eq. (15b) and Δ has been defined in Eq. (26-27) in terms of the basis functions, $a_i(x)$ and $b_i(x)$, shown on Fig. (1), *ii)* $K_\zeta = W_T^+ . \Pi$, to take advantage of Eq. (37), and *iii)* R is chosen diagonal. With Eq. (45), the first term in the quadratic (22) represents the radially integrated squared profile error (see section 3.1.1). Thus, λ_{ITB}, α_ζ and the diagonal elements of R are the only (n_u+2) tuning parameters.

As shown in [25], the near-optimal, $O(\varepsilon^2)$, two-time-scale approximation of $U_{opt}(t)$ is provided by a composite control law, $U(t) = U_s(t) + U_f(t)$. Defining

$$Y(t) = \begin{bmatrix} \Delta \cdot C & 0 \\ 0 & \alpha_\zeta \end{bmatrix} \cdot \begin{bmatrix} X(t) \\ Z(t) \\ \zeta(t) \end{bmatrix} = \begin{bmatrix} \Delta_\mu & 0 & 0 \\ 0 & \Delta_\rho & 0 \\ 0 & 0 & \alpha_\zeta \end{bmatrix} \cdot \begin{bmatrix} \mu(t) \\ \rho(t) \\ \zeta(t) \end{bmatrix} \quad , \tag{46}$$

the integrand in Eq. (22) reads : $Y(t)^+ . Y(t) + U(t)^+ . R . U(t)$. Using Eq. (44c), we obtain in the quasi-static limit,

$$Y_s(t) = \begin{bmatrix} \Delta & 0 \\ 0 & \alpha_\zeta \end{bmatrix} \cdot \begin{bmatrix} C_s \cdot X(t) + D_s \cdot U_s(t) \\ \zeta(t) \end{bmatrix} \tag{47}$$

The slow component of the near-optimal control law is then the one that minimizes

$J_s[U_s(t)] =$

$$\int_0^\infty dt \left\{ \left[X(t)^+ \; \zeta(t)^+ \right] \cdot M_0^+ \cdot M_0 \cdot \begin{bmatrix} X(t) \\ \zeta(t) \end{bmatrix} + 2\, U_s^+(t) \cdot N_0^+ \cdot M_0 \cdot \begin{bmatrix} X(t) \\ \zeta(t) \end{bmatrix} + U_s^+(t) \cdot R_0 \cdot U_s(t) \right\} \tag{48}$$

where the matrices M_0, N_0 and R_0 are defined by

$$M_0 = \begin{bmatrix} \Delta \cdot C_s & 0 \\ 0 & \alpha_\zeta \, Id_{n_u} \end{bmatrix} \tag{49a}$$

$$N_0 = \begin{bmatrix} \Delta \cdot D_s \\ 0 \end{bmatrix} \tag{49b}$$

$$R_0 = R + N_0^+ . \, N_0 \, . \tag{49c}$$

It reads :

$$U_s(t) = -\begin{bmatrix} G_x & G_\zeta \end{bmatrix} \cdot \begin{bmatrix} X(t) \\ \zeta(t) \end{bmatrix} = -G_x \cdot X(t) - G_\zeta \cdot K_\zeta \cdot \int_0^t \begin{bmatrix} \tilde{\mu}(t) \\ \tilde{\rho}(t) \end{bmatrix} dt \tag{50}$$

or, when the model has been identified in such a way (see sections 2.5.3-2.5.4) that the states are observable and can be deduced from the outputs, e.g. as $x(t) = \Gamma_\mu . \, \mu(t)$,

$$U_s(t) = -G_x \cdot \Gamma_\mu \cdot \tilde{\mu}(t) - G_\zeta \cdot K_\zeta \cdot \int_0^t \begin{bmatrix} \tilde{\mu}(t) \\ \tilde{\rho}(t) \end{bmatrix} dt \tag{51}$$

The near-optimal gain matrix, $[G_x \; G_\zeta]$, can be found from the unique solution of the Riccati equation which is associated with the minimization of $J_s[U_s(t)]$ (Eq. 48), and it ensures the stability of the slow variables under closed-loop operation.

With K_ζ given by Eq. (36), the gain matrices read

$$G_{sp} = \begin{bmatrix} G_x \cdot \Gamma_\mu & O(n_u, n_x + n_\rho) \end{bmatrix} \quad \text{and} \quad G_{si} = G_\zeta \cdot W_T^+ \cdot \Pi, \tag{52}$$

where O(i, j) is a (i × j) matrix of zeros, and using the results of section 3.1.1, Eq. (51) can finally be written as

$$U_s(t) = -G_{sp} \cdot \left\{ \begin{bmatrix} \mu(t) \\ \rho(t) \end{bmatrix} - K \cdot K_{inv} \cdot \begin{bmatrix} \mu_{target} \\ \rho_{target} \end{bmatrix} \right\} - G_{si} \cdot \int_0^t \left\{ \begin{bmatrix} \mu(t) \\ \rho(t) \end{bmatrix} - K \cdot K_{inv} \cdot \begin{bmatrix} \mu_{target} \\ \rho_{target} \end{bmatrix} \right\} dt \tag{53}$$

Of course, the product ($K.K_{inv}$) appears here because the controller is meant to achieve the closest coherent achievable state, $[\mu_\infty, \rho_\infty]$, as defined in section 3.1.1. However, this hypothetical plasma state and the corresponding input vector were deduced from the static gain of a *model* obtained experimentally, with large uncertainties. They may not coÔncide exactly with the state and inputs which are achieved by the real plasma under the control defined in Eq. (53). Hence, unless the profiles corresponding to $[\mu_\infty, \rho_\infty]$ are very different from those corresponding to $[\mu_{target}, \rho_{target}]$ (e.g. if n_{SV} needs to be chosen much smaller than n_u), the product ($K.K_{inv}$) may often be omitted. The essential features which must be retained from the model appear in the computation of the gains (Eq. 52), and the achieved state will still lie within experimental accuracy of both $[\mu_\infty, \rho_\infty]$ and $[\mu_{target}, \rho_{target}]$, perhaps even closer to the requested target than $[\mu_\infty, \rho_\infty]$ is.

3.1.5. The Fast Proportional Feedback Loop

By definition, the fast variables have zero static limit so that $X_f = x_f$, $Z_f = z_f$, $\tilde{\rho}_f = \rho_f$ and $U_f = u_f$, and therefore the fast model associated with Eq. (44a-c) is given by Eq. (40a-b) with

$$z_f = z - z_s = Z - Z_s \qquad \text{and} \quad \rho_f = \rho - \rho_s = \tilde{\rho} - \tilde{\rho}_s \qquad . \tag{54}$$

From Eq. (46), the only fast element of Y(t) is

$$Y_f(t) = \Delta_\rho \cdot C_f \cdot z_f(t) \tag{55}$$

The fast component of the near-optimal control law, which is to supplement Eq. (53) in order to minimize the functional (22) to order $O(\varepsilon^2)$, is then the one that minimizes

$$J_f[u_f(t)] = \int_0^\infty dt \left\{ z_f(t)^+ \cdot \left[C_f{}^+ \cdot \Delta_\rho{}^+ \cdot \Delta_\rho \cdot C_f \right] \cdot z_f(t) + u_f^+(t) \cdot R \cdot u_f(t) \right\} \tag{56}$$

It is given by

$$u_f(t) = U_f(t) = -G_z \cdot z_f(t) = -G_z \cdot \left[z(t) - z_s(t) \right] \qquad . \tag{57}$$

When the model has been identified in such a way (see sections 2.5.3-2.5.4) that the states are observable and can be deduced from the outputs, e.g. as $z(t) = = \Gamma_\rho . \rho(t)$, it becomes

$$u_f(t) = U_f(t) = -G_z \cdot \Gamma_\rho \cdot \rho_f(t) = -G_z \cdot \Gamma_\rho \cdot \left[\rho(t) - \rho_s(t) \right] \tag{58}$$

The optimal gain matrix, G_f, is found again from the unique solution of the Riccati equation which is associated with the minimization of $J_f[u_f(t)]$, and ensures the stability of the fast variables under closed-loop operation. In terms of $[\mu, \rho]$, and using Eq.(39b), the fast control law finally reads :

$$u_f(t) = -G_f \cdot \rho_f(t) = -G_f \cdot \left[\rho(t) - \rho_s(t)\right] = -G_f \cdot \left[\rho(t) - C_{\rho,s} \cdot \Gamma_\mu \cdot \mu(t) - D_{\rho,s} \cdot u_s(t)\right] \quad (59)$$

with

$$G_f = G_z \cdot \Gamma_\rho \quad (60)$$

Upon application of the composite control law, $u(t) = u_s(t) + u_f(t)$, and forε sufficiently small, the closed-loop system is stable and the value reached by the functional J[U(t)] (Eq. 22) is$O(\varepsilon^2)$ close to the minimum which would be obtained under optimal control of the original system [25]. Conventional optimal control is therefore recovered when the ratio of the thermal confinement time to the resistive diffusion time tends to zero so that the small-ε approximate model holds.

3.2. Feedforward Disturbance Rejection

The structure of the dynamic plasma model was obtained, in section 2.1, from the analysis of a set of coupled transport equations which are assumed to govern the plasma evolution. It was then observed that the plasma density appears in the right-hand-side of the dynamical model equations (2a-2b). Therefore it cannot be discarded in the model identification procedure unless its average value and/or radial profile does not depart significantly from the density profile of the so-called reference plasma state. This was indeed taken into account in the model identification procedures described in section 2 where the local density at some radii or the line-averaged density along some chords were included in the input vector [see for instance the model inputs shown on Fig. (11-12)]. A density vector, $n(t) = n_s(t) + n_f(t)$, was thus included in the vector $u(t) = u_s(t) + u_f(t)$ in addition to the H&CD (and possibly PF) actuators, and the plasma response to changes in the density was also identified.

The two-time-scale near-optimal controller design described above assumes that the input vector, u(t), only consists of the control actuators. Other model inputs are assumed to take on their reference values and the corresponding columns of the model matrices have been discarded. For instance the static gain matrix considered in section 3.1 is deduced from the full model static gain by removing the columns corresponding to the density inputs (and to any actuator which would not participate in the control). Now, if the power delivered by an actuator which is not used for control purposes can in principle be set to its reference value during the whole control phase, it is generally not so for the plasma density which is subject to neutral beam fuelling and to various uncontrolled plasma perturbations (e.g. edge localized modes (ELM), MHD events, etc ..). From the control point of view, any variation of the plasma density will therefore be considered as an external disturbance. It can have a physical impact on the profile evolution and also a non-physical systematic influence on the q-profile measurement because the polarimetry diagnostic used for the real-time magnetic equilibrium reconstruction is based on Faraday rotation and requires a difficult deconvolution between the influences of the magnetic field and of the plasma density.

In the controller design, a specific account of the density variations can be taken by adding to the composite control law, $u(t) = u_s(t) + u_f(t)$, a feedforward component, u_{fwd}, which is computed in

real-time on the basis of the measured variations of the density vector with respect to the reference density vector and of the identified response to these variations. Any other parameter which could have a systematic influence on the system dynamics could be treated in the same way if the plasma response to its variations can be identified in the model. We shall therefore denote the disturbance vector by the general symbol d(t), with the understanding that d(t) includes at least the components of n(t). The variables d(t) and n(t) refer again to variations with respect to a reference state, d(t) = D(t) - D_{ref} and n(t) = N(t) - N_{ref}, and d(t) equals n(t) when the models have the ideal structure derived in section 2.

In order to isolate the response to the identified disturbances, d(t), from the response to the actuators, u(t), we write the reduced state space models in the form

$$\partial\tilde{\mu} / \partial t = A_s \tilde{\mu} + B_s \tilde{u}_s + E_s d_s \tag{61a}$$

$$\tilde{\rho}_s = C_s \tilde{\mu} + D_s \tilde{u}_s + F_s d_s \tag{61b}$$

and

$$\partial\rho_f / \partial\tau = A_f \rho_f + B_f u_f + E_f d_f \tag{61c}$$

so that the static gain matrix of the system assumes the form [K K_d] with

$$K = \begin{bmatrix} -A_s^{-1} \cdot B_s \\ D_s - C_s \cdot A_s^{-1} \cdot B_s \end{bmatrix} \quad \text{and} \quad K_d = \begin{bmatrix} -A_s^{-1} \cdot E_s \\ F_s - C_s \cdot A_s^{-1} \cdot E_s \end{bmatrix} \tag{62}$$

We have used here the reduced state and input variables as defined before, and since the final value of the disturbance vector cannot be known, we have assumed d_∞= 0. The disturbance vector can be split into its slow and fast components ($d=d_s+d_f$) by applying an appropriate filter to the raw measurements, D(t), and a *composite feedforward compensation*,

$$u_{fwd}(t) = u_{s,\,fwd}(t) + u_{f,\,fwd}(t) \tag{63}$$

can be applied to correct for the effect of disturbances. Ideally, it should be such that

$$\begin{bmatrix} B_s \\ D_s \end{bmatrix} \cdot u_{s,\,fwd} + \begin{bmatrix} E_s \\ F_s \end{bmatrix} \cdot d_s = 0 \tag{64a}$$

and

$$B_f \cdot u_{f,\,fwd} + E_f \cdot d_f = 0\,. \tag{64b}$$

Since there is no exact solution to Eq. (64a-64b), one can use here pseudo-inversions corresponding to the classical least-square minimization, i.e. without any particular scaling matrix such as Δ in Eq.

(28), but truncated to the most significant singular values, as in Eq.†(30). Denoting such truncated pseudo-inverses by the subscript “inv”, we then add the following contributions to the control laws of section 3.1 :

$$u_{s,\,fwd}(t) = -G_{s,\,fwd}\cdot d_s = -\begin{bmatrix} B_s \\ D_s \end{bmatrix}_{inv} \cdot \begin{bmatrix} E_s \\ F_s \end{bmatrix} \cdot d_s \tag{65a}$$

$$u_{f,\,fwd}(t) = -G_{f,\,fwd}\cdot d_s = -\,B_{f,\,inv}\cdot E_f \cdot d_f \tag{65b}$$

It is essential to note that such a feedforward disturbance rejection scheme does not alter the closed-loop stability of the feedback controls.

3.3. Actuator Saturation and Integral Windup

The PC controller design presented in sections 3.1-3.2 allows for some tuning parameters such as the R-matrix and the number of terms in various SVD truncations, which can be selected with care in order to limit the demand on the actuators. Such limitations have a negative impact on controller performance but they are essential because the available H&CD actuators are not as efficient as one would wish and have a large cost, so they offer marginal headroom for plasma control. Most of the time they can drive current unidirectionally, while the controller request can be both positive or negative. As a result, despite all the possible care in choosing the tuning parameters, actuator saturation is almost unavoidable, in particular in the early phase of the controller action.

During the time when one or several actuators are saturated, the feedback loops are inoperative and the error signals between the current plasma state and the target state may not decrease. In the integral term of the slow control law (Eq. 53), the winding up of the errors leads to an increasing demand on the actuators. It may eventually decrease if the “free” evolution of the system allows but it would take a long time before the control becomes active again. An anti-windup scheme is therefore necessary to avoid the accumulation of the error term and force a faster reset of the integral.

Due to actuator saturation, the delivered input vector, $U_{del}(t)$ may be different from the one, $U_{req}(t)$, which would be requested by application of the control law, including all feedforward and feedback contributions from the various loops. In such a case, to reset the winding up terms in Eq.†(53), an integral feedback on the “actuator error” is added to the controls so that this error eventually vanishes. Therefore, any controller request which otherwise would exceed a saturation limit remains at the saturation limit, and control is active again as soon as this request decreases.

The control law then includes the following anti-windup component :

$$U_{reset}(t) = -\frac{1}{\tau_{reset}} \int_0^t \left[U_{req}(t) - U_{del}(t) \right] dt \tag{66}$$

This additional loop is obviously inactive when none of the actuators are saturated since U_{reset} is then constant.

When adding up the reference value of the actuators, U_{ref} (which corresponds to the reference state around which the system has been linearized), the offset, u_∞, used in the definition of reduced variables, the contributions of the slow and fast feedback loops, the feedforward disturbance rejection, and the anti-windup component, the final control law then reads :

$$U(t) = U_{ref} + u_\infty + U_s(t) + u_f(t) + u_{fwd}(t) + U_{reset}(t) \qquad (67)$$

and the various terms are defined in Eq. (31), (53), (59), (63), (65) and (66).

3.4. Closed-Loop Simulations and Results

As an illustration of the possible controller performance and time response, we display here typical results of closed-loop simulations. They were performed with the SIMULINK® software, in the aim of testing the validity of the controller design and of the implemented computer programs. These simulations are based on the models described in section 2.4.2, which have been identified from JET experimental data (see Fig.6-9). The plasma response was assumed to be *linear* and governed by a full-order state space model which, in the limit $\varepsilon \to 0$, reproduces the identified two-time-scale reduced-order models consistently with Eq. (6a-6f). Note that, given the identified A_s, B_s, C_s, D_s and A_f, B_f matrices there is of course an infinite arbitrariness in the choice of a full-order model ($A_{i,j}$ matrices).

Both the slow and the fast reduced-order models were models of order 3. The magnetic and kinetic state variables, [x, z], were three Galerkin coefficients of the $\Psi(x)$ and T(x) profiles, corresponding exactly to the values of $\Psi(x)$ and T(x) at x = 0.4, 0.5 and 0.6, and the controlled output variables were $\mu = [\iota(0.4), \iota(0.5), \iota(0.6)]$ and $\rho = [\rho_{Te}^*(0.4), \rho_{Te}^*(0.5), \rho_{Te}^*(0.6)]$, six Galerkin coefficients corresponding exactly to the values of $\iota(x)$ and $\rho_{Te}^*(x)$ at the same radii. These data were obtained from the real-time magnetic reconstruction [31] and from an Electron Cyclotron Emission (ECE) radiometer. The three actuators are the powers delivered by the H&CD systems (P_{LH}, P_{NBI}, P_{ICRH}). The line-integrated densities along two vertical lines of sight of the interferometer (at major radii, R = 2.70 m and R = 3.04 m compared with a typical plasma axis location at R = 3.08m) constitute additional inputs that are considered as disturbances. The model identification was done in the plasma current control mode so the primary flux is not an available actuator for the PC controller in this simulation.

The reference state around which the system was linearized (JET Pulse No: 66041) corresponds to a toroidal field, B_T = 3T at the center of the plasma chamber (R = 2.96m), a plasma current, I_p = 1.5 MA, and a volume-averaged electron density, $n_e = 2.7 \times 10^{19}\ m^{-3}$. It was obtained by the usual advanced scenario preforming of the plasma on JET [1], with a low density LH preheat phase during current ramp-up, and then injecting H&CD powers at the reference values, P_{LH} = 1.7 MW,

P_{NBI} = 12MW, P_{ICRH} = 2MW (Fig. 6), during the plasma current flat-top phase. The target values for q and ρ_{Te}^{*} were chosen as q(0.4) = 2.47, q(0.5) = 2.76, q(0.6) = 3.14, and $\rho_{Te}^{*}(0.4) = 1.3 \times 10^{-2}$, $\rho_{Te}^{*}(0.5) = 0.9 \times 10^{-2}$, $\rho_{Te}^{*}(0.6) = 0.7 \times 10^{-2}$.

The static gain matrix, K, of the model yielded singular values, $\sigma = [1.06, 1.7 \times 10^{-2}, 3 \times 10^{-3}]$ and was truncated to retain only 2 principal modes ($n_{SV} = 2$) in Eq. (30). The tuning parameters of the controller were chosen as $\alpha_{\zeta} = 1$, $R = 10^{-2} \times Id_3$ (see Eq. 22), $\lambda_{ITB} = 10^3$ (see Eq. 24), and the following gain matrices were obtained, in MW :

$$G_{sp} = \begin{bmatrix} 58 & -92 & 69 & 0 & 0 & 0 \\ -0.07 & -15 & 4.6 & 0 & 0 & 0 \\ -19 & 77 & -26 & 0 & 0 & 0 \end{bmatrix}, \; G_{si} = \begin{bmatrix} 2.3 & 2.9 & 0.35 & 10 & -36 & 69 \\ -0.67 & -0.96 & -0.19 & -10 & 19 & -16 \\ -0.91 & 0.05 & 0.78 & 76 & -79 & -67 \end{bmatrix}, \; G_{f} = \begin{bmatrix} -3.8 & 9.9 & 7.8 \\ 0.17 & -1.6 & 3.1 \\ -8.8 & 2.3 & 7.6 \end{bmatrix} \tag{68}$$

Figure 20 shows the rapid initial variation of the kinetic variables due to the evolution of the fast components, ρ_f, which are finite at the start and during the first phase of the control period. After a characteristic time of about 0.3s., the fast components have relaxed ($\rho_f \approx 0$) and the kinetic variables follow their slow trajectories. During this second phase, both magnetic and kinetic variables are linked together by a quasi-equilibrium, and evolve slowly towards the requested targets. The target state, which is represented by the horizontal lines and is almost a coherent state of the system, is reached in approximately 4-5s. Saturation occurs at the start of control since two actuators (LH and ICRH) are requesting negative powers and are therefore clamped on their lower saturation limit (here zero) for almost 3s (Fig. 21).

Figutre 22 shows the evolution of the cost functional, I_{∞}, defined in Eq. (24) with $x_1 = x_3 = 0.4$ and $x_2 = x_4 = 0.6$. Fig.20 and 22 show that the excursion of the controlled parameters at the onset of the density perturbation is indeed reduced when the feedforward disturbance rejection scheme is added to the feedback control.

The effect of a feedforward compensation of known disturbances such as density perturbations is also shown. A sudden 25% density decrease has been applied on the simulation at t = 5s. The perturbation is decomposed into slow and fast components through a low-pass filter with a cutoff at 2.5Hz, the same as was used for the fast model identification. Without any feedforward compensation, the variations of the H&CD powers are continuous and smooth at the onset of the perturbation, while the response of the controller to the disturbance is discontinuous in the other case (Fig.21). The effect on the controlled variables is then faster, as shown on Fig. (20). The near-singular character of the model appears in the multi-valuedness of the LH and ICRH powers to provide at t ≈ 10s almost identical values of $\iota(x)$ and $\rho_{Te*}(x)$ at the controlled radii. Only 2 singular components were retained in the pseudo-inversion of Eq. (65a) for which the singular values were $[1.4 \times 10^{-1}, 1.8 \times 10^{-2}, 9 \times 10^{-4}]$, and only one in the pseudo-inversion of Eq.(65b) for which the singular values were $[4.5 \times 10^{-1}, 4.4 \times 10^{-3}, 2 \times 10^{-4}]$. The following gain matrices were then obtained in units of $10^{-19} \times MW.m^2$:

$$G_{s,\,fwd} = \begin{bmatrix} 2.9 & -1.8 \\ -0.47 & 0.61 \\ -1.2 & -3.5 \end{bmatrix}, \qquad G_{f,\,fwd} = \begin{bmatrix} 1.9 & -2.9 \\ -0.26 & 0.4 \\ 1.7 & -2.6 \end{bmatrix} \tag{69}$$

4. FIRST CLOSED-LOOP EXPERIMENTS AND RESULTS

The first attempts of using the Profile Controller (PC) for current profile control in real JET discharges started during the late 2006 and early 2007 experimental campaigns [28], after the open-loop experiments had been completed satisfactorily, and the subsequent model identification work (section 2.5) was sufficiently advanced for testing the slow loop of the controller (magnetic control). The PC actuators were different combinations of the LH, ICRH, NBI powers and surface loop voltage. The latter is controlled by the PF system through the boundary flux, and together with the plasma shape (XSC in the boundary flux control mode [30]). All these experiments were therefore performed in an operation mode in which the plasma current is not precisely controlled by the PF system. Instead, contrary to the usual JET operation, it was left floating within an allowed range (± 0.5MA around the reference current), only subject to current profile control through the PC. Now, with the XSC in the boundary flux control mode, two different configurations are still possible. When the actual loop voltage is not constrained to any particular value, the PF system can be used as a PC actuator, in addition to some H&CD systems. This is the case, for instance, during the current ramp-up phase and the transient evolution of the discharge towards a desired advanced plasma equilibrium. In the other configuration, the PF system is used as a separate actuator for tracking a given boundary flux waveform. This would be necessary for pure non-inductive operation (constant flux), once the desired equilibrium has been nearly reached and the inductive fraction of the current is low enough. The PC then uses only the H&CD actuators.

Within the available time for these initial investigations, some preliminary experiments were necessary to optimise the simultaneous control of the plasma shape and boundary flux, and to test the integration of the PC voltage request into a boundary flux request for the XSC. Then, we concentrated on four main experiments : *i)* the regulation of the plasma current through the PC during a steady heating phase (using the loop voltage as only actuator and the edge safety factor, q_{edge}, as the controlled variable), *ii)* the early use of the PC for current ramp-up (q_{edge} control after the formation of the plasma separatrix), in the aim of integrating later the control of the q-profile into the ramp-up phase to reduce current profile peaking, *iii)* the simultaneous control of several q-profile coefficients with the H&CD actuators, first at a given loop voltage, and then, *iv)* with the surface loop voltage as an additional actuator.

These experiments were performed in a high triangularity advanced scenario after a low density LH preheat during current ramp-up. The state space plasma model was described in section 2.5. The reference state around which the system was linearized (JET Pulse No: 67872) corresponds to a toroidal field, $B_T = 3$T on the magnetic axis, a plasma current, $I_p = 1.5$MA, and a volume-averaged electron density, $n_e = 3.5 \times 10^{19}$ m^{-3}. The reference H&CD powers were $P_{LH} = 2$MW, $P_{NBI} =$

13MW, P_{ICRH} = 3MW, and the reference loop voltage was 25mV/rad. The reference q-profile obtained with these discharge parameters is given in Table 2.

4.1. Regulation of the plasma current through q_{edge} control

The loop voltage at the surface of the plasma appears as an input variable in the state space model governing the dynamics of the magnetic and kinetic states of the plasma. This is inherent to the structure of the plasma transport equations (section 2.1), and therefore V_{ext} is to be considered on the same footing as the powers delivered by the H&CD systems. However, in conventional operation of tokamaks, the plasma current is accurately controlled and the surface loop voltage is not a free parameter. The JET XSC was recently upgraded in order to provide the possibility of controlling the plasma boundary flux rather than the plasma current [30] and the time-varying voltage request from the PC was then transformed into a request on the boundary flux waveform by simple integration, with an added offset in order to match the measured value of the boundary poloidal flux at the start of the control phase.

The first closed-loop experiments were dedicated to the integration of the PC and of the plasma shape and boundary flux control so as to evaluate the potentiality of using the PF system as a PC actuator, and identify limitations and possible improvements. The simplest test was to attempt a Single-Input Single-Output (SISO) control of the edge safety factor, q_{edge}, using the surface loop voltage as the only actuator. This test was necessary to assess the stability of the discharge under such an indirect control of the plasma current and was preliminary to any further use of the boundary flux request for Multiple-Input Multiple-Output (MIMO) profile control applications.

The result is shown on Fig.23 where the time evolution of q_{edge} is plotted for two similar discharges. The target value for q_{edge} was 4.8 for both pulses and it was effectively reached with good reproducibility. The PC was active from time t = 4.5s. for a duration of 6.5s. while the H&CD powers were constant and nearly equal to their reference values (P_{LH} = 2MW, P_{NBI} = 11.7MW, P_{ICRH} = 3.1MW). The tuning parameters of the controller were chosen as $\alpha_\zeta = 0.5$ and R = 0.25 (see Eq.22). For this limiting case with only one controlled variable, the integral in Eq. (24) is irrelevant and the Q matrix in Eq. (22) and (45) reduces to a scalar. To avoid singularities, the Δ matrix (Eq. 25-27) was computed using $\lambda_{ITB} = 0$, $x_1 = 0.975$, and $x_2 = 1$ in Eq. (24), and was truncated to retain only the scalar element corresponding to q_{edge}. The proportional and integral gains were obtained as G_{sp} = 3.49 Volts and G_{si} = -1.57 $V.s^{-1}$, respectively.

The request on the loop voltage, as calculated by the PC, is shown on Fig.24. It stabilizes around 0.2 Volts, i.e. 32mV/rad while the reference value corresponding to $q_{edge,ref}$ = 5.4 (Table 2) was 25 mV/rad with slightly different H&CD powers and plasma density. As discussed already in section 2.5.1 (Fig.10a), the response of the PF system to the boundary flux request is slow and there is always a few seconds delay before the XSC tracks a given flux waveform. Here the proper request should be on the loop voltage, i.e. on the rate of change of the flux, even with a large steady state offset on the requested flux waveform. But, for practical reasons, the loop voltage request is integrated

and transformed into a flux waveform that the XSC attempts to track without any offset. As a result, both the requested and the delivered loop voltages exhibit significant oscillations (Fig.24) before they converge to their static value, after a few seconds. When the XSC flux control is used on its own to apply a constant loop voltage at the plasma surface, for instance to force the plasma into a non-inductively driven state ($V_{ext} = 0$), this is of minor importance. On the contrary, this delay can be deleterious for using V_{ext} as a PC actuator. It can lead to a closed-loop instability, in particular when a larger set of actuators is used. For such applications where a proper control of the time derivative of the boundary flux is needed, the interface between the profile controller and the XSC would therefore require some improvements.

4.2. PLASMA CURRENT RAMP-UP THROUGH q_{EDGE} CONTROL

Tuning the early phases of the discharge is important to achieve enhanced plasma performance in the so-called advanced operation mode. This is true for plasma initiation, but also for the plasma current ramp-up phase because the magnetic shear at the time when strong heating is applied plays an essential role in the stabilization of plasma turbulence and in the emergence of ITBs. Current profile control is presently obtained by applying some pre-heating or LH current drive during the ramp-up phase to prevent current profile peaking. This is generally done in an feedforward, trial and error, fashion until an adequate timing of the strong NBI heating pulse triggers the desired improvement of the plasma performance. Some early control of the current profile is therefore needed during the ramp-up phase in order to increase the reproducibility of advanced operation scenarios. Such control could in principle be achieved through the present PC with a dedicated choice of the actuators and control parameters. The PF system is obviously a powerful actuator for this application. Some preliminary experiments were therefore performed in the simplest SISO configuration (similar to the one described in section 4.1), except for the early start of the control phase. The PC was switched on after the formation of the plasma separatrix so that the shape control by the XSC was already in a quasi-steady phase.

Figures 25a-b show the typical result of such a q-driven current ramp-up (Pulse No: 68905). The plasma current at the start of control (t = 2.7s) was 1.3 MA and the target value for q_{edge} was 4.8, corresponding roughly to a current of 1.8MA. The PC was active for a duration of 8.3s., and the LH power was constant ($P_{LH} = 2MW$), starting from t = 2.5s. while the NBI and ICRH powers were applied only at t = 3.5 s. and also constant ($P_{NBI} = 11.7MW$, $P_{ICRH} = 3.1MW$). After an initial drop due to the usual transient response of the boundary flux control (section 4.1), the current was ramped from 1.2MA to 1.8MA in 0.85s. Thus, with the chosen control parameters, the current ramp rate was around 700kA/s. This high ramp-up rate was achieved with good MHD stability, thus providing an adequate q-profile target for developing a high-performance advanced scenario with more intense plasma heating.

The optimal gains were computed from the same model as before. For this pulse, the controller parameters were $\alpha_\zeta = 0.6$, R = 0.4, $\lambda_{ITB} = 0$, $x_1 = 0.975$, $x_2 = 1$ and the Δ matrix was also truncated

to retain only the scalar element corresponding to q_{edge}. Then, the proportional and integral gains were $G_{sp} = -2.90$ Volts and $G_{si} = -1.26$ V.s^{-1}, respectively. The controller performed satisfactorily despite the fact that the plasma state at the start of control was far from the reference equilibrium state around which the model was identified.

These experiments need to be generalized using the MIMO configuration of the PC to possibly tailor the entire q-profile during the current ramp-up phase. To do so, we plan to use at least one additional actuator so that the current driven in the outer layers of the plasma and at half-radius can be properly balanced. LH current drive seems to be the most appropriate additional actuator thanks to a high current drive efficiency even at moderate plasma temperature and in the low beta phase of the discharge.

4.3. CONTROL OF THE q-PROFILE, USING THE H&CD ACTUATORS AT CONSTANT LOOP VOLTAGE

The third experimental tests were dedicated to the control of the q-profile during the current flat-top phase, using the H&CD systems as actuators and requesting a constant loop voltage from the PF system. This is a controller configuration to be used in the steady state phase of an advanced scenario, when the flux consumption from the primary circuit is bound to vanish (zero loop voltage). The controller parameters were based on the 3rd order model derived in section 2.5.4, so as a first test, only three coefficients of the q-profile were controlled. Since we use cubic splines as basis functions and the Galerkin residues (see appendix A1.2) are negligible, these coefficients correspond almost exactly to the values of q(x) at three different radii. In all these experiments, the real-time q-profile reconstruction depends mostly on the reconstruction of $\Psi(x)$ (see section 2.5.2) and is basically limited to a 3-parameter family of profiles [31]. Therefore a generalization to the control of the full set of 10 coefficients would be practically equivalent and should be straightforward. This can be checked in future experimental campaigns.

The result of the experiment is shown on Fig.26a-b. The controlled variables were q(x) at x = 0.2, 0.5 and 0.8 and their variations are plotted versus time. The corresponding target values were 1.85, 2.7 and 4.2, respectively. The controller was active between t = 4s. and t =11.5s., and the requested value of the surface loop voltage was 32 mV/rad during the control phase. As before, the initial behaviour of the controller is dominated by a transient in the boundary flux control which causes large oscillations of the loop voltage and, as a consequence, of the H&CD powers. Control becomes really effective and successful when the boundary flux has finally tracked the requested waveform, and the loop voltage has settled to the desired value.

The R-matrix in the quadratic J[U(t)] of Eq. (22) was chosen in relation to the available headroom for each actuator, namely

$$R = \begin{bmatrix} 0.20\ \mathrm{MW}^{-2} & 0 & 0 \\ 0 & 0.07\ \mathrm{MW}^{-2} & 0 \\ 0 & 0 & 0.16\ \mathrm{MW}^{-2} \end{bmatrix} \qquad (70)$$

with the actuators ordered as [P_{LH}, P_{NBI}, P_{ICRH}]. The other controller parameters in Eq.(22) and (24) were $\alpha_\xi = 25$, $\lambda_{ITB} = 0$, $x_1 = 0.2$, $x_2 = 0.8$ and the Π_μ matrix (Eq.26) was truncated to retain only the elements corresponding to the controlled variables. The static gain matrix, K, of the model yielded singular values, $\sigma = [4.7 \times 10^{-3}, 2.9 \times 10^{-3}, 7 \times 10^{-5}]$ and was approximated by retaining only two principal modes ($n_{SV} = 2$). The following gain matrices were then obtained:

$$G_{sp} = \begin{bmatrix} 14.4 & -26.3 & 100 \\ -50.3 & -230 & -577 \\ 24.5 & -33.3 & 179 \end{bmatrix} \text{MW} \qquad \text{and} \qquad G_{si'} = \begin{bmatrix} -14.7 & 6.13 & 10.4 \\ -49.1 & -112 & -36.7 \\ -22.6 & 15.3 & 19.2 \end{bmatrix} \text{MW.s}^{-1} \tag{71}$$

It is instructive to observe that, although there are three actuators to control three variables in this example, only two input modes (i. e. two combinations of the actuators) are effective. As a matter of fact, the requested target for the q-profile was not achievable exactly at $x = 0.8$. The *closest coherent achievable state* that the controller found has $q(x=0.8) \approx 4.5$ rather than 4.2. Fig. 26b shows the controller minimization of the cost functional, I_∞, defined in Eq. (24).

Finally, Fig. 27a-b show a comparison between the requested boundary flux and actuator powers, and the delivered ones. The controller outputs, i.e. the actuator requests, were limited within the following brackets : $0.5 \text{ MW} \le P_{LH} \le 3 \text{ MW}$, $1 \text{ MW} \le P_{NBI} \le 10 \text{ MW}$, $0 \le P_{ICRH} \le 4.2 \text{ MW}$, and the anti-windup reset time, τ_{reset} (Eq. 66), was set to 0.1s. Note that the LH power did not exceed 2 MW while the request approaches the 3 MW which were in principle available. This also limits the performance of the controller around $x = 0.8$.

4.4. CONTROL OF THE q-PROFILE USING THE BOUNDARY FLUX AS AN ADDITIONAL ACTUATOR

Finally, in the last experiment, q-profile control was attempted using four actuators, namely the H&CD powers and the loop voltage, to control five spline coefficients corresponding to $q(x)$ at $x =$ 0.2, 0.4, 0.6, 0.8 and 1. The corresponding target values were 1.8, 2.3, 3.2, 4.5, and 6.6, respectively. The R-matrix was again chosen in relation to the available headroom on the four actuators, namely

$$R = \begin{bmatrix} 25 \text{ MW}^{-2} & 0 & 0 & 0 \\ 0 & 0.016 \text{ MW}^{-2} & 0 & 0 \\ 0 & 0 & 0.057 \text{ MW}^{-2} & 0 \\ 0 & 0 & 0 & 44.4 \text{ V}^{-2} \end{bmatrix} \tag{72}$$

with the actuators ordered as [P_{LH}, P_{NBI}, P_{ICRH}, V_{ext}]. A very large relative weight was purposely chosen on the diagonal element corresponding to P_{LH} because, for these experiments, the LH generators were limited and there was no headroom above the reference power. The other controller

parameters were $\alpha_\zeta = 25$, $\lambda_{ITB} = 0$, as before, $x_1 = 0.2$, $x_2 = 1$, and the Π_μ matrix was also adequately truncated to retain only the elements corresponding to the controlled variables. The static gain matrix, K, of the model yielded singular values, $\sigma = [6.0 \times 10^{-2}, 4.2 \times 10^{-3}, 1.2 \times 10^{-4}, 1.6 \times 10^{-7}]$. It was again approximated by retaining only two principal modes. The following gain matrices were then obtained, with the first three rows of G_{sp} (G_{si}) in MW (MW/s) and the last row in Volts (V/s) :

$$G_{sp} = \begin{bmatrix} -0.0002 & -0.011 & -0.18 & 0.015 & 0.003 \\ 0.34 & -18.6 & -162 & -5.50 & -18.0 \\ -0.15 & -3.3 & -66.8 & 7.4 & 3.1 \\ 0.05 & -1.0 & -2.9 & -1.7 & -2.0 \end{bmatrix}, \qquad G_{si} = \begin{bmatrix} -0.031 & -0.026 & 0.003 & 0.018 & 0.002 \\ -22.4 & -24.7 & -4.5 & 6.2 & 1.30 \\ -12.4 & -9.6 & 2.0 & 8.3 & 0.90 \\ 0.10 & -0.53 & -0.69 & -0.79 & -0.03 \end{bmatrix} \quad (73)$$

As expected the gains corresponding to the LH actuator (first rows) are small, so the LH power request remains close to the reference power which was 2MW.

The result is shown on Fig.28a-b and the comparison between the requested values of the actuators, and the delivered ones is shown on Fig. 29a-b. The control phase starts at t = 4s. The controller outputs were limited within the following brackets : 0.5 MW ≤ P_{LH} ≤ 2MW, 1MW ≤ P_{NBI} ≤ 10 MW, 0 ≤ P_{ICRH} ≤ 4.2MW, 0.12 V ≤ V_{ext} ≤ 0.5 V, and the anti-windup reset time, τ_{reset} , was set to 0.1s. Note that the LH actuator is indeed practically inactive.

In this experiment, limitations were encountered during the transient oscillations of the boundary flux. Here, a soft discharge termination was triggered at t = 5.7s. so that a steady state could not be reached. Nevertheless, the trend on the evolution of the q-profile (Fig.28a) and of I_∞ (Fig.28b) was satisfactory and quite comparable to the initial evolution of the q-profile and of I_∞ shown on Fig. 26.

A discharge termination procedure was automatically triggered, as a protection measure, when the current in the tokamak central solenoid (P1 coil) departed excessively from a requested current waveform. In the present implementation of the PC, although the controller request refers to the loop voltage (i.e. to the rate of change of the boundary flux), the PF system is tracking a boundary flux target waveform (Fig.29a), until there is no offset. This entails large errors on the loop voltage and is too much of a constraint. In addition, the JET PF system design does not allow the voltage applied on the P1 solenoid to be reversed. Thus, during the flux oscillation, there are periodic phases when the P1 current departs from the requested waveform because the applied voltage is limited to zero. When the flux error is too large or the duration of such phases is too long, a discharge termination occurs. This is what happened here during the early phase of the control.

Therefore, although some profile control applications would in principle benefit from the use of the loop voltage as an additional actuator because it provides an efficient ohmic current drive in addition to the H&CD systems, the integration of the PC request into the PF system is a difficult task. The present implementation has shown some limitations and needs to be improved, possibly by controlling the rate of change of the boundary flux. Of course, ideally, the PF system, plasma dynamics and the transport physics should be fully integrated into a comprehensive tokamak model

with H&CD powers and coil voltages forming a complete set of inputs. But, despite extensive work aiming to obtain reliable first-principle modelling of plasma transport, this perspective seems quite remote. On the contrary, the control of the boundary magnetic parameters and plasma shape by the PF system can be accurately modelled from first principles. Therefore, restricting the experimental model identification to the volume enclosed within the separatrix (with V_{ext} as an independent input provided by the PF system, Eq. 2a-b) looks like an interesting compromise to design a controller for plasma parameter profiles. In any case, power amplifiers that allow the voltage applied on the central solenoid to be reversed would also be highly beneficial.

CONCLUSION

In this work, a two-time-scale dynamic-model approach is proposed in order to possibly regulate the performance of advanced tokamak plasmas through magnetic and kinetic profile control. It was specifically applied to the design of a Profile Controller (PC) for JET, but the design is sufficiently general to be easily adapted to other tokamaks.

A system identification procedure has been developed and applied to JET experimental data. The relevant magnetic and kinetic variables are radially distributed plasma parameters. However, retaining the full partial differential equation nature of the system for the model identification was not considered meaningful because the model parameters must be identified from noisy and inaccurate experimental data. A system discretization was therefore performed through an expansion onto a finite set of appropriate basis functions and a Galerkin scheme. From the coupled structure of plasma transport equations, and without any quantitative assumptions on the transport coefficients, a state space model can be derived in which some physical variables appear naturally as the state and input variables. These are the expansion coefficients of the internal magnetic poloidal flux and of the plasma density and temperature for the state variables, and the H&CD powers and surface loop voltage for the input variables. In the present work, for the sake of simplicity, the plasma density profile was not yet included in the kinetic variables to be controlled. In this case, it should however be characterized by some measured parameters that must appear in the state space model as independent inputs.

The model identification technique uses singular perturbation methods in order to cope with the high dimensionality of the system and with the small ratio, ε, between the confinement and resistive diffusion time scales (two-time-scale approximation). It was shown to yield reduced-order models which could fairly reproduce the slow and the fast evolution of a few profile coefficients, in some broad vicinity of a reference equilibrium plasma state. Examples were shown using either computer-simulated data produced by large non-linear transport codes, or experimental data. The same state space model structure and technique could be extended to describe the evolution of some non-dimensional output variables whose direct control would be physically very relevant, such as the (inverse) safety factor and the gyro-normalized temperature gradient profiles. Interestingly, with some justified assumptions, these output magnetic and kinetic variables can be linearly related to

the poloidal flux and temperature profiles, respectively. Then, by projecting the data onto a subspace of reduced dimension spun by the principal components of the system static gain matrix, the global evolution of the safety factor profile (10 coefficients) could be satisfactorily reproduced with a state space model whose maximum order (typically 3) is consistent with experimental data accuracy.

A controller based on the same two-time-scale approximation has been designed and implemented on JET.

It uses an $O(\varepsilon^2)$ near-optimal control algorithm which amounts to conventional optimal control when the ratio of the two time scales asymptotically vanishes. The maximum number of actuators was presently limited to four, namely three H&CD systems (LH, NBI, ICRH) and the surface loop voltage. Any partial combination of these four actuators can be used to control a chosen number of coefficients related either to the magnetic profiles only (e.g. the safety factor profile) through a slow feedback loop, or to the magnetic and kinetic profiles through a composite control law combining a slow (proportional+integral) and a fast (proportional) feedback loop. With given actuators, the set of achievable steady state plasma equilibria is hardly known in every detail in advance. When the number of controlled variables is larger than the number of actuators, the requested target state may not be a coherent equilibrium state, but the controller is designed to achieve the *closest coherent achievable state*, as defined by the minimization of a quadratic integral error.

In the absence of a proper regulation of the plasma density profile, its variations with respect to a reference profile can be considered as disturbances and measured in real-time. A composite feedforward disturbance rejection scheme that does not alter its closed-loop stability has therefore been added to the controller. The identified responses of the controlled profiles to either slow or fast variations of some chosen line-integrated interferometer signals can then be partially compensated for with anticipation on the feedback action. Finally, due to rather limited headroom on the H&CD systems, a conventional anti-integral-windup scheme has also been implemented to cope with the transient saturation of some actuators.

In order to validate the profile controller design and the associated software, closed-loop simulations were performed, based on a linear plasma response model which is consistent with the identified reduced-order models in the vicinity of a given reference state. They show that, with an appropriate selection of some tuning parameters, magnetic and kinetic profiles can be regulated within a few seconds (typically 3-4 seconds).

Now, an extensive set of closed-loop experiments are required on real JET plasmas to assess whether the linear response models are robust and accurate enough for the radial profiles of the safety factor, $q(x)$, and gyro-normalized electron temperature gradient, $\rho_{Te}^*(x)$, to be simultaneously regulated or controlled in real-time. These experiments are to be conducted stage by stage, starting from simple PC configurations for magnetic control only, before proceeding to the integrated magnetic and kinetic control in moderate performance plasmas and ultimately attempting to regulate high-performance advanced tokamak plasmas.

First closed-loop experiments were performed on JET during the last experimental campaigns.

They were dedicated to the control of the safety factor profile in order to test some basic features of the proposed approach. In particular, the integration of the loop voltage request into the JET eXtreme Shape Controller (XSC) was achieved by running the XSC in the boundary flux control mode. This mode of operation of the PF system is particularly suitable for advanced scenarios which are meant to be ultimately operated in steady state, i.e. at constant boundary flux rather than at a precisely given plasma current. The plasma current, which is then kept floating within some predefined bounds, is to be regulated as a result of current profile control. Hence, in this operational mode, the safety factor in the plasma edge region must be embeded in the controlled variables.

Four different controls were attempted. First the regulation of the plasma current through the control of the edge safety factor, q_{edge}, was tested during a constant heating phase, using the boundary flux as the only actuator. Then, with the same controller configuration and to prefigure the tailoring of the q-profile during current ramp-up, q_{edge} control was initiated just after the separatrix formation in order to possibly achieve current ramp-up through the PC. Both experiments were successful in controlling the plasma shape and safety factor simultaneously, and achieving the requested ramp-up in a stable manner in the second case. Nevertheless they pointed to a limitation (large oscillations) in the use of boundary flux control to provide the requested surface loop voltage. The third experiment achieved successful q-profile control using the three H&CD systems as actuators to control three profile coefficients, and requesting a constant loop voltage from the PF system. Finally, the last experiment attempted to use the boundary flux as an additional actuator to control five coefficients of the q-profile. In this configuration, the oscillations which characterise the boundary flux control led to severe limitations. This will require some improvements, possibly by controlling the rate of change of the boundary flux and tracking more accurately the requested loop voltage.

Altogether, an important step has been made towards the development of an integrated magnetic and kinetic control methodology. Forthcoming JET experiments should address *i)* the control of the safety factor over the entire plasma radius (10 profile coefficients) with three H&CD actuators and at constant boundary flux, and *ii)* the simultaneous control of the current and electron temperature profiles in advanced operation scenarios. This should ideally be done in a staged approach, first at moderate plasma performance in order to experimentally assess the proposed two-time-scale approach, and then in high β_N plasmas possibly with large bootstrap current fractions. The regulation of ITBs through the control of the q-profile and of the gyro-normalized temperature gradient is also an ultimate goal to be pursued. As far as magnetic sensors are concerned, these experiments would benefit from a real-time Grad-Shafranov magnetic reconstruction. In parallel, some improvements are also needed for a practical use of the ohmic drive (PF system) as an additional actuator on JET, in particular for q-profile control during current ramp-up or for composite magnetic/kinetic control where the number of controlled variables is larger.

Then, using the H&CD systems together with the PF system for controlling *(i)* the plasma shape, *(ii)* the magnetic and kinetic plasma profiles, and *(iii)* the boundary flux, could provide the essential part of an integrated scheme for achieving high-performance non-inductively driven advanced

tokamak discharges in JET. The technique can be adapted to any device, for simple as well as more comprehensive controls, and with other actuators and sensors. Experiments on other pulsed (DIII-D, JT-60U) and steady-state tokamaks (Tore-Supra, EAST, and later KSTAR, JT-60SA) would also be beneficial to possibly validate or improve the proposed methodology. They could provide a broad basis for developing integrated profile control and steady state advanced scenarios in ITER.

ACKNOWLEDGMENTS

This work has been performed under the European Fusion Development Agreement (EFDA).

REFERENCES

[1]. Challis C.D. 2004 Plasma Phys. Contr. Fus. **46** B23.

[2]. Ide S. and the JT-60 Team 2005 Nucl. Fusion **45** S48.

[3]. Litaudon X. *et al* 2007 *"Development of Steady State Scenarios Compatible with ITER-like Wall Conditions"*, submitted to Plasma Phys. Contr. Fus.

[4]. Luce T. C. for the DIII-D Team 2005 Nucl. Fusion **45** S86.

[5]. Sips A., Hobirk J. and Peeters A.G. 2003 Fusion Science and Technology **44** 605.

[6]. Takase Y. *et al* 2006 *Proc. 21st Int. Conf. on Fusion Energy 2006 (Chengdu, China)*, (Vienna: IAEA), CD-ROM file (EX/1-4) and http://www-naweb.iaea.org/napc/physics/FEC/FEC2006/html/node16.htm#2345.

[7]. Gormezano C. *et al* 2007 Nucl. Fusion **47** S285 (ITER Physics Basis, Chapter 6).

[8]. Gribov Y. *et al* 2007 Nucl. Fusion **47** S385 (ITER Physics Basis, Chapter 8).

[9]. Walker M.L. *et al* 2006 IEEE Control Systems Magazine **26-2** 35.

[10]. Moreau D. *et al* 2006 *Proc. 21st Int. Conf. on Fusion Energy 2006 (Chengdu, China)*, (Vienna: IAEA), CD-ROM file (EX/P1-2) and http://www-naweb.iaea.org/napc/physics/FEC/FEC2006/html/node57.htm#14844.

[11]. Ferron J. *et al* 2006 Nucl. Fusion **46** L13.

[12]. Suzuki T. *et al* 2006 *Proc. 21st Int. Conf. on Fusion Energy 2006 (Chengdu, China)*, (Vienna: IAEA), CD-ROM file (EX/6-4) and http://www-naweb.iaea.org/napc/physics/FEC/FEC2006/html/node281.htm#55891.

[13]. Mazon D. *et al* 2006 *Proc. 33rd EPS Conf. on Plasma Physics 2006 (Roma, Italy)*, paper O3.018.

[14]. Sakamoto Y. *et al* 2006 *Proc. 21st Int. Conf. on Fusion Energy 2006 (Chengdu, China)*, (Vienna: IAEA), CD-ROM file (EX/P1-10) and http://www-naweb.iaea.org/napc/physics/FEC/FEC2006/html/node65.htm#16831.

[15]. Humphreys D.A. *et al* 2007 Nucl. Fusion **47** 943.

[16]. Moreau D. *et al* 2004 *Proc. 20th Int. Conf. on Fusion Energy 2004 (Vilamoura, Portugal)*, (Vienna: IAEA), CD-ROM file (EX/P2-5) and http://www-naweb.iaea.org/programmes/napc/physics/fec/fec2004/datasets/EX_P2-5.html.

[17]. Laborde L. *et al* 2005 Plasma Phys. Contr. Fus. **47** 155.
[18]. Mazon D. *et al* 2003 Plasma Phys. Contr. Fus. **45** L47.
[19]. Moreau D. *et al* 2003 Nucl. Fusion **43** (2003) 870.
[20]. Tresset G. *et al* 2002 Nucl. Fusion **42** 520.
[21]. Moreau D. *et al* 2006 *Proc. 33rd EPS Conf. on Plasma Physics 2006 (Roma, Italy)*, paper P1.069.
[22]. Basiuk V. *et al* 2003 Nucl. Fusion **43** (2003) 822.
[23]. Pereverzev G. and Yushmanov P.N. 2002 *"ASTRA Automated System for TRansport Analysis in a Tokamak"*, IPP-Report IPP 5/98, Max-Planck-Institut für Plasmaphysik.
[24]. Genacchi G. and Taroni A. 1988 *"JETTO : A free boundary plasma transport code (basic version)"*, Report ENEA RT/TIB 1988(5) ENEA.
[25]. Kokotovitch P.V., Khalil H.K. and O'Reilly J. 1986 *Singular Perturbation Methods in Control: Analysis and Design*, Academic Press, London.
[26]. Tala T. *et al* 2005 Nucl. Fusion **45** 1027.
[27]. Ljung L. 1999 *System Identification: Theory for the User*, Prenctice Hall PTR.
[28]. Mazon D. *et al* 2007 *Proc. Int. Workshop on Burning Plasma Diagnostics 2007 (Varenna, Italy)*.
[29]. Ambrosino G. *et al* 2003 Fusion Engineering and Design **66-68** 797.
[30]. Ariola M. *et al* 2007 "*Integrated Plasma Shape and Boundary Flux Control at JET*", EFDA-JET Report EFDA-JET-PR(07)10, Fusion Sci. Technology (accepted for publication).
[31]. Zabeo L. *et al* 2002 Plasma. Phys. Control. Fusion **44** 2483.
[32]. Ray W. H. 1981 *Advanced Process Control*, McGraw-Hill Inc., New York.

APPENDIX A1. A MINIMAL STATE SPACE MODEL FOR MAGNETIC AND KINETIC PROFILE CONTROL

A1.1 DISTRIBUTED-PARAMETER PLASMA MODEL

The generic structure of the tentative state space model postulated in section 2.1 can be derived by linearising the transport equations (Eq.1) in the cylindrical approximation where x is the radial independent variable, normalized such that $x = 1$ at the plasma edge, and other (toroidal and poloidal) space variables are assumed to be ignorable. This amounts to reducing the differential operators to derivatives with respect to x, and yields an approximate 1-D model of the plasma which is more tractable for real-time applications than the exact set of flux-surface-averaged transport equations in an arbitrary geometry. When trying to fit the models to experimental data, the dependent variables will however be generally considered as flux-surface averages of the physical variables of interest. Consistently with these approximations, only the toroidal component of the current density and electric field, and only the radial component of the heat and particle fluxes will be retained. Other physical assumptions are given in points *i)* to *vi)* in section 2.1 and will be refered to with the same numbering below.

Linearization is performed around an equilibrium reference state labeled by the subscript “ref” and the following variables are defined :

$$j(x, t) = J(x, t) - J_{ref}(x), \qquad E(x, t) = E(x, t) - E_{ref}(x) \tag{A1-1a}$$

$$n(x, t) = N(x, t)-N_{ref}(x),\ \Gamma_n(x, t) = G_n(x, t)-G_{n,ref}(x),\ S_n(x, t) = S_n(x, t)-S_{n,ref}(x) \tag{A1-1b}$$

$$T(x, t) = T(x, t)-T_{ref}(x),\ \Gamma_T(x, t) = G_T(x, t)-G_{T,ref}(x),\ S_T(x, t) = S_T(x, t)-S_{T,ref}(x) \tag{A1-1c}$$

Decomposing the current density into an ohmically driven current and a non-inductively driven current,

$$J(x, t) = \sigma(x, t)\, E(x, t) + J_{ni}(x, t) \tag{A1-2}$$

with

$$\sigma(x, t) = \sigma_{ref}(x) + \hat{\sigma}(x, t) \quad \text{and} \quad J_{ni}(x, t) = J_{ni,ref}(x) + j_{ni}(x, t), \tag{A1-3}$$

the linearized system of equations reads (a is the minor plasma radius):

$$\mu_0 \frac{\partial j(x,t)}{\partial t} = \frac{1}{a^2}\left[\frac{1}{x}\frac{\partial}{\partial x}\left(x\frac{\partial E(x,t)}{\partial x}\right)\right] \tag{A1-4a}$$

$$\frac{\partial n(x,t)}{\partial t} = -\frac{1}{ax}\frac{\partial}{\partial x}\left[x\Gamma_n(x,t)\right] + S_n(x,t) \tag{A1-4b}$$

$$\frac{3}{2}\left[N_{ref}(x)\frac{\partial T(x,t)}{\partial t} + T_{ref}(x)\frac{\partial n(x,t)}{\partial t}\right] = -\frac{1}{ax}\frac{\partial}{\partial x}\left[x\Gamma_T(x,t)\right] + S_T(x,t) \tag{A1-4c}$$

Combining Eq. (A1-4b) and (A1-4c), one obtains an equation for the evolution of the plasma temperature:

$$\frac{3}{2}N_{ref}(x)\frac{\partial T(x,t)}{\partial t} = \frac{3}{2}T_{ref}(x)\left[\frac{1}{ax}\frac{\partial}{\partial x}\left[x\Gamma_n(x,t)\right] + S_n(x,t)\right] - \frac{1}{ax}\frac{\partial}{\partial x}\left[x\Gamma_T(x,t)\right] + S_T(x,t) \tag{A1-5}$$

Whether to use Eq. (A1-4c) for the plasma pressure or Eq. (A1-5) for the temperature is a matter of choice and depends upon the chosen set of controlled variables. Here we have selected the temperature because of diagnostic space and time resolution, but a model for the evolution of the plasma density and pressure could be derived in the same way.

Now, at some point, Eq. (A1-4a) will need to be integrated over time to avoid manipulating time derivatives of $\hat{\sigma}(x, t)$, $j_{ni}(x, t)$ and therefore of the input parameters. Instead, to speed up the derivation, we can directly start from an integrated form of Eq. (A1-4a). It is obtained by introducing the magnetic vector potential, $A(x, t)$, into Ampere’s law which then reads :

$$\nabla\times\nabla\times A(x, t) = \mu_0 J(x, t). \qquad \text{(A1-6)}$$

Within our quasi-cylindrical approximation, as for $E(x, t)$, we shall retain only the toroidal component of the vector potential. The toroidal coordinate being an ignorable coordinate, it follows that

$$E(x, t) = -\partial A(x, t)/\partial t. \qquad \text{(A1-7)}$$

Let us also introduce the•*total* poloidal magnetic flux, $\hat{\psi}(x, t)$, the local plasma loop voltage, $V(x, t)$, and the *internal* poloidal magnetic flux, $\psi(x, t) = \hat{\psi}(x, t) - \hat{\psi}_B(t)$, where $\hat{\psi}_B(t) = \hat{\psi}(1, t)$ denotes the total poloidal flux at the plasma boundary. In the same cylindrical approximation, R_0 denoting the average plasma major radius, one writes

$$\hat{\psi}(x, t) = 2\pi R_0 A(x, t) \quad \text{and} \quad V(x,t) = 2\pi R_0 E(x,t) = -\frac{\partial\hat{\psi}(x,t)}{\partial t} \qquad \text{(A1-8)}$$

and, with Eq. (A1-2), Ampere's law becomes

$$\frac{1}{a^2}\left[\frac{1}{x}\frac{\partial}{\partial x}\left(x\frac{\partial\hat{\psi}(x,t)}{\partial x}\right)\right] = \frac{1}{a^2}\left[\frac{1}{x}\frac{\partial}{\partial x}\left(x\frac{\partial\psi(x,t)}{\partial x}\right)\right] = -2\pi R_0\,\mu_0\left[\sigma(x,t)E(x,t) + J_{ni}(x,t)\right] \qquad \text{(A1-9)}$$

The loop voltage at the plasma boundary, $V_{ext}(t)$, is related to $\hat{\psi}_B(t)$ by

$$V_{ext}(t) = -\frac{\partial\hat{\psi}_B(t)}{\partial t} \qquad . \qquad \text{(A1-10)}$$

At equilibrium, the electric field, $E(x, t) = E_{ref}$, and the loop voltage, $V(x, t) = V_{ref} = V_{ext, ref}$ are steady and uniform across the plasma, with

$$V_{ref} = 2\pi R_0 E_{ref} = -\left[\frac{\partial\hat{\psi}(x,t)}{\partial t}\right]_{ref} \quad \text{and} \quad V_{ext,ref} = -\left[\frac{\partial\hat{\psi}_B(t)}{\partial t}\right]_{ref} \qquad \text{(A1-11)}$$

so that the internal flux reaches a steady state, $\psi(x, t) = \psi_{ref}(x)$.

Now, defining $V(x, t) = V(x, t) - V_{ref}$, $V_{ext}(t) = V_{ext}(t) - V_{ref}$, and $\Psi(x, t) = \psi(x, t) - \psi_{ref}(x)$, one can write

$$\frac{\partial\Psi(x,t)}{\partial t} = \frac{\partial\psi(x,t)}{\partial t} = \frac{\partial\hat{\psi}(x,t)}{\partial t} - \frac{\partial\hat{\psi}_B(t)}{\partial t} = V_{ext}(t) - V(x,t) = V_{ext}(t) - V(x,t) \qquad \text{(A1-12)}$$

The linearized version of Eq. (A1-9) reads

$$\frac{1}{a^2}\left[\frac{1}{x}\frac{\partial}{\partial x}\left(x\frac{\partial\Psi(x,t)}{\partial x}\right)\right] = -2\pi R_0\,\mu_0\left[\sigma_{ref}(x)E(x,t) + \hat{\sigma}(x,t)E_{ref} + j_{ni}(x,t)\right] \qquad \text{(A1-13)}$$

i.e.,

$$\frac{1}{\mu_0 a^2 \sigma_{ref}(x)}\left[\frac{1}{x}\frac{\partial}{\partial x}\left(x\frac{\partial \Psi(x,t)}{\partial x}\right)\right] = -\left[V(x,t) + \frac{\hat{\sigma}(x,t)}{\sigma_{ref}(x)} V_{ref} + \frac{2\pi R_0}{\sigma_{ref}(x)}\, j_{ni}(x,t)\right] \qquad \text{(A1-14)}$$

and using Eq.(A1-12) for V(x, t), the equation for the evolution of Ψ(x, t) is found :

$$\frac{\partial \Psi(x,t)}{\partial t} = \frac{1}{\mu_0 a^2 \sigma_{ref}(x)}\left[\frac{1}{x}\frac{\partial}{\partial x}\left(x\frac{\partial \Psi(x,t)}{\partial x}\right)\right] + \frac{V_{ref}}{\sigma_{ref}(x)}\hat{\sigma}(x,t) + \frac{2\pi R_0}{\sigma_{ref}(x)}\, j_{ni}(x,t) + V_{ext}(t) \qquad \text{(A1-15)}$$

Now, assumptions *ii)* to *vi)* of section 2.1, together with proper linearization of the assumed dependences of $\hat{\sigma}$, j_{ni}, Γ_n, Γ_T, S_n, S_T with respect to n(x, t), T(x, t) and j(x, t), enable the system (Eq. A1-4b, A1-5 and A1-15) to be cast in a form which envolves a small number of essential dynamical variables. Formally, one can define some linear differential operators, $L_{\alpha,\beta}\{x\}$, and line vectors, $L_{\alpha,\beta}(x) = [L^{(LH)}_{\alpha,\beta}(x)\ L^{(NBI)}_{\alpha,\beta}(x)\ L^{(ICRH)}_{\alpha,\beta}(x)]$, depending upon the variable x but independent of time, such that the system reads :

$$\frac{\partial \Psi(x,t)}{\partial t} = L_{\Psi,\Psi}\{x\}\cdot\Psi(x,t) + L_{\Psi,T}\{x\}\cdot T(x,t) + L_{\Psi,n}\{x\}\cdot n(x,t) + L_{\Psi,P}(x)\,P(t) + V_{ext}(t) \qquad \text{(A1-16a)}$$

$$\frac{\partial n(x,t)}{\partial t} = L_{n,\Psi}\{x\}\cdot\Psi(x,t) + L_{n,T}\{x\}\cdot T(x,t) + L_{n,n}\{x\}\cdot n(x,t) + L_{n,P}(x)\,P(t) \qquad \text{(A1-16b)}$$

$$\frac{\partial T(x,t)}{\partial t} = L_{T,\Psi}\{x\}\cdot\Psi(x,t) + L_{T,T}\{x\}\cdot T(x,t) + L_{T,n}\{x\}\cdot n(x,t) + L_{T,P}(x)\,P(t) \qquad \text{(A1-16c)}$$

where P(t) is a power input column vector consisting of three elements which are power variations with respect to some reference values :

$$P(t) = \begin{bmatrix} P_{LH}(t) \\ P_{NBI}(t) \\ P_{ICRH}(t) \end{bmatrix} = P(t) - P_{ref} = \begin{bmatrix} P_{LH}(t) - P_{LH,ref} \\ P_{NBI}(t) - P_{NBI,ref} \\ P_{ICRH}(t) - P_{ICRH,ref} \end{bmatrix} \qquad \text{(A1-17)}$$

Eq. (A1-16) represent the minimal distributed-parameter model one can possibly derive to describe in an approximate fashion the time evolution of the magnetic and kinetic state of the plasma. The internal poloidal flux, Ψ(x, t), appears as a natural magnetic state variable and the plasma temperature, T(x, t), and density, n(x, t), appear as natural kinetic state variables. Generalization to a two-fluid plasma would be straightforward with an an additional equation for an additional state variable, T_i(x, t), representing the ion temperature while T = T_e(x, t) represents the electron temperature. Natural input variables are the power vector, P(t) and the external loop voltage, V_{ext}(t).

A1.2 REDUCTION TO A LUMPED-PARAMETER MODEL THROUGH A GALERKIN SCHEME

A pragmatic way to identify the various operators in Eq. (A1-16) is to resort to a finite set of trial basis functions on which to project the distributed plasma parameters and to least-square fits of the

discrete system to experimental data. A Galerkin approach will be followed here, and it is assumed that by increasing the number of trial basis functions the solution of the identified discrete system converges towards the solution of the full differential system. Let the basis functions be $a_i(x)$ with i = 1, 2,... N (e.g. cubic splines as shown in Fig. 1a). The Galerkin projection of a generic dynamical variable, Y(*x*, t), reads :

$$Y(x,t) = \sum_{i=1}^{N} G_{y,i}(t)\, a_i(x) + R_{y,i}(x,t) \qquad \text{(A1-17)}$$

where the residues, $R_{y,i}(x, t)$, are chosen to be orthogonal to every basis function :

$$\int_0^1 a_i(x)\, R_{y,i}(x,t)\, dx = 0 \ , \qquad \text{(A1-18)}$$

and the expansion coefficients, $G_{y,i}(t)$, will be called the Galerkin coefficients of the variable y(*x*,†t). The vector whose elements are the Galerkin coefficients will be denoted as $G_y(t)$ or sometimes simply as Y(t) for convenience. The set of basis functions could indeed be different for each dynamical variable and must be chosen judiciously to provide a satisfactory fit of the corresponding parameter profiles. For instance, for the variable $\rho_{Te}^*(x)$, a different set, $b_i(x)$, was used (see section 2.3 and Fig.1-b).

Multiplying every equation in (A1-16) by the appropriate basis functions (here $a_j(x)$ with j = 1, 2,... N), integrating over *x* and neglecting integrals involving the residues of the expansions yields an ordinary differential system of equations of the form :

$$\Pi_\Psi \cdot \frac{dG_\Psi}{dt} = A_{\Psi\Psi} \cdot G_\Psi(t) + A_{\Psi T} \cdot G_T(t) + A_{\Psi n} \cdot G_n(t) + B_{\Psi P} \cdot P(t) + C_{\Psi V} . V_{ext}(t) \qquad \text{(A1-19a)}$$

$$\Pi_n \cdot \frac{dG_n}{dt} = A_{n\Psi} \cdot G_\Psi(t) + A_{nT} \cdot G_T(t) + A_{nn} \cdot G_n(t) + B_{nP} \cdot P(t) \qquad \text{(A1-19b)}$$

$$\Pi_T \cdot \frac{dG_T}{dt} = A_{T\Psi} \cdot G_\Psi(t) + A_{TT} \cdot G_T(t) + A_{Tn} \cdot G_n(t) + B_{TP} \cdot P(t) \qquad \text{(A1-19c)}$$

where Π_α and $A_{\alpha\beta}$ are matrices whose (i, j) elements are made of scalar products involving the appropriate basis functions :

$$\Pi_\alpha^{i,j} = \int_0^1 a_i(x)\, a_j(x)\, dx \qquad \text{(A1-20a)}$$

$$A_{\alpha\beta}^{i,j} = \int_0^1 a_i(x)\, L_{\alpha,\beta}\{x\} \cdot a_j(x)\, dx \ , \qquad \text{(A1-20b)}$$

$B_{\alpha\beta}$ is a 3-column matrix whose i^{th} line is given by

$$B^{i}_{\alpha\beta} = \int_0^1 a_i(x)\, L_{\alpha,\beta}(x)\, dx \qquad . \tag{A1-20c}$$

and $C_{\Psi V}$ is a column vector whose i^{th} element is given by

$$C^{i}_{\Psi V} = \int_0^1 a_i(x)\, dx \qquad . \tag{A1-20d}$$

In this paper, we do not consider the real-time control of the plasma density (see sections 2.1 and 3.2). We shall then restrict ourselves to Eq. (A1-19a) and (A1-19c) and consider the variations of the plasma density coefficients, $G_n(t)$, as known (measurable) perturbations, i.e. as additional inputs to the model. A lumped-parameter state space model is finally obtained by inverting the Π_α matrices and defining new matrices A_{hk} , B_{hk} (with h = 1, 2 and k = 1, 2) and $B_{\Psi V}$. It has the following structure :

$$\dot{\Psi}(t) = A_{11} \cdot \Psi(t) + A_{12} \cdot T(t) + B_{11} \cdot P(t) + B_{12} \cdot n(t) + B_{\Psi V}.V_{ext}(t) \tag{A1-21a}$$

$$\varepsilon\, \dot{T}(t) = A_{21} \cdot \Psi(t) + A_{22} \cdot T(t) + B_{21} \cdot P(t) + B_{22} \cdot n(t) \tag{A1-21b}$$

where $B_{\Psi V}$ is known :

$$B_{\Psi V} = \Pi_{\Psi}^{-1} \cdot C_{\Psi V} \qquad . \tag{A1-22}$$

Here dotted variables refer to their time derivatives (d/dt) and, for all the dynamic variables, the simple generic notation Y(t) has been used to refer to the column vector $G_y(t)$. A small scaling parameter, ε, has been introduced when defining A_{2k} and B_{2k} (k = 1, 2) to exhibit the large ratio between the kinetic time scale and the magnetic time scale.

APPENDIX A2. DATA PROCESSING FOR PRACTICAL MODEL IDENTIFICATION

The state space models to be identified from experimental data involve linearized equations,

$$\dot{X}(t) = A \cdot X(t) + B \cdot U(t) \tag{A2-1a}$$

$$Y(t) = C \cdot X(t) + D \cdot U(t), \tag{A2-1b}$$

dynamical state vectors, X(t), input vectors, U(t), and possibly output vectors, Y(t), that are defined as variations with respect to reference values, X_{ref}, U_{ref}, Y_{ref}:

$$X(t) = X(t) - X_{ref} \quad U(t) = U(t) - U_{ref} \qquad\qquad Y(t) = Y(t) - Y_{ref} \tag{A2-2}$$

In pulsed devices such as JET, and in the advanced mode of operation, the duration of plasma discharges does not exceed the resistive diffusion time scale by a sufficient margin to be able to reach a steady state equilibrium unambiguously. Therefore the reference state (which corresponds to the plasma equilibrium when the input variables are set to their reference values) is not known and the X(t), U(t) and Y(t) data cannot be obtained from the measured X(t), U(t) and Y(t) data.

To deal with this problem we define for each discharge used for model identification, a time window, $[t_1, t_2]$, in which the identification will be performed, and a set of new variables that can be calculated offline from the measured data, and with the same sampling time as the original data :

$$\hat{X}(t) = X(t) - \langle X \rangle = X(t) - \langle X \rangle \tag{A2-3a}$$

$$\hat{U}(t) = U(t) - \langle U \rangle = U(t) - \langle U \rangle \tag{A2-3b}$$

$$\hat{Y}(t) = Y(t) - \langle Y \rangle = Y(t) - \langle Y \rangle \quad . \tag{A2-3c}$$

Here, brackets denote signal averages between t_1 and t_2, such as

$$\langle X \rangle = \frac{1}{t_2 - t_1} \int_{t_1}^{t_2} X(t)\, dt \quad . \tag{A2-4}$$

Interestingly, with minor changes in the input vector, the state space model [A, B, C, D] to be identified also governs the evolution of the new variables :

$$\dot{\hat{X}}(t) = A \cdot \hat{X}(t) + B \cdot \hat{U}(t) + \Delta_t X \tag{A2-5a}$$

$$\hat{Y}(t) = C \cdot \hat{X}(t) + D \cdot \hat{U}(t) \tag{A2-5b}$$

where

$$\Delta_t X = \langle \dot{X} \rangle = \frac{X(t_2) - X(t_1)}{t_2 - t_1} = \frac{X(t_2) - X(t_1)}{t_2 - t_1} \tag{A2-6}$$

is an additional input vector which is known from the data and is to be included when identifying the system (A2-4a, A2-4b). Model identification can then proceed using the new variables and therefore the reference state needs not be known.

Nevertheless, once the system [A, B, C, D] producing the best fit to the experimental data has been identified, it is possible to extrapolate the data at the end of the reference pulse assuming that the input vector is kept constant, $U(t) = U_{ref}$, i. e. $\hat{U}(t) = U_{ref} - \langle U \rangle = -\langle U \rangle$. One can thus estimate the steady state values, $\hat{X}_\infty$ and $\hat{Y}_\infty$, that $\hat{X}(t)$ and $\hat{Y}(t)$ should have reached, respectively, if the reference inputs had been applied until the plasma is in equilibrium :

$$\hat{X}_\infty = -A^{-1}\cdot\left[B\cdot\left(U_{ref} - \langle U \rangle\right) + \Delta_t X\right] = A^{-1}\cdot\left[B\cdot\langle U\rangle - \Delta_t X\right] \qquad \text{(A2-7a)}$$

$$\hat{Y}_\infty = C\cdot\hat{X}_\infty + D\cdot\left(U_{ref} - \langle U \rangle\right) = C\cdot\hat{X}_\infty - D\cdot\langle U\rangle \quad . \qquad \text{(A2-7b)}$$

Through this extrapolation, one has access to an estimate of the reference state :

$$X_{ref} = \hat{X}_\infty + \langle X \rangle \qquad \text{(A2-8a)}$$

$$Y_{ref} = \hat{Y}_\infty + \langle Y \rangle \; . \qquad \text{(A2-8b)}$$

An approximate knowledge of the reference state can be useful because the controller design is based on the reduced variables, X(t) and Y(t) which can then be calculated in real-time from the measurements, X(t) and Y(t). This only introduces constant offsets on the variables to be controlled. In closed-loop operation, any error on these offsets will be rapidly compensated by the feedback control action. An accurate estimation of X_{ref} and Y_{ref} is therefore not essential.

APPENDIX A3. SYSTEM ORDER REDUCTION THROUGH THE QUASI-STATIC APPROXIMATION

With enough basis functions to describe the magnetic and kinetic profiles satisfactorily, the orders of the generic models derived in appendix A1 are large. This may have some drawbacks. If slow and fast models of such high orders (say n_x and n_z, respectively) are available, some of the high-order modes are likely to be uncontrollable (see section 3.1.2). Also, if only a subset, $[\mu_c, \rho_c]$, of the output variables, $[\mu, \rho]$, are available and controlled in real-time, some high-order state variables may not be observable (see section 3.1.3) and/or may not be expressed only in terms of the controlled variables [see matrices Γ_μ in Eq. (51) and Γ_ρ in Eq. (58)]. The latter situation is more troublesome because the controller design is based on optimal *state control*, and assumes the observability of all states. It may then be advantageous to use appropriate reduced-order models with a number of state variables, $n_{x,c}$ and $n_{z,c}$, equal to the number of measured magnetic and kinetic outputs (say $n_{\mu,c}$ and $n_{\rho,c}$, respectively). The procedure described below allows such models to be constructed by treating the $(n_x - n_{x,c})$ highest order magnetic eigenmodes and the $(n_z - n_{z,c})$ highest order kinetic eigenmodes in the quasi-static approximation.

A new basis can be chosen for the state space, such that the first basis vectors of the slow system are combinations of the $n_{x,c} = n_{\mu,c} \leq n_x$ slowest magnetic eigenmodes only, and the first basis vectors of the fast system are combinations of the $n_{z,c} = n_{\rho,c} \leq n_z$ slowest kinetic eigenmodes only. The new state vectors of the full system, [x, z], or in reduced form, [X, Z], can then be decomposed as

$$X = x - x_\infty = \begin{bmatrix} X_c \\ X_u \end{bmatrix} = \begin{bmatrix} x_c - x_{c,\infty} \\ x_u - x_{u,\infty} \end{bmatrix} \qquad Z = z - z_\infty = \begin{bmatrix} Z_c \\ Z_u \end{bmatrix} = \begin{bmatrix} z_c - z_{c,\infty} \\ z_u - z_{u,\infty} \end{bmatrix} = \begin{bmatrix} Z_{s,c} \\ Z_{s,u} \end{bmatrix} + \begin{bmatrix} z_{f,c} \\ z_{f,u} \end{bmatrix} \qquad \text{(A3-1)}$$

Interestingly, with some straightforward algebra, the state space basis can also be chosen such that [x, z] are related to [μ, ρ] through transformation matrices, T_s and T_f, which are lower triangular:

$$\mu = \begin{bmatrix} \mu_c \\ \mu_u \end{bmatrix} = T_s \cdot \begin{bmatrix} x_c \\ x_u \end{bmatrix} = \begin{bmatrix} T_{s,cc} & 0 \\ T_{s,uc} & T_{s,uu} \end{bmatrix} \cdot \begin{bmatrix} x_c \\ x_u \end{bmatrix}; \qquad \rho = \begin{bmatrix} \rho_c \\ \rho_u \end{bmatrix} = T_f \cdot \begin{bmatrix} z_c \\ z_u \end{bmatrix} = \begin{bmatrix} T_{f,cc} & 0 \\ T_{f,uc} & T_{f,uu} \end{bmatrix} \cdot \begin{bmatrix} z_c \\ z_u \end{bmatrix} \tag{A3-2}$$

while, at the same time, the new A-matrices of the state space models, A_s* and A_f*, are upper triangular:

$$A_s^* = \begin{bmatrix} A_{s,cc} & A_{s,cu} \\ 0 & A_{s,uu} \end{bmatrix}; \quad A_f^* = \begin{bmatrix} A_{f,cc} & A_{f,cu} \\ 0 & A_{f,uu} \end{bmatrix}. \tag{A3-3}$$

In Eq. (A3-2), the components of the vector μ (respectively ρ) have been re-ordered so that the first $n_{\mu,c} = n_{x,c}$ (respectively $n_{\rho,c} = n_{z,c}$) components which compose μ_c (respectively ρ_c) are all available in real-time.

In the new basis, the B-matrices of the state space models, B_s* and B_f*, are then simply decomposed as

$$B_s^* = \begin{bmatrix} B_{s,c} \\ B_{s,u} \end{bmatrix}; \quad B_f^* = \begin{bmatrix} B_{f,c} \\ B_{f,u} \end{bmatrix}. \tag{A3-4}$$

Since $A_{s,cc}$ contains the slowest eigenvalues, we can possibly assume that the eigenvalues of $A_{s,uu}$ are $O(\varepsilon^{-1})$ larger than those of $A_{s,cc}$ (note that this may require a shift in the definition of the time scale ordering), so that the quasi-stationary approximation holds for the variables x_u and their dynamics can be neglected in the slow system. Defining

$$A_{s,c}^* = A_{s,cc}\ ,\ B_{s,c}^* = B_{s,c} - A_{s,cu} \cdot (A_{s,uu})^{-1} \cdot B_{s,u} \tag{A3-5a}$$

$$T_{s,c} = \begin{bmatrix} T_{s,cc} \\ T_{s,uc} \end{bmatrix}, \qquad D_{\mu,s}^* = \begin{bmatrix} 0 \\ -T_{s,uu} \cdot (A_{s,uu})^{-1} \cdot B_{s,u} \end{bmatrix} \tag{A3-5b}$$

$$C_{\rho,s}^* = C_s \cdot T_{s,c} \quad \text{and} \quad D_{\rho,s}^* = C_s \cdot D_{\mu,s}^* + D_s \tag{A3-5c}$$

the slow system then reads :

$$\dot{x}_c = A_{s,c}^* x_c + B_{s,c}^* u_s \tag{A3-6a}$$

$$\begin{bmatrix} \mu_s \\ \rho_s \end{bmatrix} = \begin{bmatrix} T_{s,c} \\ C_{\rho,s}^* \end{bmatrix} \cdot x_c + \begin{bmatrix} D_{\mu,s}^* \\ D_{\rho,s}^* \end{bmatrix} \cdot u_s = C_s^* \cdot x_c + D_s^* \cdot u_s \tag{A3-6b}$$

We have also implicitly assumed here that the components of x_u are stable. They can be assimilated to the fast variables,ρ and z, i.e.$x_u$and μ_u contain both slow and fast components [$x_u = x_{s,u} + x_{f,u}$, with $x_{s,u} = -(A_{s,uu})^{-1}. B_{s,u} . u_s$, and $\mu_u = \mu_{s,u} + \mu_{f,u}$]. Consistently with the two-time-scale approximation, we have defined μ_s in Eq.(A3-6b) as being made of μ_c and $\mu_{s,u}$. New dynamical equations,

$$\dot{x}_{f,u} = A_{s,uu}\, x_{f,u} + B_{s,u}\, u_f \tag{A3-7a}$$

$$\mu_{f,u} = T_{s,uu} \cdot x_{f,u} \ , \tag{A3-7b}$$

obtained by inserting Eq.(A3-2) to (A3-4) into the new state space models should, in principle, be included in the fast system. But this is not essential if they involve uncontrolled variables only, because they are not coupled with the equations that govern the dynamics of the other fast variables, z and ρ.

With the same procedure, if the fast eigenmodes, $z_{f,u}(t)$, are stable, and the eigenvalues of $A_{f,uu}$ can be assumed $O(\varepsilon^{-1})$ larger than those of $A_{f,cc}$, the fast system (with $\rho_f = \rho - \rho_s$) can be reduced to

$$\dot{z}_{f,c} = A^*_{f,c}\, z_{f,c} + B^*_{f,c}\, u_f \tag{A3-8a}$$

$$\rho_f = T_{f,c} \cdot z_{f,c} + D^*_f \cdot u_f \tag{A3-8b}$$

where

$$A^*_{f,c} = A_{f,cc} \ , \quad B^*_{f,c} = B_{f,c} - A_{f,cu} \cdot (A_{f,uu})^{-1} \cdot B_{f,u} \tag{A3-9a}$$

$$T_{f,c} = \begin{bmatrix} T_{f,cc} \\ T_{f,uc} \end{bmatrix}, \quad D^*_f = \begin{bmatrix} 0 \\ -T_{f,uu} \cdot (A_{f,uu})^{-1} \cdot B_{f,u} \end{bmatrix} \tag{A3-9b}$$

The slow system (Eq.A3-6), of order $n_{x,c}$, is now represented by a state vector, x_c, and the fast system (Eq.A3-8), of order $n_{z,c}$, by a state vector, z_c. These new models can be validated against experimental data and implemented in the controller design in place of the original high-order models. Their *controllability* can be checked by applying criteria (41a-b) to the matrices $A^*_{s,c}$, $A^*_{s,c}$, and $A^*_{f,c}$, $B^*_{f,c}$, respectively:

$$\text{Rank} \left[(\lambda^*_{s,i} \cdot \text{Id}_{n_{x,c}} - A^*_{s,c}) \quad B^*_{s,c} \right] = n_{x,c} \quad \text{for } i = 1, 2, ..., n_{x,c} \tag{A3-10a}$$

and

$$\text{Rank} \left[(\lambda^*_{f,j} \cdot \text{Id}_{n_{z,c}} - A^*_{f,c}) \quad B^*_{f,c} \right] = n_{z,c} \quad \text{for } j = 1, 2, ..., n_{z,c}. \tag{A3-10b}$$

where $\lambda^*_{s,i}$ and $\lambda^*_{f,j}$ are the eigenvalues of $A^*_{s,c}$ and $A^*_{f,c}$, respectively, i. e. the slowest eigenvalues of the original high-order slow and fast systems, respectively.

Now, restricting the output equations to :

$$\mu_c = T_{s,cc} \cdot x_c \quad \text{and} \quad \rho_{f,c} = T_{f,cc} \cdot z_{f,c}\,, \tag{A3-11}$$

the system *observability* requires that

$$\text{Rank} \begin{bmatrix} (\lambda^*_{s,i} \cdot Id_{n_{x,c}} - A^*_{s,c}) \\ T_{s,cc} \end{bmatrix} = n_{x,c} \quad \text{for } i = 1, 2, ..., n_{x,c} \tag{A3-12a}$$

and

$$\text{Rank} \begin{bmatrix} (\lambda^*_{f,j} \cdot Id_{n_{z,c}} - A^*_{f,c}) \\ T_{f,cc} \end{bmatrix} = n_{z,c} \quad \text{for } j = 1, 2, ..., n_{z,c}. \tag{A3-12b}$$

This is satisfied when μ_c and ρ_c are chosen such that $T_{s,cc}$ and $T_{f,cc}$ are *full* triangular matrices since, in such a case, their rank is already $n_{x,c}$ and $n_{z,c}$, respectively. This generally leaves a wide range of possibilities for choosing the $n_{x,c}$ components μ_c within the μ vector and the $n_{z,c}$ components ρ_c within the ρ vector so that the system is observable through the outputs μ_c and ρ_c only. If this is not the case, a larger set of outputs, $[\mu_\gamma, \rho_\gamma]$, must be used until the state variables can be expressed in terms of the outputs :

$$x_c = \Gamma_{\mu,\gamma} \cdot \mu_\gamma \quad \text{and} \quad z_c = \Gamma_{\rho,\gamma} \cdot \rho_\gamma\,, \tag{A3-13}$$

When all the outputs are controlled, the static gain matrix of the system is not modified by the quasi-static approximations which lead to Eq.(A3-6) and (A3-8). Therefore, for a given target state, $[\mu_{target}, \rho_{target}]$, the closest coherent achievable state $[\mu_\infty, \rho_\infty]$ is the same with the new models as with the original high-order models.

Table 1

x	0.1	0.2	0.3	0.4	0.5	0.6	0.7	0.8	0.9	1
$\Phi'(x)$	2.4	4.7	7.2	9.7	12.4	15.3	18.5	22.1	26.1	30.6

Table 2

x	0.1	0.2	0.3	0.4	0.5	0.6	0.7	0.8	0.9	1
$q(x)$	2.02	2.13	2.27	2.47	2.73	3.05	3.45	3.96	4.60	5.42

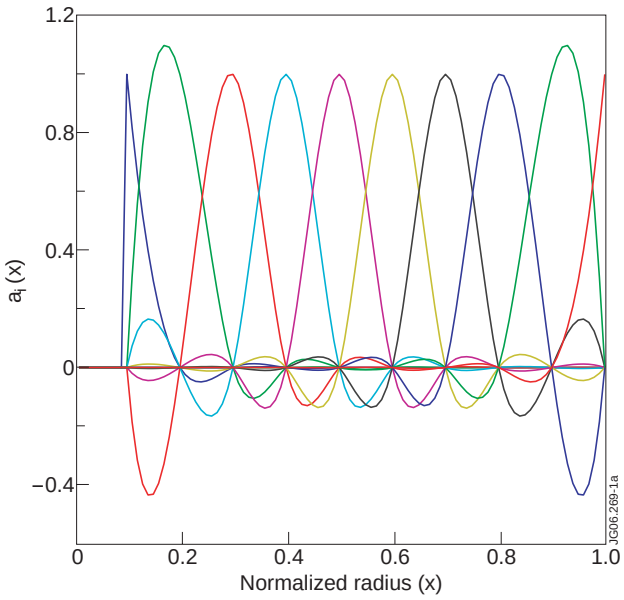

Figure 1(a): Cubic splines, $a_i(x)$, used for the expansion of $\Psi(x)$, i(x) and T(x).

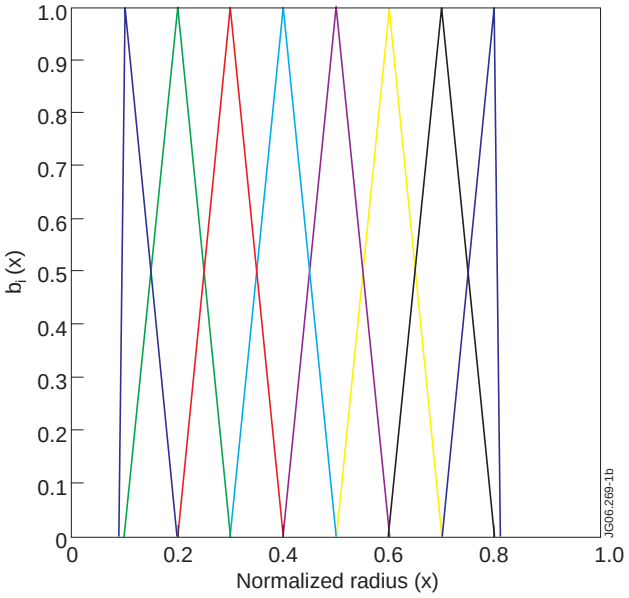

Figure 1(b): Piecewise linear functions, $b_i(x)$, used for the expansion of ρ_{Te}(x).*

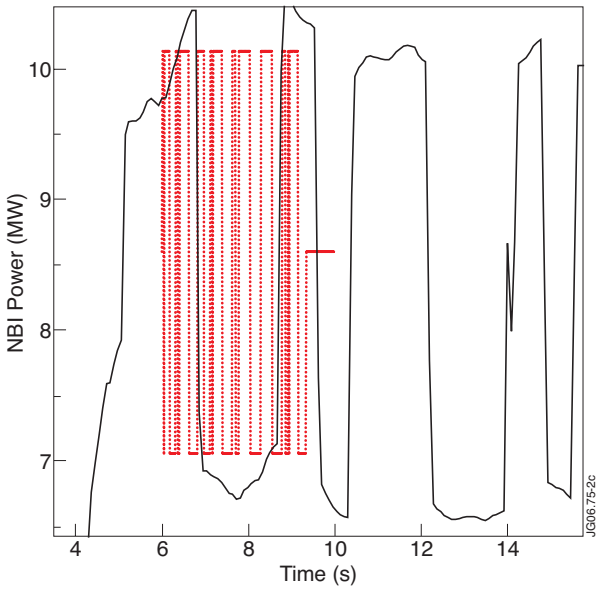

Figure 2: Examples of a fast (red dotted trace) and of a slow (black trace) modulation of the NBI power used for the identification of a two-time-scale state space model.

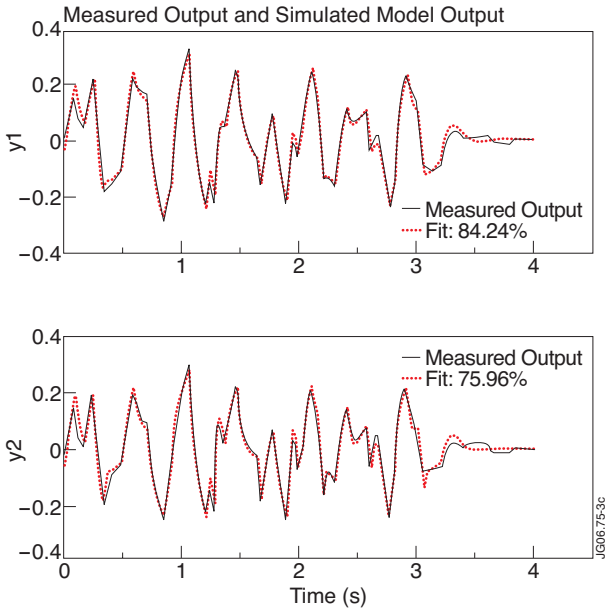

Figure 3: Comparison between the data from JETTO and from the identified state space (fast) model for two elements of the electron temperature vector (x = 0.3 and x = 0.4).

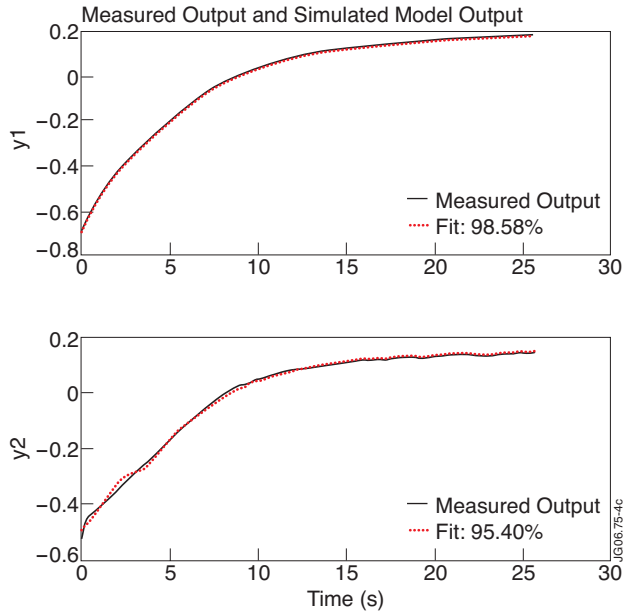

Figure 4: Comparison between the free dynamics data from JETTO and from the identified (slow) state space model for two elements of the poloidal flux vector at normalized radii x = 0.3 and x = 0.4.

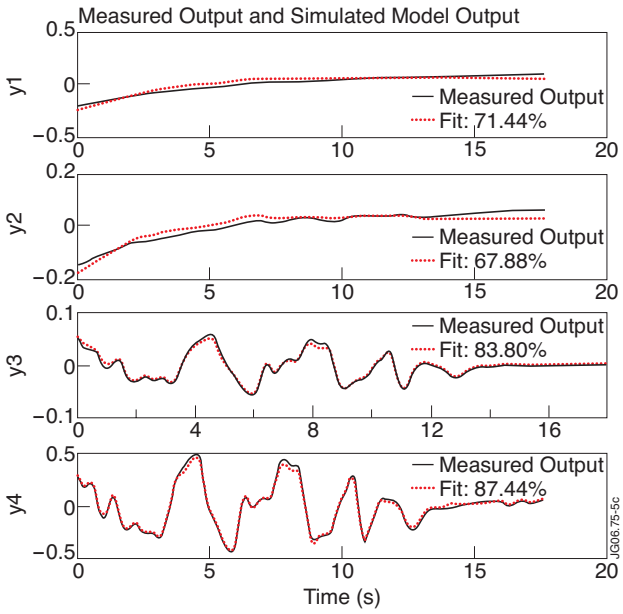

Figure 5: Comparison between the data from JETTO and from the identified (slow) state space model for two elements of the poloidal flux vector (y1, y2) and two elements of the electron temperature vector (y3, y4) at normalized radii x = 0.3 and x = 0.4).

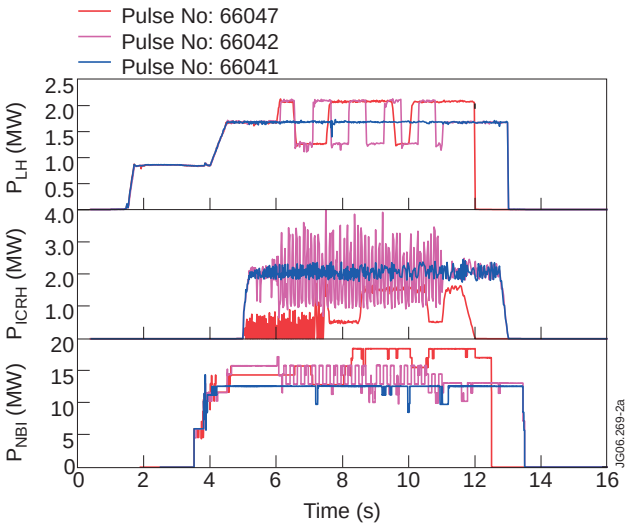

Figure 6: Input LH, ICRH and NBI powers for the reference Pulse No's: 66041 (blue), and modulated pulses 66047 (red) and 66042 (magenta).

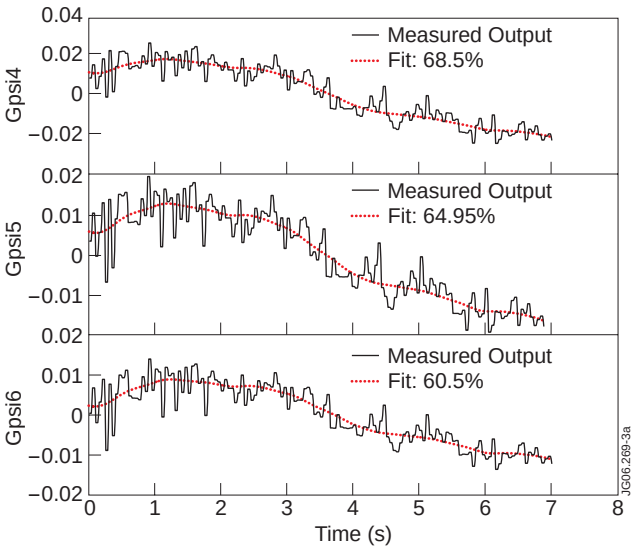

Figure 7: Identification of A_s from the reference pulse data. Comparison between the fit and the experimental data for three elements of the poloidal flux vector (x = 0.4, 0.5 and 0.6).

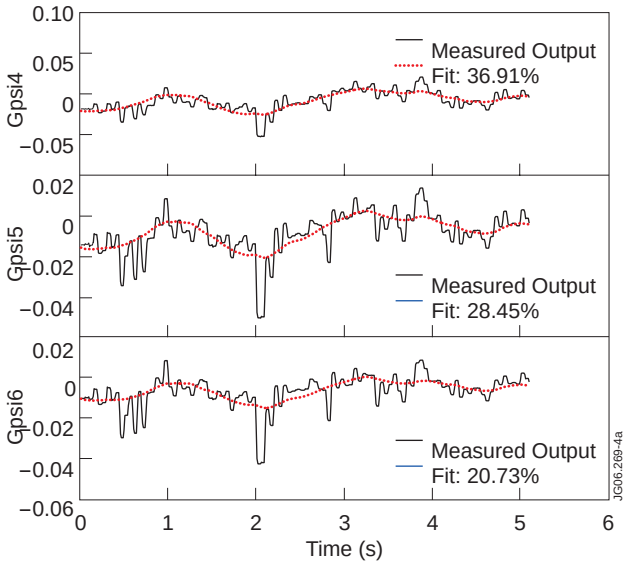

Figure 8: Identification of B_s from Pulse No: 66047. Comparison between the fit and the experimental data for three elements of the poloidal flux vector (x = 0.4, 0.5 and 0.6).

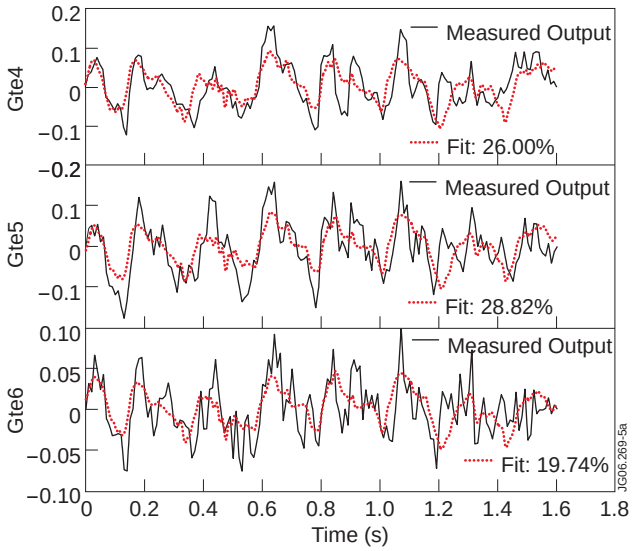

Figure 9: Identification of A_f and B_f from Pulse No: 66042. Comparison between the fit and the experimental data for three elements of the electron temperature vector (x = 0.4, 0.5 and 0.6).

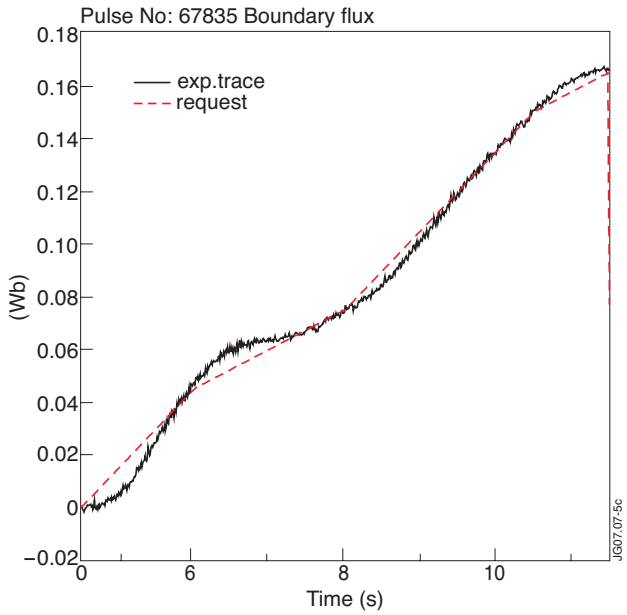

Figure 10(a): Control of the plasma boundary flux, Pulse No: 67835, using the PF system (XSC) as an actuator.

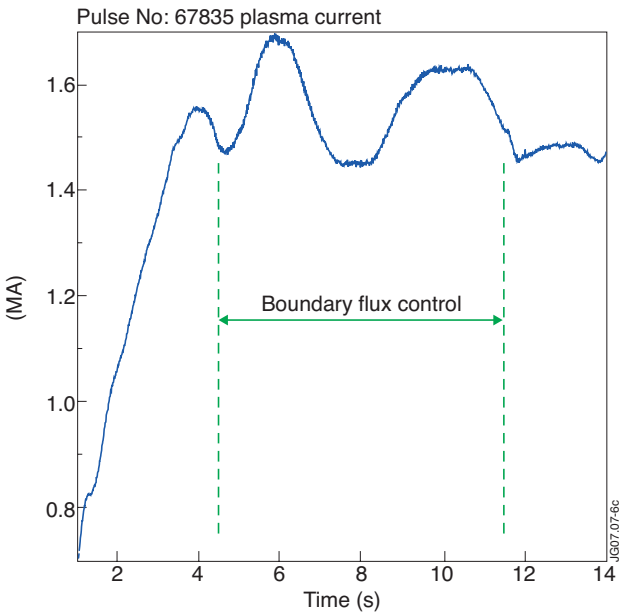

Figure 10(b):Time evolution of the plasma current during the control of the boundary flux, Pulse No: 67835

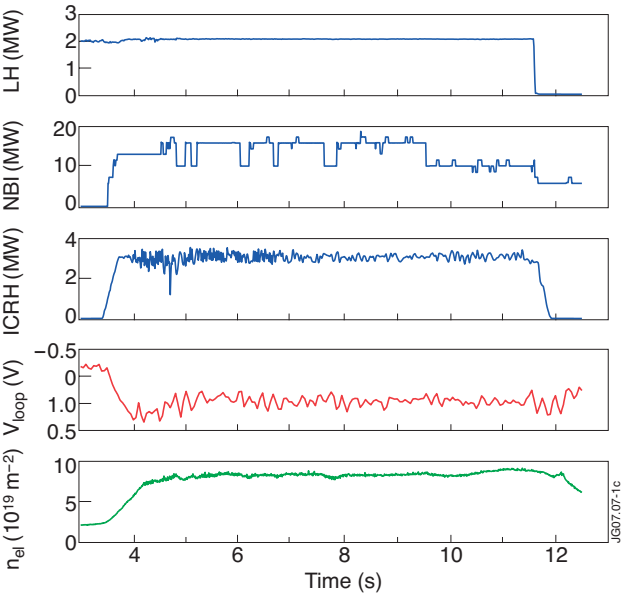

Figure 11: Input H&CD powers (blue), surface loop voltage (red) and line-integrated density (green) for Pulse No: 67874.

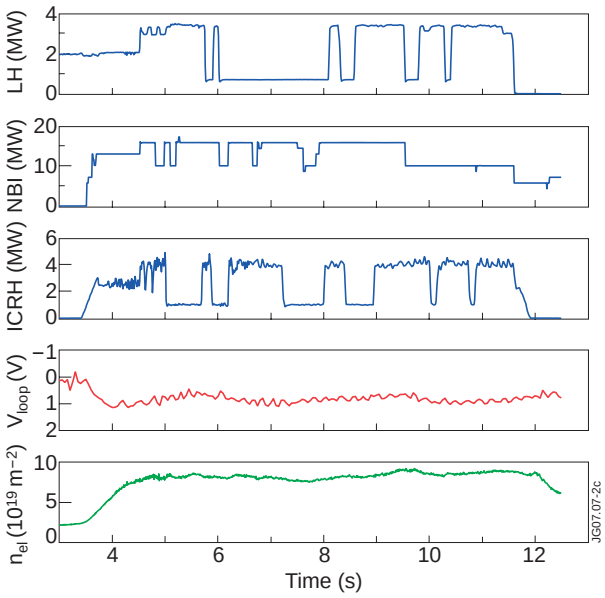

Figure 12: Input H&CD powers (blue), surface loop voltage (red) and line integrated density (green) for Pulse No: 67876..

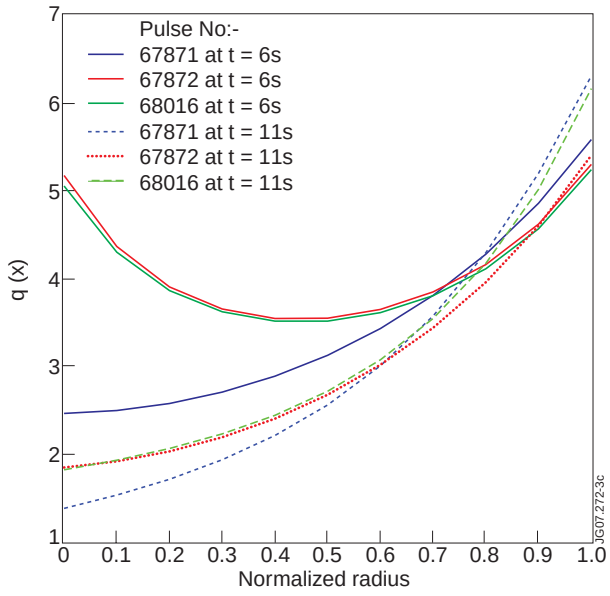

Figure 13(a): Typical variations of the safety factor. The figure shows q(x) at t = 6s. (full lines) and t = 11s. (dashed lines), for Pulse No's: 7871 (blue), 67872 (red) and 68016 (green).

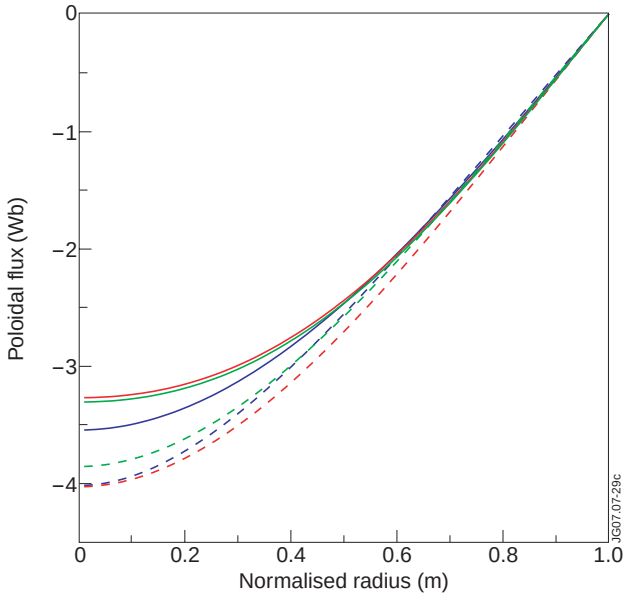

Figure 13(b): Typical variations of the internal poloidal flux. The figure shows Ψ(x) at t = 6s. (full lines) and t = 11s. (dashed lines), for Pulse No's: 67871 (blue), 67872 (red) and 68016 (green).

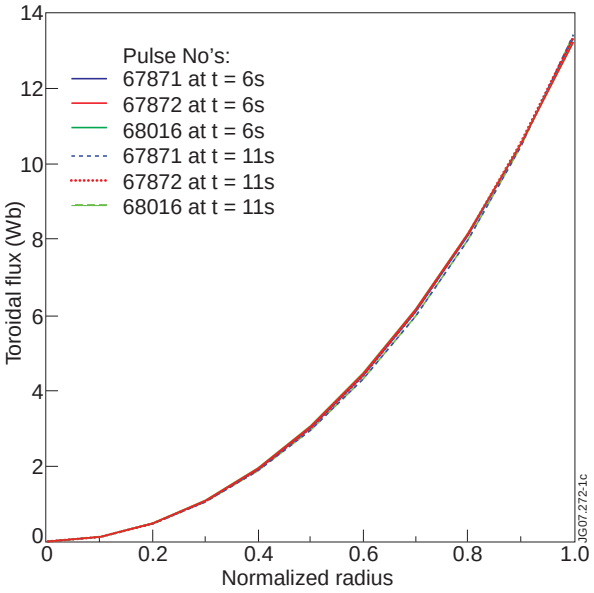

Figure 13(c): Typical variations of the internal toroidal flux. The figure shows Φ(x) at t = 6s. (full lines) and t = 11s. (dashed lines), for Pulse No's: 67871 (blue), 67872 (red) and 68016 (green).

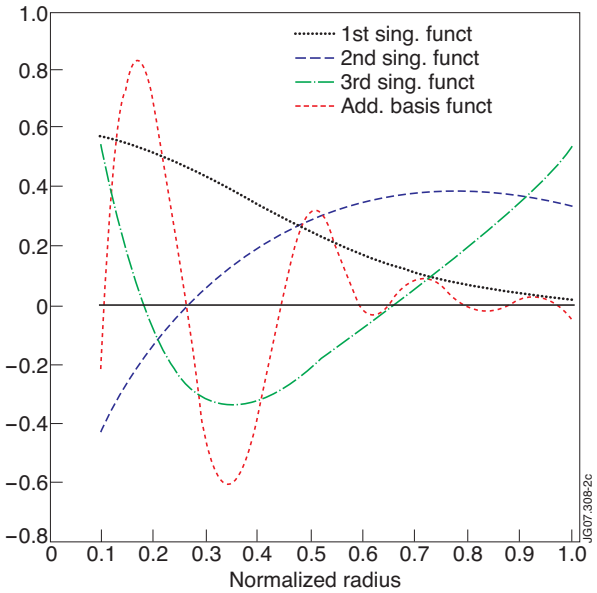

Figure 14: The first three output singular functions of the static gain matrix for i(x) (black, blue and green curves), and an additional basis function of the orthogonal subspace (red curve).

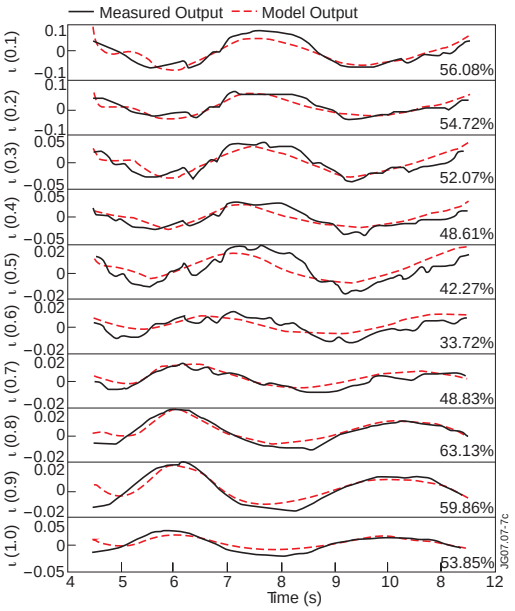

Figure 15: Comparison between the measured i(x) profile and the model-based simulation at 10 fixed normalized radii (x = 0.1, 0.2, 0.3, ..., 1). Pulse No: 67840: modulations of V_{ext} with constant H&CD powers. The fit parameter (Eq.11) is shown in each frame.

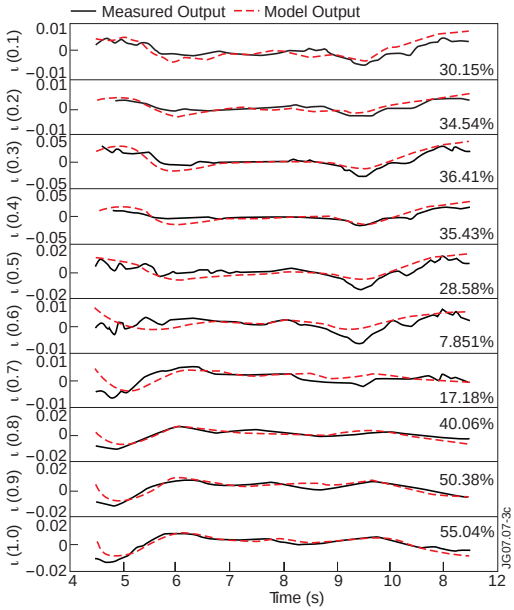

Figure 16:Comparison between the measured i(x) profile and the model-based simulation at 10 fixed normalized radii (x = 0.1, 0.2, 0.3, ..., 1). Pulse No: 67874 : modulations of NBI power with constant LH and ICRH powers, and constant request on V_{ext} (see Fig.11). The fit parameter (Eq.11) is shown in each frame.

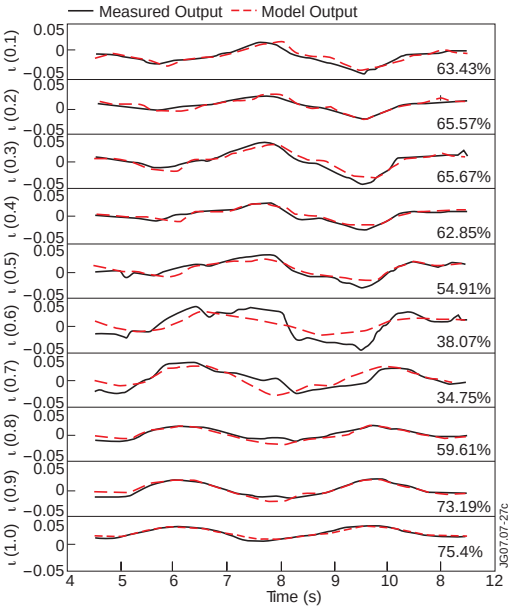

Figure 17:Comparison between the measured i(x) profile and the model-based simulation at 10 fixed normalized radii (x = 0.1, 0.2, 0.3, ..., 1). Pulse No:67876 : modulations of LH, NBI and ICRH powers with a constant request on V_{ext} (see Fig.12). The fit parameter (Eq. 11) is shown in each frame.

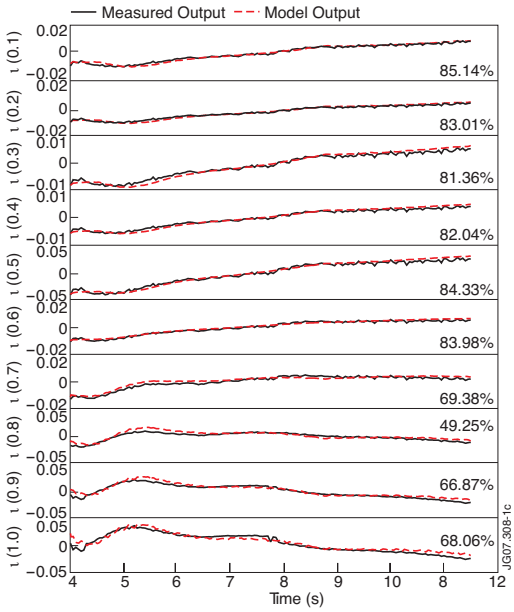

Figure 18:Comparison between the measured i(x) profile and the model-based simulation at 10 fixed normalized radii (x = 0.1, 0.2, 0.3, ..., 1) for a validation pulse (Pulse No: 70318 not used in the model identification process). The fit parameter (Eq. 11) is shown in each frame.

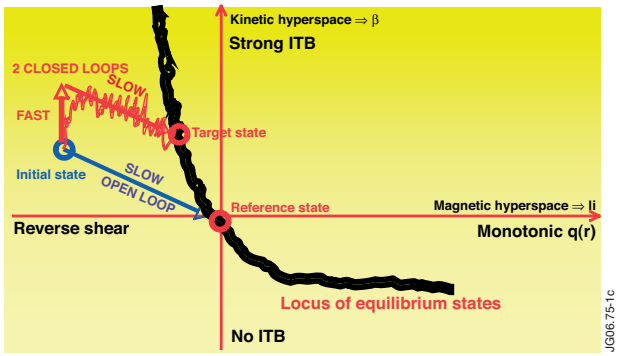

Figure 19: State space diagram showing schematically : (i) the slow relaxation of the system with constant input parameters (blue arrow), (ii) the asymptotic response when $\varepsilon \rightarrow 0$ to a change in these parameters leading to another equilibrium state (red arrows), and (iii) the closed-loop response of the system to the control laws when requesting the same target state (red trajectory). The locus of all possible equilibrium states is represented by the black curve. Lines and curves are artistic 1-D representations of multidimensional spaces.

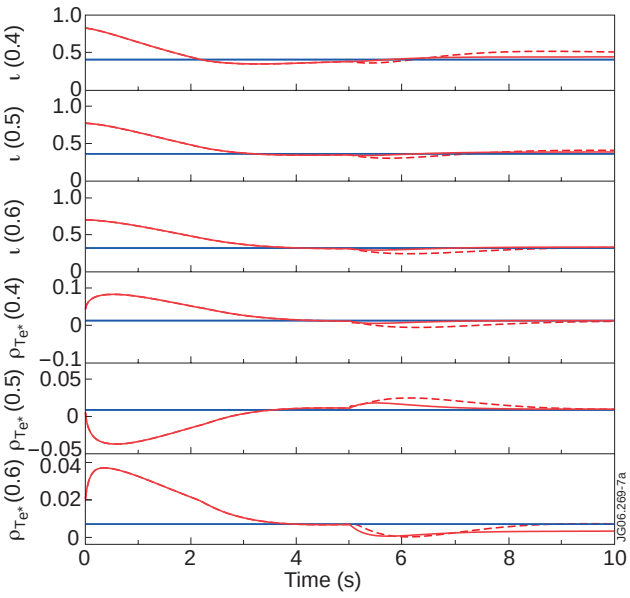

Figure 20: Evolution of $\iota(x)$(3 upper traces) and $\rho_{Te*}(x)$ (3 lower traces) at x=0.4, 0.5 and 0.6 in a closed-loop simulation with (full traces) and without (dotted traces) disturbance rejection. The requested target values are represented by the horizontal lines

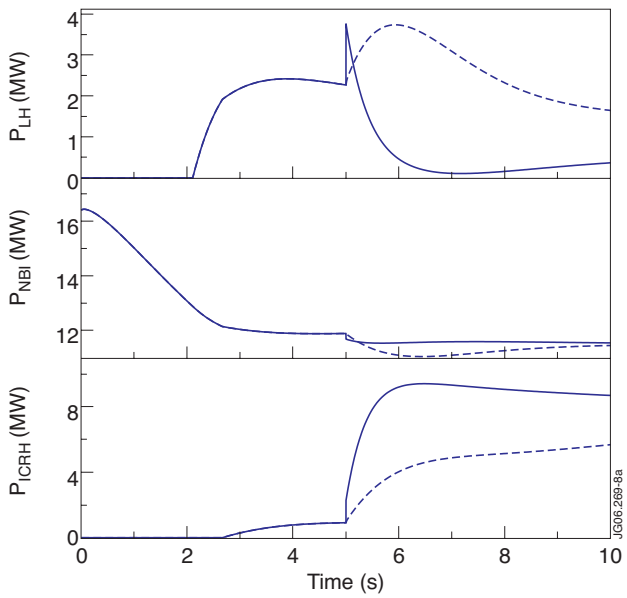

Figure 21: Evolution of the actuator powers in the closed-loop simulation with (full traces) and without (dotted traces) disturbance rejection. The time origin refers to the start of the control phase. A density perturbation is applied at t = 5s.

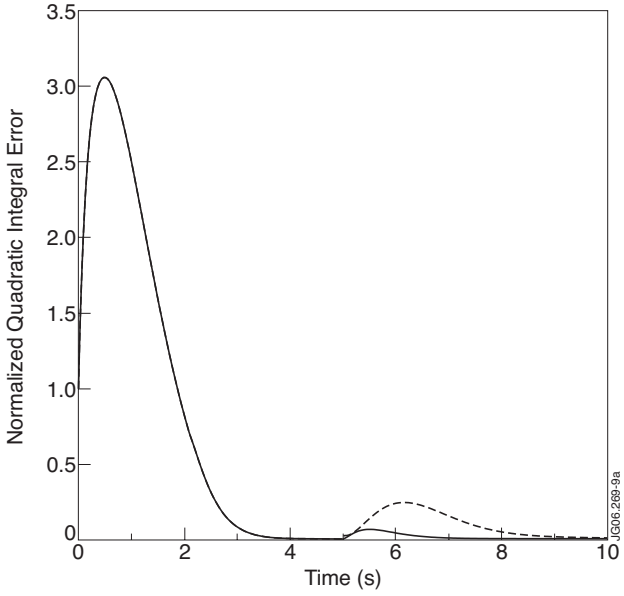

Figure 22: Evolution of the cost functional I_∞ in the closed-loop simulation with (full trace) and without (dotted trace) disturbance rejection. The time origin refers to the start of the control phase. A density perturbation is applied at t = 5s.

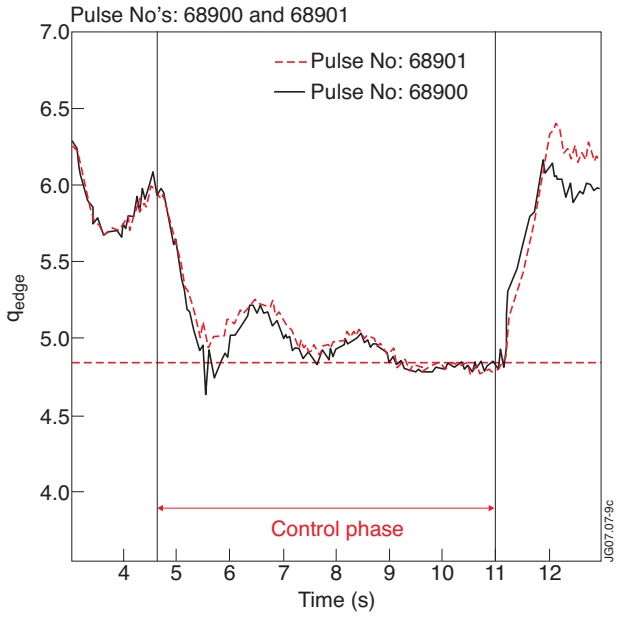

Figure 23: Regulation of the total plasma current using the PC during the main heating phase of two different discharges. The target value of q_{edge} is represented by the horizontal line.

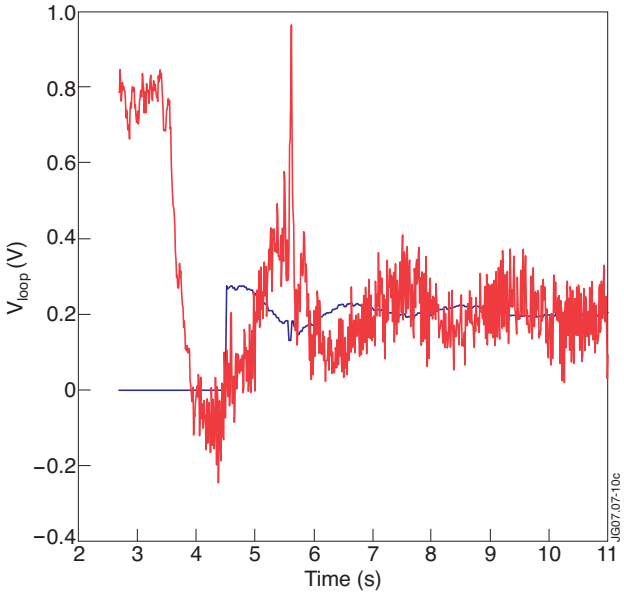

Figure 24: Comparison between the requested (blue trace) and the delivered loop voltage (red trace) during the control of q_{edge} in Pulse No: 68900.

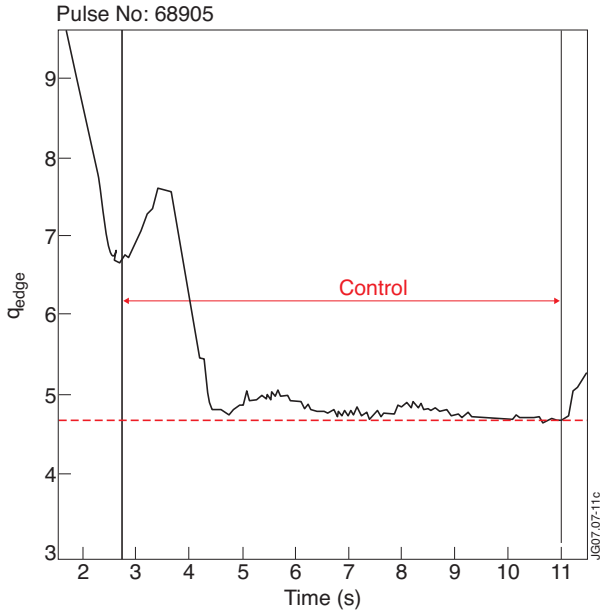

Figure 25(a): Control of the edge safety factor for plasma current ramp up (pulse #68905). The target value of q_{edge} is represented by the dotted horizontal line.

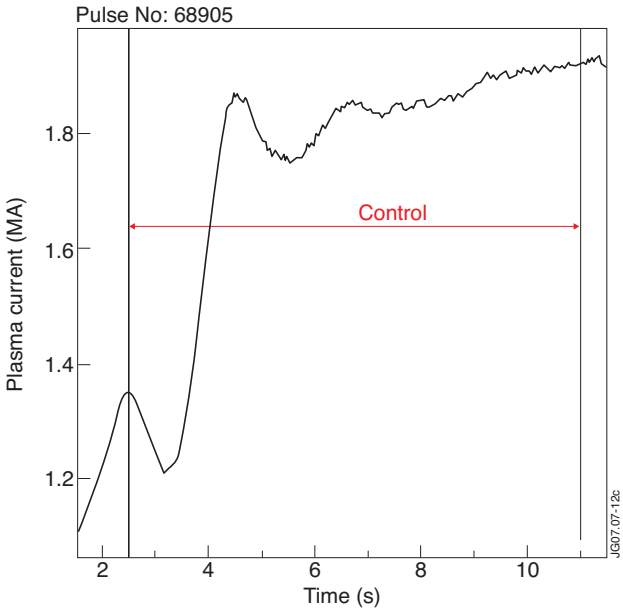

Figure 25(b): Plasma current ramp-up through the control of the edge safety factor with the PC (pulse #68905).

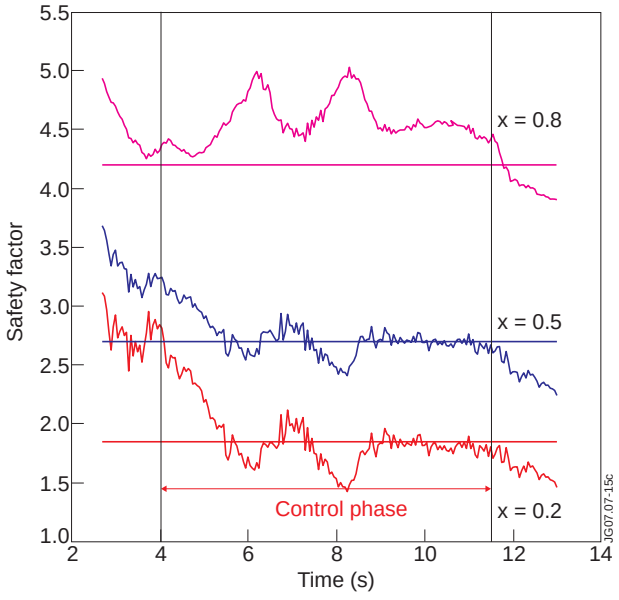

Figure 26(a): Control of the safety factor profile at three normalized radii, x = 0.2 (red), x =0.5 (blue), and x = 0.8 (magenta) using the three H&CD actuators (Pulse No: 70395). During the control phase V_{ext} is requested constant (32mV/rad). Target values are represented by horizontal lines.

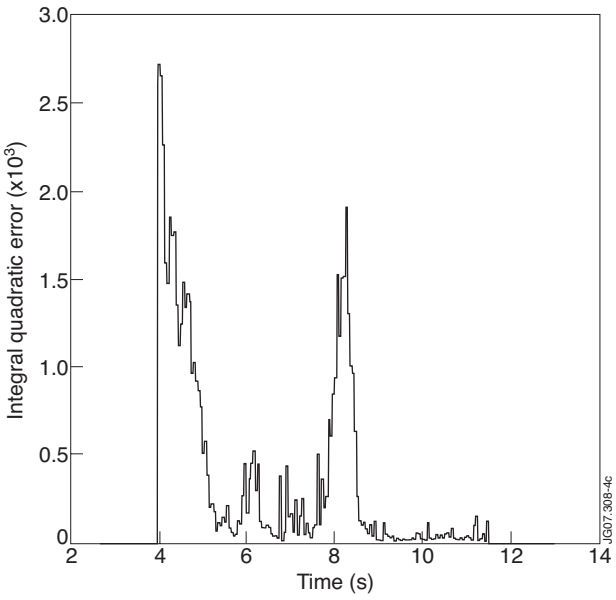

Figure 26(b): Time evolution of the cost functional I_∞ for Pulse No: 70395. After transient oscillations of the loop voltage, a quasi-steady minimum which corresponds to the closest coherent achievable state is reached.

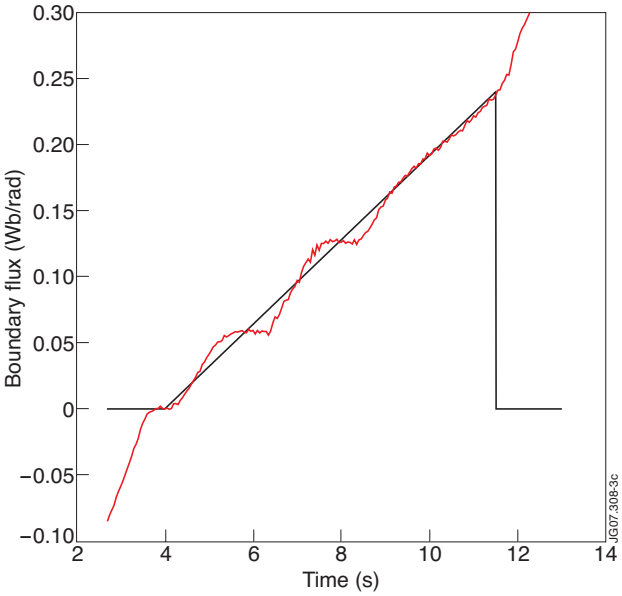

Figure 27(a): Requested (black trace) and delivered (red trace) boundary flux for Pulse No: 70395 with a desired constant loop voltage of 32 mV/rad.

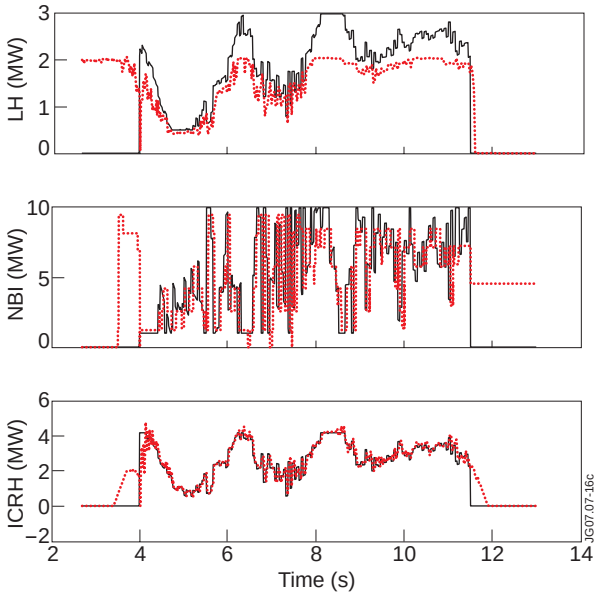

Figure 27(b): Requested (black traces) and delivered (red dotted traces) LH, NBI and ICRH powers for Pulse No: 70395.

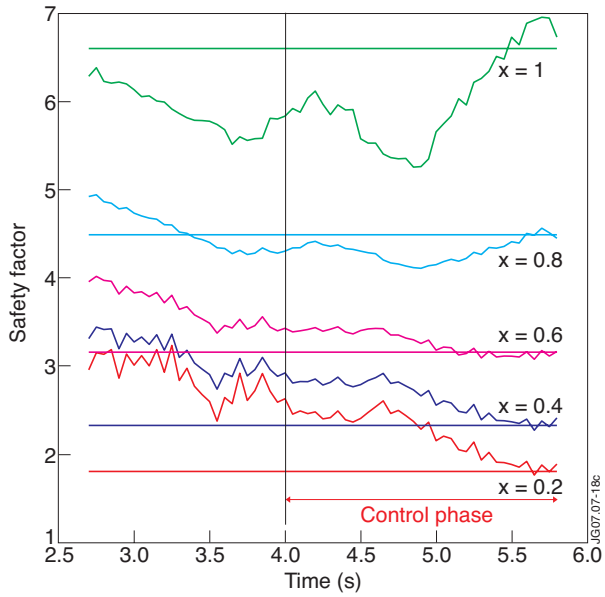

Figure 28(a): Control of the safety factor profile at five normalized radii, x = 0.2 (red), x = 0.4 (blue), x = 0.6 (magenta), x = 0.8 (cyan), and x = 1 (green), using the H&CD and loop voltage actuators (Pulse No:70404). Target values are represented by horizontal lines.

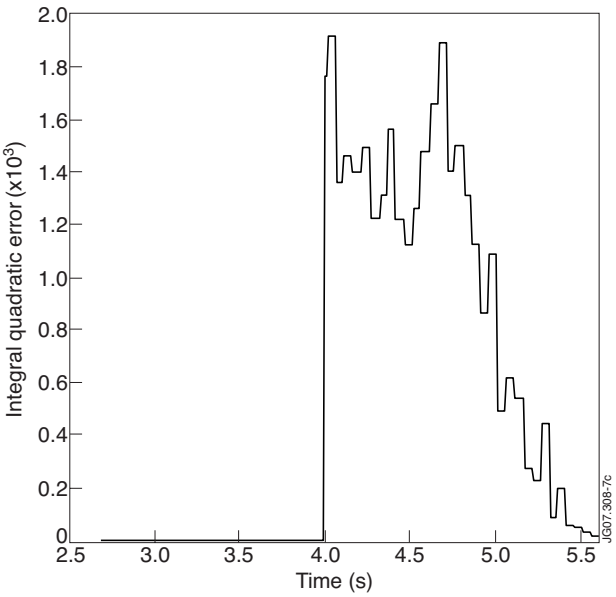

Figure 28(b): Time evolution of the cost functional I_∞ during the active phase of the profile controller in Pulse No:70404.

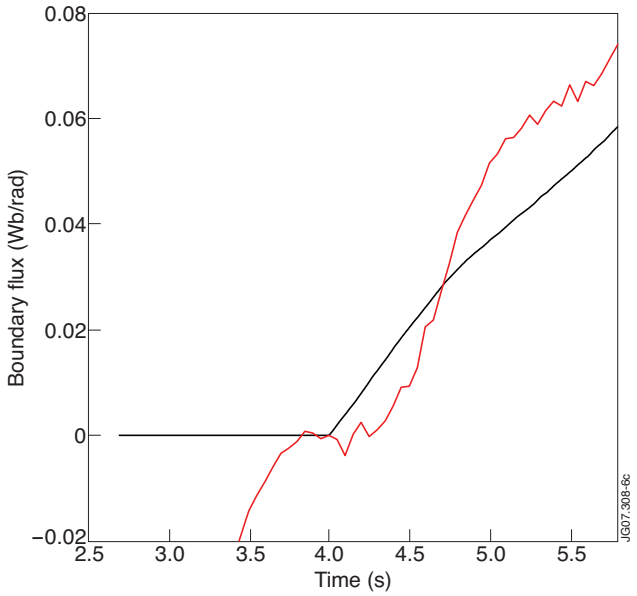

Figure 29(a): Requested (black trace) and delivered (red dashed trace) boundary flux for Pulse No:70404.

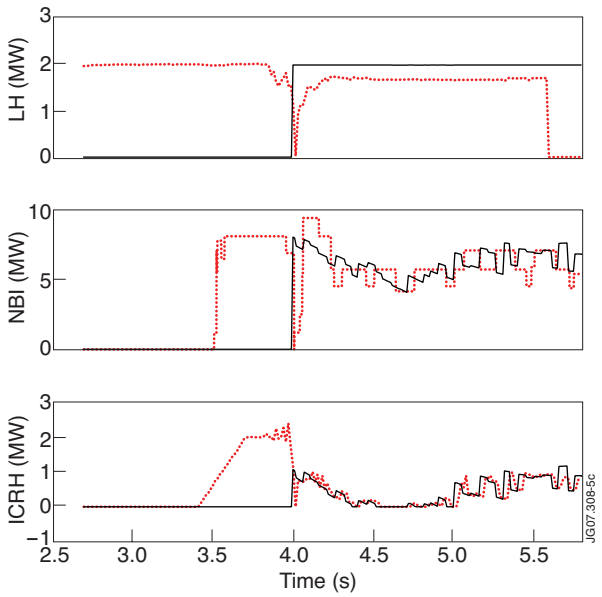

Figure 29(b): Requested (black traces) and delivered (red dotted traces) LH, NBI and ICRH powers for Pulse No:70404.